Somatic calcium imaging reveals simple spike activity of cerebellar Purkinje cells : applications and limitations to in vivo research

Jorge Enrique Ramírez Buriticá

THÈSE DE DOCTORAT DE L'UNIVERSITÉ SORBONNE PARIS CITÉ

Préparée à l'Université Paris Descartes

École doctorale: Bio Sorbonne Paris Cité (ED BioSPC- 562)

Département Développement, Génétique, Reproduction, Neurobiologie et Vieillissement (DGRNV)

Brain Physiology Lab - UMR 8118 – CNRS

GABAergic Synapses in the Cerebellum

L'imagerie calcique révèle l'activité de potentiels d'action simples des cellules de Purkinje cérébelleuses: Applications et limites de la méthode pour la recherche sur l'activité nerveuse in vivo

Par Jorge Enrique Ramírez Buriticá

Dirigée par Brandon Stell

Paris, 1er Août 2018

THÈSE DE DOCTORAT DE L'UNIVERSITÉ SORBONNE PARIS CITÉ

Préparée à l'Université Paris Descartes

École doctorale: Bio Sorbonne Paris Cité (ED BioSPC- 562)

Département Développement, Génétique, Reproduction, Neurobiologie et Vieillissement (DGRNV)

Brain Physiology Lab- UMR 8118 – CNRS

GABAergic Synapses in the Cerebellum

Somatic Calcium imaging reveals simple spike activity of cerebellar Purkinje Cells: applications and limitations to in vivo research

By Jorge Enrique Ramírez Buriticá

Directed by Brandon Stell

Paris, August 1st 2018

Titre: L'imagerie calcique révèle l'activité de potentiels d'action simples des cellules de Purkinje cérébelleuses: Applications et limites de la méthode pour la recherche sur l'activité nerveuse *in vivo*

Résumé. Le cervelet est impliqué dans la coordination des mouvements, et il traite l'information sensorimotrice au niveau du cortex cérébelleux avant d'envoyer le résultat de ce traitement aux autres régions du cerveau. Comme toute l'information traitée par le cervelet converge sur les cellules de Purkinje (CP), la perspective d'enregistrer l'activité nerveuse de populations bien identifiées de ces cellules est un enjeu crucial pour la compréhension du traitement d'information par le cervelet. Dans cette thèse, nous montrons que des enregistrements par imagerie calcique somatique des cellules de Purkinje peuvent fournir une image fidèle de l'activité de potentiels d'action simples sodium dépendants (SS), sans souffrir de contamination significative provenant de fluctuations calciques dendritiques liées à des potentiels d'action complexes (CS). En utilisant cette approche nous avons développé des méthodes permettant l'enregistrement de changements de rythmes de décharge de potentiels SS dans des cellules de Purkinje dans des tranches de cerveau et *in vivo*. Dans des tranches de cervelet, nous avons effectué des enregistrements simultanés de groupes de cellules de Purkinje, et nous avons ainsi montré une organisation spatiale remarquable de pauses de l'activité nerveuse des cellules de Purkinje à l'intérieur d'un plan sagittal. Nous avons de plus montré que cette organisation résulte de l'activité du réseau de cellules inhibitrices présynaptiques, puisque le blocage de récepteurs ionotropiques au GABA abolit la synchronicité entre cellules voisines. En ce qui concerne les expériences *in vivo*, nous avons testé la faisabilité de notre méthode d'imagerie pour inférer l'activité des cellules de Purkinje en utilisant l'indicateur calcique génétique GCaMP6f. Bien que la fluorescence de cet indicateur soit une fonction complexe de la concentration en calcium, nous avons pu développer une méthode qui permet une estimation quantitative des changements du rythme de décharge de potentiels SS dans les cellules de Purkinje. Cette méthode est susceptible d'ouvrir des perspectives nouvelles pour l'étude de l'activité nerveuse du cortex cérébelleux *in vivo*.

Mots-clés: Cervelet, Imagerie calcique, Cellule de Purkinje, Potentiel d’action simple.

Title: Somatic Calcium imaging reveals simple spike activity of cerebellar Purkinje Cells: applications and limitations to *in vivo* research.

Abstract. The cerebellum is thought to coordinate movement by processing sensorimotor information in the cerebellar cortex before relaying its output to other brain structures. Since all information processed by the cerebellar cortex converges on Purkinje cells (PCs), the ability to record the spiking output from identified populations of these cells is crucial for understanding cerebellar processing. In this thesis, we demonstrate that somatic calcium imaging in Purkine cells is a faithful reporter of sodium-dependent simple spike (SS) activity, with almost no interference coming from the dendritic calcium fluctuations of complex spikes (CS). This enabled us to optically record changes in SS firing rates from Purkinje cells in brain slices and *in vivo*. In cerebellar slices, the simultaneous recordings of Purkinje cell groups revealed a striking spatial organization of pauses in Purkinje cell activity inside a sagittal plane. The source of this organization is shown to be the presynaptic gamma-Aminobutyric acid producing (GABAergic) network, since blocking ionotropic GABA receptors (GABAARs) abolishes the synchrony. Concerning *in vivo* experiments, we tested the feasibility of this imaging method to infer Purkinje cell activity in combination with the genetically encoded calcium indicator GCaMP6f. Despite the nonlinear binding kinetics of GCaMP6f with calcium, we developed a method that allows a quantitative estimate of changes in Purkinje cell SS firing activity. This method is susceptible to open new avenues for research on cerebellar cortex output *in vivo*.

Keywords: Cerebellum, Calcium Imaging, Purkinje Cell, Simple Spike

To my wonderful family,
for always breaking the mold
and enhancing my life with love.

Acknowledgment

These last 4 years of PhD adventure have been like a juxtaposition between the new and old, brute and enriched, day and night experiences, that passed so quickly my sight could only distinguish it as a colorful amalgam of emotions.

From the core of this experiences, I want to thank my lab, the UMR8118 at the University Paris Descartes, for hosting me all these years and enable my pursuit of scientific literacy. I also thank the CNRS, specially the lovely crew of Human Resources, for their support in the legal domains.

In a juxtaposition of old with new gratitude, I am very thankful to Ann, Diego, Lyle and Megan for accepting the call for jury, and reading through the passages of my work.

I am very grateful to Brandon for his guidance to transform our brute experimentations into a precious work valued by ourselves and our peers. Also, I would like to thank Isabel and Alain for their cheerful wisdom and their raw help with both their body of work and their wi-fi password. Just kidding, with their incommensurable help to get me established in Paris!

Special thanks to Michael for the enrichments he succinctly offered to my work, both in the analytical and in the logistical parts. Also, for indulging my first curiosity with electronics. In that regard, I would also like to thank David Ogden for the opportunity to enrich my life experience with an invitation to an electronics course overseas.

For the days in the lab, I want to thank many members of our side of the hallway that made my time funnier and worthier: Camila, Javier, Taka, Gerardo, Kris, Fede, Merouann, Van; with the visits of Siva, Marcin, Lulu, Elke, Laura and Domi. The nights that followed our days were even worthier! Specially the ping-pong-movie assemblies, and the Belgium beer escapades!

And for some of the nights that passed up to the next ray of light, I thank Juan, Oscar, Javier, Monika, Ewa, Livia, Eduardo and the homeless crew from the CEA!

And coating all these emotions with a shine that reflects back in my heart, I want to thank my family for being always around despite our distance (sometimes very close, my dear sista). And to my beloved Maica, for the sharing to come, a thank you that comes up in front!

TABLE OF CONTENTS

Figure Index

Table Index

1. INTRODUCTION

To cope with a changing environment, animals must form accurate representations of their context using their sensory inputs, so they can change their behavior accordingly. However, the self-generated stimuli produced by an animal's engagement with its environment (known as reafference) gets mixed with the external stimuli, thus confounding the relevant information needed to adjust its behavior. One option to minimize this confusion might be attained by comparing the animal's sensory input with other sources of information of the animal's own activity. Such extra information could come from copies of motor commands (known as corollary discharges). In principle, this additional information could be used to predict and nullify the effect of the self-generated stimuli so the external signals stand out. However, it is still unclear whether and how the brain of highly evolved vertebrates is able to make such computations (Sawtell, 2017).

1.1. Primitive behavior correction based on sensory prediction: Cerebellum-like structures

Some independent evolutionary threads in the animal kingdom have maintained simpler versions of sensory systems that have to deal directly with this reafferent cancelling of self-generated sensory stimuli. One well studied example is the electrosensory system in aquatic animals like in some elasmobranchii (sharks and rays, e.g. Bodznick, Montgomery, & Carey, 1999), gymnotids (knifefishes; MacIver, Sharabash, & Nelson, 2001), mormyrids (eg. elephant fish; Baker, Kohashi, Lyons-Warren, Ma, & Carlson, 2013) and even in mammals such as monotremes (Langner & Scheich, 2009). These animals are capable of locating the bioelectrical fields generated from living creatures in water through two types of electrolocation systems: (1) a passive sensing system constituted from ampullary electroreceptors and (2) an active system employing the perturbations created from a specialized electric organ sensed by tuberous electroreceptors. Both types of electrolocation are affected by the animal's own bioelectric fields (e.g. cardiac and ventilatory pulses), the movements of its receptors relative to itself (e.g. lateral line deformation while swimming), and their own electric organ discharges (EODs) for animals with active electrolocation (Sawtell, 2017).

Interestingly, there is a common feature among these electrosensory animals regarding the processing of their electroreceptor signals. Convergence of the electrosensory input with the

streams of additional information from the animal's behavior occurs in a brain structure similar to the mammalian cerebellum (Bell, Han, & Sawtell, 2008). In general, these cerebellum-like structures have one layer containing bundles of fibers running parallel to each other that carry the information predicting the sensation (like corollary discharges or proprioception). These parallel fibers establish excitatory synapses with the arborization of principal cells, which also receive peripheral electroreceptive input. The region where parallel fiber and principal cellss intersect is called the molecular layer, which usually contains inhibitory interneurons also connected to the parallel fibers (Golgi and stellate cells). The origin of the parallel fibers can be traced down to small cells located in a region called the granule layer.

Inside the principal cells, the combination of all the parallel fiber activities in their dendrites generates a signal that exactly opposes the sensory input coming from the electroreceptors when there is no external stimuli, creating what is called a negative image (Fig. 1.1.A). Thus, as elegantly demonstrated by Curtis Bell in the 1980s, when both the negative image and the sensory input collide in the principal cell, the output of the cell will only reflect the perturbations of the signal attributed to external sources (Bell, 1981). Moreover, the negative image could be readjusted via the plasticity of the parallel fiber responses in the principal cell to match new trends in the sensory inputs. This has been demonstrated by pairing artificial electrosensory stimuli to the central predictive signals in electroreceptive animals. For instance, in the mormyrid fish a pairing between its EOD motor command and an external electrical stimulus in its environment causes its ampullary receptors (the principal cells) to adapt their output so they stop responding to the new artificial trend. Once the pairing is halted, the ampullary receptors exhibit a response of opposite sign to the previous artificial stimulus, which in turn also fades eventually (Fig. 1.1.B).

In this way, the cerebellar-like structures could be though as adaptive filters that enrich the behaviorally relevant cues from the environment against the irrelevant background of sensorial trends, including reafference signals. The key feature of this filter is the production of a precisely-timed negative image, which requires a complex array of both excitatory and inhibitory signals that shape the response of the principal cells (Sawtell, 2017). To achieve this purpose, there exists subsets of interneurons inside the cerebellar-like structures that can modify the parallel fiber information: unipolar brush cells, Golgi cells, and stellate cells (Montgomery & Bodznick, 2016). The role of unipolar brush cells is to interconnect groups of granule cells via excitatory synapses, hence unifying the parallel fiber response on downstream targets. On the other hand, Golgi and

stellate cells are inhibitory cells embedded in the granule and molecular layer respectively. The function of their inhibition is to convert the excitatory signals coming from the parallel fibers into an opposite inhibitory version that allows for a change of the signal polarity. This enables the feedforward (or common-mode) rejection of some predictive information sources by cancelling their signals with their self-activated inhibitory counterpart. Additionally, if the inhibition activated by the feedforward mechanism surpasses the excitatory effect on the principal cells, the result could be a signal with a completely reversed polarity. This increases the effective dynamic range available for the negative image to cancel out the sensory input in the principal cells (Montgomery & Bodznick, 2016).

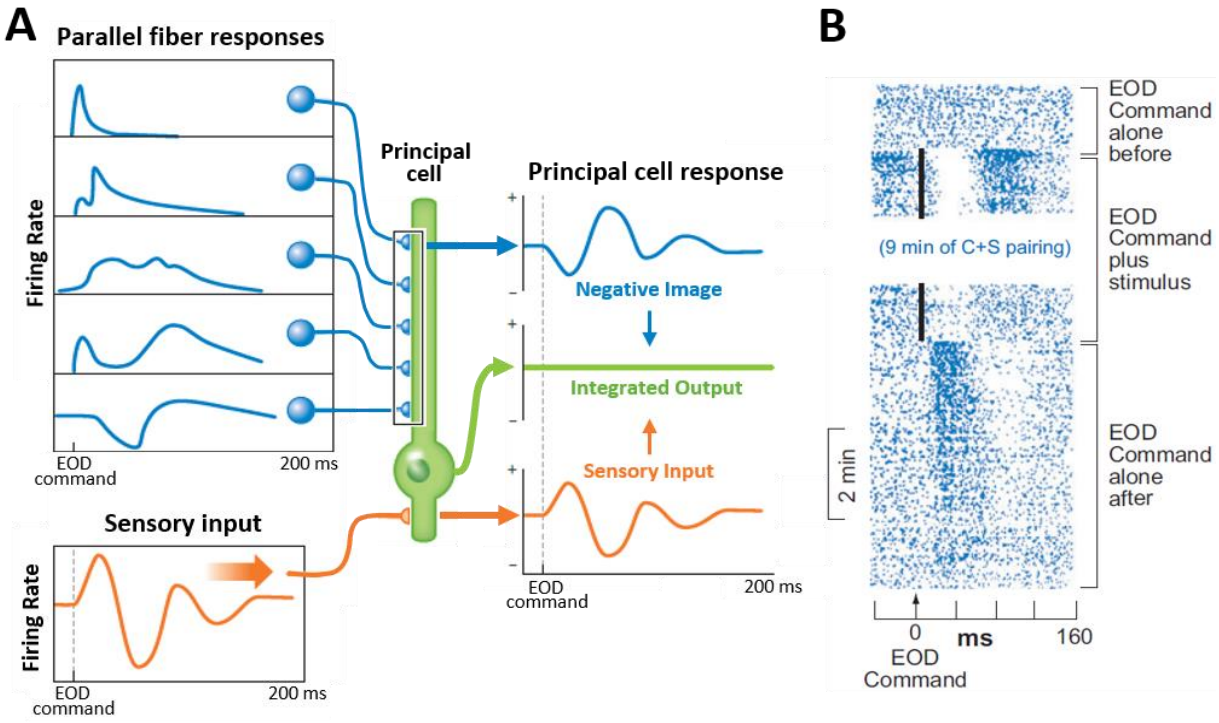

Figure 1.1. Negative image formation in the cerebellar-like structures of active electrosensory organs.

Note: **A.** Cancellation of a sensory input with its negative image assembled from the parallel fiber inputs in a principal cell. **B.** Raster display of the extracellular action potentials recorded in principal cells (receiving ampullary afferents) located in the electrosensory lobe of a mormyrid fish subjected to artificial electric stimulation. The EOD motor command initially has no effect on the cell. An electrosensory stimulus (vertical black line) that evokes a pause-burst response is then paired with the command. After several minutes of pairing, the stimulus is turned off and a response to the command alone is revealed, which was not present before the pairing and which is a negative image of the previously paired sensory response. Images adapted from Bell et al., 2008; Sawtell, 2017.

1.2. Parallelism of the cerebellum-like structures with the mammalian cerebellum

The many similarities between cerebellum-like structures and the mammalian cerebellum suggest that the latter may also be involved in generating predictions concerning expected sensory input or states of the system (Bell et al., 2008). First, the histological composition of both nervous centers is almost identical. The two possess molecular and granule cell layers with principal cells embedded in the molecular layer, that in the cerebellum are called Purkinje cells (PCs). Also, the inhibitory and excitatory interneurons like unipolar, Golgi and stellate cells are present in both organs. However, the cerebellum presents some peculiarities. It has a specialized type of stellate cells called basket cells (Castejón, 2003), which connect to PC somas through processes resembling a "basket" (hence their name). Additionally, Purkinje cells in the cerebellum connect to an additional excitatory fiber that climbs around the dendritic arborization of the cells. This climbing fiber comes from a brainstem region called the inferior olive nucleus (Palay & Chan-Palay, 1974). Typically, Purkinje cells have thousands of glutamatergic synapses with multiple parallel fibers, but only one climbing fiber makes glutamatergic synapses on an individual PC. Moreover, the cell processes (dendrites, axons) of the elements in the molecular layer of the cerebellum are strictly oriented in the sagittal plane, and perpendicular to the parallel fibers (see Fig. 1.2. for more details).

Secondly, the circuit physiology of the cerebellum and cerebellum-like structures is also very similar. The most crucial matching is that between the inputs received by the two organs. Both of them take in parallel fibers that convey a rich variety of information from multiple sources (sensory and/or highly cognitive inputs). Also, both receive a secondary input (from peripheral sensors in cerebellum-like structures and from climbing fibers in the cerebellum) that relays specific information which subdivides the set of principal/Purkinje cells that share the same parallel fiber inputs (Bell et al., 2008).

Thirdly, several studied functions associated to the cerebellum are akin to the functions analyzed by the adaptive filter framework in cerebellum-like structures. The most classical example is the vestibulo-ocular reflex (VOR) researched from the mid 1970's (Ito, 2012). In the mammalian VOR model, the cerebellum has a direct influence in the reflex pathway that adjusts the eye position whenever the head movements cause an image to sweep across the retina (also called 'retinal slip'). The movements of the head are reported by the vestibular system on the inner

ear in mammals. The nature of this model is that the proprioception of the head is used to reduce errors in an unrelated sensory modality such as vision, in an open-loop fashion that requires a transformation of one sensory modality to another. This open-loop compensation, having both the predictive information from the vestibular system and the motor command of the eye muscles reaching the cerebellum, is an echo of the adaptive filter operation already described for electrosensory fishes (Dean, Porrill, Ekerot, & Jörntell, 2009).

The predictive capability demonstrated by the cerebellum and cerebellum-like structures have led to the hypothesis that they implement forward control models (Sawtell, 2017). In these models, both the motor commands and the current state of the system (like appendage positions or velocities) are used to predict the system's future state. By comparing the predicted and the actual system states (i.e. cancelling the negative image with the sensory input), an error signal is computed and is fed back to the generator of the motor command, thus correcting its inaccuracies for the next action. Then again, for this model to be adaptable in face of sensory changes, it requires synaptic plasticity inside the cerebellar elements as shown already with the adaptive filter. One advantage of forward models is their ability to explain fast and coordinated movement sequences, given that feedback from peripheral sources is very slow (Bell et al., 2008). To a certain extent, the forward model can also explain classic symptoms of cerebellar degeneration, like the uncoordinated tremors while doing precise motor tasks, or the inability to rapidly adjust the motor commands to abrupt and steady changes in sensory inputs. Forward models are also successfully applied in robotics to implement motor control algorithms (Floreano, Ijspeert, & Schaal, 2014). Despite the compelling evidence in its favor, the top-to-bottom perspective of this model still lacks the explanation of the cellular and circuit mechanisms that originate its cerebellar computing properties.

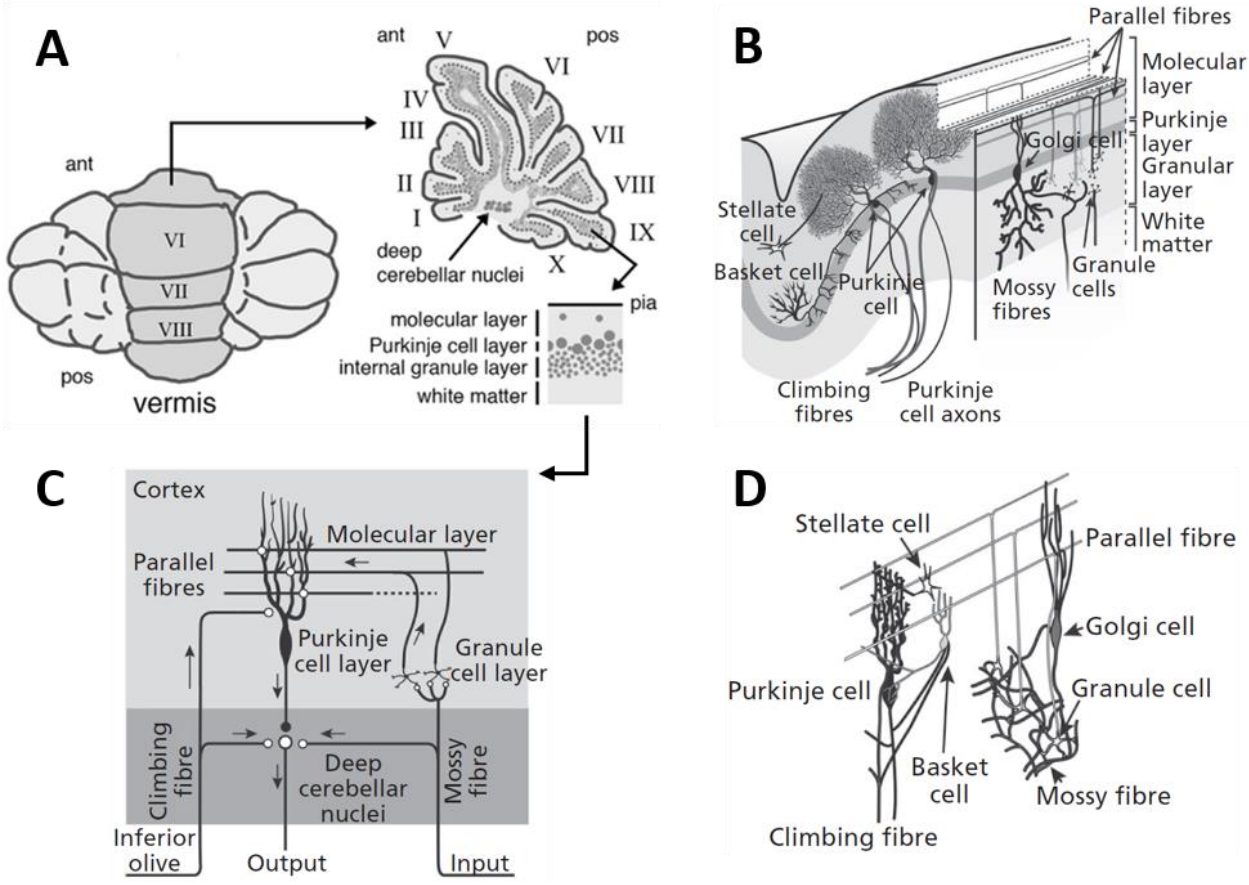

Figure 1.2. The mammalian cerebellum: histology, cellular connectivity and the cerebellar cortex motif.

Note: **A.** Illustration of a mouse adult cerebellum. A uniform layering of cell types can be found throughout the vermis and more lateral hemispheres (shown in schematic parasagittal section): the Purkinje cells layer separates the molecular layer from an internal granule cell layer. Deep cerebellar nuclei (GABAergic and glutamatergic neurons) lie within the white matter. **B.** 3-D illustration of the crystal-like structure of the cerebellum. Purkinje, stellate and basket cells in the molecular layer have their processes constrained to parasagittal planes. Purkinje cells receive input from the numerous and densely packed parallel fibers that run at right angles to the Purkinje cell dendrites and make up the bulk of the molecular layer. Parallel fibers are the axons of the billions of granule cells that make up the bulk of the cellular layer beneath the Purkinje cells. Granule cells receive input from many parts of the brain via the mossy fibers. Climbing fibers are the only other input pathway. **C.** Schematic circuit diagram of the cerebellum. Mossy fiber inputs branch from the cortex, as do climbing fibers from their origin in the inferior olive. Both converge with Purkinje cell outputs onto the deep cerebellar neurons. **D.** The cerebellar cortex motif further simplified: the mossy fiber / granule cell / parallel fiber / Purkinje cell pathway is illustrated. The true complexity of the connectivity would be better shown by having 100,000 mossy fibers and 4.6 million granule cells on the input side for the single Purkinje cell output neuron. Given these ratios, it is apparent that granule cells make up the majority of cells in the cerebellum, but also that the input pathway goes through an information expansion step between mossy fibers and granule cells. Image adapted from (Basson & J Wingate, 2013; Montgomery & Bodznick, 2016).

1.3. Cerebellar dynamics elucidated through electrophysiological experiments

In the search for linking the cerebellar circuit dynamics and its emergent functional attributes, many authors have studied the cerebellum using a variety of methods. Initially, most of the research at the cellular and circuit levels was done using electrophysiological techniques in acute models, like decerebrated cats or cerebellar slices. The biggest exponent on these initial stages was the Eccles´ research group in the 1960s, located in the University of Canberra (Australia). By using intracellular recordings with glass microelectrodes and complementing with electron microscopy, they identified the elements responsible for glutamate-mediated excitation (granule cells, mossy and climbing fibers) and GABAergic inhibition (basket, stellate, Golgi and Purkinje cells) in the cerebellum (Palay & Chan-Palay, 1974). At the end of that decade, their findings were synthesized in the first theoretical model of the cerebellar cortex circuitry by both Marr and Albus (1969-1971), which predicted the relevance of synaptic plasticity as a memory element involved in cerebellar learning. Later, some of the model predictions were supported by the finding of long-term depression (LTD) in synapses between parallel fibers and Purkinje cells (Ito & Kano, 1982). This bottom-to-top approach was a phenomenal start for explaining cerebellar physiology, that led directly to the research of its connection to behavior (as the VOR model). However, the model made many assumptions on the cellular physiology in the cerebellum that had to be tested.

As Purkinje cells were found to be the main target of the inputs reaching the cerebellum, and with their size facilitating electrode recordings, most of the initial cellular research of the cerebellum has focused on understanding how these cells relay information in the cerebellar cortex. The most productive researcher in this field has been Rodolfo Llinas, who studied in detail the electroresponsiveness and related ionic conductances of these cells (Llinás & Sugimori, 1992). In his experiments, he found a clear difference between the somatic and dendritic compartments of Purkinje cells. For instance, dendrites had responses to inputs associated to Ca^{2+} conductances, whereas the soma had all-or-nothing responses associated to Na^{+} conductances (Llinás & Sugimori, 1980a, 1980b). Their work led to the understanding of the electric effects that inputs have on the Purkinje cells, which are separated into three types: (1) the electrotonic contribution of excitatory and inhibitory potentials from parallel fiber and interneurons synapses, (2) the all-or-none Ca^{2+}-dependent spikes in the dendrites generated by climbing fibers (named complex spikes;

CS), and (3) the Na^+-dependent action potentials in the somas (named simple spikes; SS) modulated by the balance between inhibitory and excitatory inputs.

One of the biggest surprises encountered with Purkinje cells was that they transmitted a GABAergic output to distant cells inside the cerebellum, into a region called the deep cerebellar nuclei (DCN; see Fig. 1.2.C). The convention at that moment was that long cell projections in the nervous system were all excitatory (Ito, 2012). Moreover, it was known that Purkinje neurons outnumber the cells in the DCN at least by an order of magnitude, meaning that multiple PCs inhibit a single DCN cell (Fig. 1.3.). Since Purkinje cells have a high baseline activity *in vivo*, it is a challenge to reconcile how this massive inhibition from populations of PCs can modulate the activity of its DCN targets. More recently, experiments using dynamic clamp techniques to simulate PC inputs over recorded DCN cells have given insights over this conundrum (Gauck & Jaeger, 2000; Person & Raman, 2012). What appears to allow the DCN cell output to overcome this inhibition is an interplay between the synaptic weight of the PC-DCN synapses, the synchronicity of the PC inputs and the assembled silent periods from the PC activity (with the resulting effects depicted in Fig. 1.3.C). As a consequence of this population effect of PCs into DCN cells, there is a need to record activity simultaneously from multiple Purkinje neurons in the cerebellum to elucidate the type of information that is conveyed to the DCN.

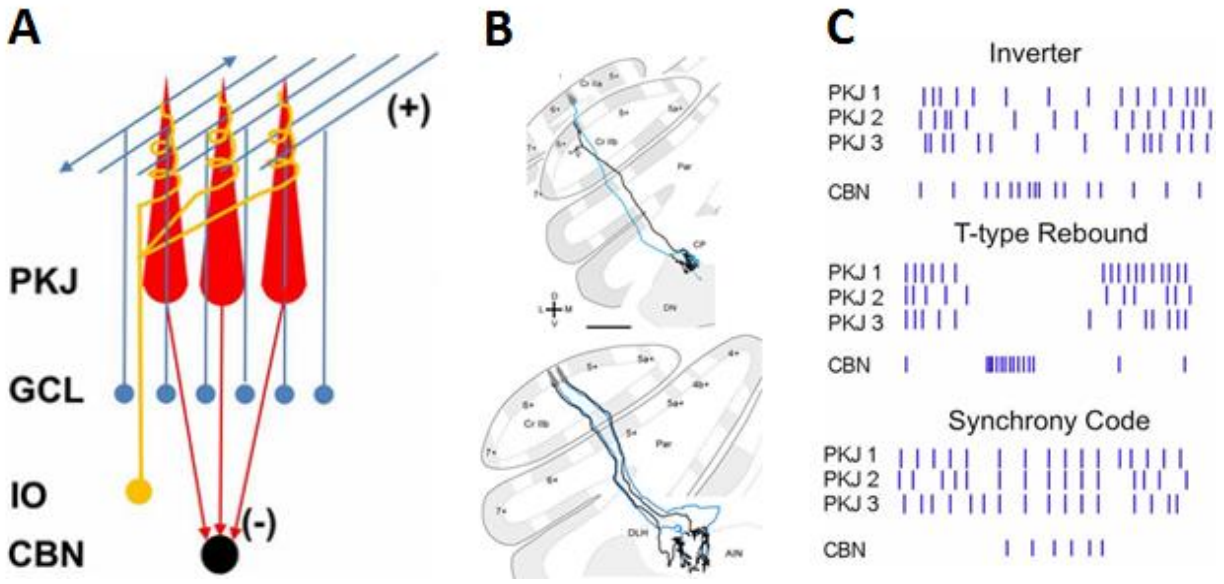

Figure 1.3. Convergence of Purkinje cells GABAergic output into the deep cerebellar nuclei

Note: **A.** Diagram representing the connection of multiple Purkinje cells onto a single DCN cell. The most recent estimation of the PC-DCN effective convergence ratio (in mouse) is of maximum 30:1 cells (Person & Raman, 2012). **B.** Reconstruction of the axonal projections of Purkinje cells in the cerebellum of mice visualized in horizontal planes. *Top:* Purkinje cells on the same sagittal plane (visibly overlapping in this horizontal perspective) with their axons reaching the same spot in the deep nuclei. *Bottom:* Two pairs of Purkinje cells from another region. PCs on contiguous sagittal planes (non-overlapping cell bodies) have their projections reaching different deep nuclei regions, adapted from Sugihara Izumi et al., 2008 **C.** Schematized spike rasters showing the key features of three non-mutually-exclusive models of Purkinje cell regulation of nuclear cell firing. Nuclear cell spikes reflect responses to three afferent Purkinje cells. Inverter, nuclear cell firing rate varies inversely with the assembled Purkinje cell firing rate. T-type rebound, nuclear cells are largely silenced by Purkinje cell activity, but fire bursts of action potentials driven by low-voltage-activated Ca^{2+} currents when Purkinje cells stop firing. Synchrony code, nuclear cells are silenced by asynchronous inhibition but produce short-latency spikes after IPSPs from synchronous inputs (adapted from Person & Raman, 2012).

1.4. Calcium imaging as a research tool for studying the cerebellar circuit dynamics

Although electrical recording offers high temporal resolution with outstanding signal to noise ratios, it is an invasive technique that damages the cerebellar tissue and that cannot acquire data from a high number of cells. Even advanced electrophysiological recording techniques, such as tetrodes and multielectrode arrays, cannot record cells just a few microns far from their sensitive sensors and cannot distinguish the absolute positions of the cells responsible for the signals (Harris, Quian Quiroga, Freeman, & Smith, 2016). However, with the advent of imaging methodologies neuroscience has developed alternative measurements of activity using fluorescent indicators that allow less invasive experiments and a higher number of cell recordings, albeit with a loss of signal time precision. Nowadays, the most used probes for imaging are the calcium indicators, since calcium is an intracellular messenger that has an essential role in neuronal communication, e.g. synaptic transmission with voltage-activated calcium channels (Grienberger & Konnerth, 2012). There are two types of fluorescent Ca^{2+} indicators typically used for neuronal imaging: the chemical indicators and genetically encoded calcium indicators (or GECIs).

Commonly used chemical indicators are Oregon Green BAPTA-1 (OGB1) and fura-2, as both the brightness and the Ca^{2+} binding properties from these indicators make them well suited for recording in neurons. First, they have K_D values just above the normal Ca^{2+} baseline concentration of cells (50-100 nM), allowing a good usable range of their Ca^{2+}-dependent fluorescence changes. Second, they have only one binding site to Ca^{2+}, which simplifies the decoding of fluorescence changes into calcium changes. And in the case of fura-2, there is a shift in wavelength emission upon Ca^{2+} binding that can be used to obtain a 'ratiometric' of the real

intracellular Ca^{2+} concentration. Nevertheless, one disadvantages of chemical indicators is that they have to be loaded into cells. Some synthesized variants of these indicators facilitate the loading process by using an acetomethylester (AM) functional group that confers liposolubility to the molecule. These lipophilic variants are then perfused on the cells of interest so they can cross the cell membrane. Once inside the cell, the endogenous activity of internal esterases cleaves the -AM radical and frees the original hydrophilic compound, effectively trapping it inside the cell (Takahashi, Camacho, Lechleiter, & Herman, 1999).

The other type of Ca^{2+} indicators widely used in imaging are GECIs. These indicators are chimeric proteins designed from the fusion of functional blocks present in other calcium-sensitive and fluorescent proteins. The most recognized family of GECIs are GCaMPs (currently in their sixth iteration; Chen et al., 2013; Helassa, Podor, Fine, & Török, 2016). These proteins are composed of parts of the jellyfish' green fluorescent protein (GFP), the Ca^{2+} binding motif of calmodulin, and a peptide coming from a myosin light chain kinase (M13); the last "P" stands for protein (Nakai, Ohkura, & Imoto, 2001). The main advantage of these indicators relies in their proteinic nature, as they can be conveniently encoded into artificial genes for cell expression. At the moment, four methods are used to express the GCaMP gene with a cell-specific transcription promoter: (1) in utero electroporation of a plasmid containing the GCaMP gene, (2) creation of a transgenic animal line, (3) transfection with a viral construct encoding the gene (M. Z. Lin & Schnitzer, 2016), and (4) a combination of the two previous methods using a site-specific recombination system (e.g. Cre/Lox) to ensure specificity of the expression (Sługocka, Wiaderkiewicz, & Barski, 2017). Currently, the most used GECI in the Ca^{2+} imaging domain is GCaMP6f (Hudson, 2018). Its brightness and Ca^{2+} affinity are very close to commonly used chemical indicators like OGB1 (Yamada & Mikoshiba, 2016). So, an obvious question arises: which one should be chosen as a reporter of Purkinje cell activity?

Each Ca^{2+} indicator has both advantages and disadvantages. The expression systems for GCaMP6f allows for targeted "loading" of the indicator in very specific cell-types *in vivo*. In contrast, the alternative method using perfusion of OGB1-AM (multibolus loading) unselectively labels all cells and cellular compartments where the molecule can diffuse, resulting in less contrasted images with more heterogeneous loading of the indicator (Franconville, 2010; Sullivan, Nimmerjahn, Sarkisov, Helmchen, & Wang, 2005). This impairs the quality of the imaging to resolve genuine signals above the background noise (Wilt, Fitzgerald, & Schnitzer, 2013).

Moreover, chemical indicators like OGB1 are cleared out from cells over time, whereas ensures the GCaMP6f transgene continuous expression. The latter extends the usable period of the fluorescent cells, enabling chronic experimentation on the animals (Grienberger & Konnerth, 2012). Lastly, our lab has already prior experience working with both methods (Astorga et al., 2015; Franconville, 2010) and it was concluded that the daily multibolus loading of AM compounds attains a less reliable labeling of the cells. Comparatively, the GCaMP expression system was more efficient. In the case of this thesis, there was an extra advantage of using GCaMP since the modified mice lines and viruses used for those previous projects were available in our lab. However, despite these advantages of GECIs there is a major complication. Current GECIs show a steep non-linear response to calcium that distort the fluorescence signals at both low and high calcium concentrations (Chen et al., 2013; Eilers, Callewaert, Armstrong, & Konnerth, 1995; Kano, Rexhausen, Dreessen, & Konnerth, 1992), whereas organic indicators only present nonlinearity at high calcium levels. Although this is an unavoidable difficulty, there are ways to extract information from these distorted signals that will be discussed below. For the moment, even with the notorious nonlinearities of GCaMP6f, this calcium indicator is able to report moments of high or low activity in cells *in vivo*.

The advantages of *in vivo* Ca^{2+} imaging are well-suited for studying the populational information of neurons in the cerebellum. To date, this method has been more frequently applied to monitor the Ca^{2+} signals associated to the activity of granule cells (deep in the cerebellar cortex) and Purkinje cell dendrites (on its surface) via 2-photon microscopy (Gaffield, Amat, Bito, & Christie, 2015; Giovannucci et al., 2017; Najafi, Giovannucci, Wang, & Medina, 2014a, 2014b; Ozden, Dombeck, Hoogland, Tank, & Wang, 2012; Zariwala et al., 2012). However, there are very few studies focused on the cells between this two depths of the cerebellar cortex, such as the molecular layer interneurons (MLI; Astorga et al., 2015; Franconville, Revet, Astorga, Schwaller, & Llano, 2011) and Bergmann glial cells (Hoogland & Kuhn, 2010). Surprisingly, there is no publication with *in vivo* recordings of spontaneous Ca^{2+} imaging in Purkinje cell somas, considering their pertinence in the integration of the cerebellar cortex output. This lack of information might have been caused by the indications that PC somas have very small calcium signals in response to direct depolarization (Callewaert, Eilers, & Konnerth, 1996; Eilers et al., 1995; Gruol, Netzeband, & Nelson, 2010; Tank, Sugimori, Connor, & Llinas, 1988) or to action potentials triggered by mossy fiber stimulation (Gandolfi et al., 2014) in cerebellar slices.

Nevertheless, in view of the proposal that Purkinje cell pauses are carriers of information to the DCN (instead of the spikes themselves), and considering the current advancements on *in vivo* techniques and analysis (Theis et al., 2016) that optimize data acquisition and quality, it might be possible to extract functionally relevant information from Purkinje cells somatic Ca^{2+} imaging.

In this thesis, we test the potential use of somatic calcium imaging in Purkinje cells as a faithful reporter of the cell's electrogenic output. We also assess the coordination of Purkinje cells predicted by the confined GABAergic connectivity in the cerebellum, which is anatomically organized along sagittal planes.

2. METHODOLOGY

The thesis is separated in two broad sections defined by the experimental methodologies. The first part corresponds to the slice experiments made in rats, which allowed us to extract data with high number of repetitions and with very low confounding variability. The insights obtained from the slice work were used to design experiments with mice *in vivo*, as they have much more logistical complexity and more difficult interpretation.

2.1. Common consumables

2.1.1. Animals

Rats: Pregnant Sprague-Dawley Rats were bought from Janvier Labs® and kept in a conventional animal house with a normal light-dark cycle (12 h/12 h), with food and water given ad libitum. The newborn rats were left with their mother until the day of the experiment.

Mice: For most of the experiments, two transgenic mice lines with knock-in of a Cre recombinase were used: one with the Cre associated to the expression of the parvalbumin promoter (PV-Cre), and the other through the Purkinje cell specific protein 2 (L7-Cre). The lines were kept in colonies dating from February 2011 (PV-Cre) and June 2013 (L7-Cre) inside the clean room facilities at the University Paris Descartes. The first generation came from strains sold by the Jackson Laboratories™, B6;129P2-Pvalbtm1(Cre)Arbr/J and B6.129-Tg(Pcp2-cre)2Mpin/J respectively.

2.1.2. External solutions

Along the work of this thesis, we used two types of solutions to keep the exterior of the nervous tissue under the closest physiological conditions. A bicarbonate-based solution (BBS) detailed in Table 2.1., and an HEPES-based solution (plainly identified with HEPES solution) described in Table 2.2. For *in vivo* extracellular recordings and stimulation, a concentrated volume of Alexa 594 (1 M) was added to the HEPES solution to allow for imaging of the electrode with the 2-photon microscope in order to better monitor the position of the electrode. The final concentration of Alexa was 50 µM.

Table 2.1. Bicarbonate-buffered external solution (BBS).

Chemical	*Stock*	*Quantity for 1 liter*	*Concentration [mM]*
NaCl	Powder	7.59 g	130
KCl	Powder	0.18 g	2.4
$NaHCO_3$	Powder	2.18 g	26
NaH_2PO_4	Powder	0.16 g	1.3
Glucose	Powder	1.8 g	10
$CaCl_2$	1 M	2 ml	2
$MgCl_2$	1 M	1 ml	1

Note: The final osmolarity was 300 mOsm. The solution was constantly bubbled with a 95/5 O_2/CO_2 gas mixture to maintain its pH and thereby avoid precipitation of divalent cations.

Table 2.2. HEPES-buffered external solution (HBS).

Chemical	*Stock*	*Quantity for 1 liter*	*Concentration [mM]*
NaCl	Powder	7.71 g	132
KCl	Powder	0.3 g	4
$NaHCO_3$	Powder	0.21 g	2
HEPES	Powder	2.38 g	10
Glucose	Powder	4.5 g	25
$CaCl_2$	1 M	2.5 ml	2.5
$MgCl_2$	1 M	1 ml	1

Note: HCl (1 M) was added to the solution in drops of (~10 µl) until reaching a pH of 7.4. Osmolarity was 300 ± 5 mOsm. The solution was kept frozen at -20°C and thawed when used.

2.1.3. Anesthetic solutions

For general anesthesia the mice were administered via intraperitoneal injections with a solution of ketamine (15 µg per gram of animal) and xylazine (10 µg per gram) diluted in isotonic saline solution and kept at 4°C. For hypodermically administered local anesthesia used in surgeries, we used a mixture of 0.1 ml of lidocaine (20 mg/ml) diluted to 1 ml with saline solution.

2.1.4. Viral solutions

Two lots of AAV2/1.CAG.Flex.GCaMP6f.WPRE.SV40 (100 µl with titer of 7.6e+12 GC/ml) bought from the U. Penn. Vector Core (material transfer agreement) were aliquoted to 5 µl volumes and stored frozen at -80°C. For each viral injection session, a new aliquot was diluted in isotonic saline solution to the following concentrations: PV-Cre animals required a dilution between 1/100 to 1/50 to have a high expression after three weeks of expression L7-Cre animals required higher concentrations ranging from 1/40 to 1/20. The diluted solutions were kept at ~4°C until the time of injection.

2.2. Acute brain slice experiments

2.2.1. Rat cerebellum slice preparation

Sagittal slices from the vermis of rat's cerebellum were prepared using the protocol already established in the lab (Llano, Marty, Armstrong, & Konnerth, 1991). Rats from 11 to 36 days old were sacrificed by decapitation under the anesthetic effects of isofluorane. Then, the cerebellum was carefully exposed from the skull and the vermis was cut apart from the hemispheres with a disposable blade. The dissected vermis was extracted from the tissue with a planar lancet and submerged in ice-cooled (~4°C) BBS solution bubbled with 95% O_2 and 5% CO_2. The extracted portion was rapidly cleaned with forceps under a stereoscope to remove the residual meninges adhered to its surface. After cleaning, the tissue was taken out of the solution and glued with cyanocrylate (Loctite® SuperGlue) to a metallic base of a Leica® VT1200S vibratome. Once inside the vibratome, the tissue was again submerged in more cold BBS solution and 200 um slices were cut by advancing the blade at a rate of 0.05 mm/s.

Each slice was taken out of the vibratome stage and put over a resting net inside a heated bath with more bubbled BBS solution at 34°C. The slices were left to recover for 30-45 minutes and then moved to room temperature before performing experiments.

2.2.2. Electrophysiological recordings in slices

The recording chamber was continuously perfused at a rate of 1-2 ml/min with BBS. Recordings were made at room temperature. The Purkinje cell layer and the molecular layer of the cerebellar cortex were visualized using an Axioskop microscope (Zeiss®) equipped with a 63X/0.9 water immersion objective (Zeiss®). Signals were recorded with an EPC-10 amplifier with Patchmaster software v2.32 (HEKA®). Borosilicate glass pipettes were pulled using a two-step vertical pipette puller (HEKA® PIP6) and had an open tip resistance of 3-5 MΩ for cell-attached and whole-cell recordings. The cell-attached recordings were made in voltage clamp mode with BBS in the pipette and 0 mV holding potential.

For experiments in which $GABA_A$ receptors were blocked with antagonists, the normal BBS used in the bath perfusion was changed to a BBS containing gabazine diluted to 10 µM.

2.2.3. Calcium imaging in slices

Purkinje cells were loaded with internal solution containing diluted OGB1 (see Table 2.3.) through a whole-cell voltage clamp for ~20 minutes, then the pipette was retracted slowly. When the leak currents where minimal and only the capacitive currents remained (indicating the initiation of an outside-out patch), the pipette was retracted faster and the membrane resealed, thereby trapping the indicator inside. Probe-loaded cells were illuminated with a 470 nm LED controlled with an Optoled system (CAIRN®). Light from the LED was sent down the epifluorescence pathway of the microscope and reflected off from a T495LP dichroic mirror (Chroma™) onto the preparation. Then, the fluorescence signal coming from the sample passed through the mirror and an emission filter (Chroma™ ET525/50M), before it was detected with an ANDOR® iXON CCD camera (model 887) at a frame-rate of 31.5 Hz.

Table 2.3. Internal solution for Ca^{2+} imaging in slices.

Chemical	*Stock*	*Quantity for 20 ml*	*Concentration [mM]*
K-Gluconate	Powder	0.82 g	175
Na2-ATP	Powder	0.022 g	2
Na2-GTP	Powder	0.0042 g	0.4

Chemical	*Stock*	*Quantity for 20 ml*	*Concentration [mM]*
HEPES	Powder	0.048 g	10
EGTA	Powder	0.0076	1
$CaCl_2$	1 M	2 µl	0.1
$MgCl_2$	1 M	48 µl	2.4

Note: KOH (1 M) was added in drops of 10 µl until the solution reached a pH of 7.4. Osmolarity was 327 ± 5 mOsm. The solution was frozen at -20°C and thawed when used. Oregon Green BAPTA-1 solution (OGB1, 1 M) was added to get a final probe concentration of 50-100 µM with a ~ 10% dilution of the internal solution.

2.3. *In vivo* experiments

2.3.1. Two-photon imaging

Two custom-made set-ups were used for scanning 2-photon imaging, each of them adapted for experiments in anesthetized or awake animals; however, both shared the same basic configuration (Fig. 2.1.A). A Ti-Sapphire laser from SpectraPhysics® was employed as a high-power source of infrared laser. The laser was conducted with Thorlabs® mirrors into a Pockels cell where its intensity was modulated (ConOptics™ 350-80BK with amplifier 302RM). The resulting light was expanded with a telescope made of Thorlab® lenses to decrease the beam density and it was directed to a set of two mirror galvanometers (Cambridge Technology™ Galvanometer XY Set model 6221H) to modify the X and Y positions of the beam in the sample's optical plane. Then, the laser light passed through a dichroic mirror (Chroma Technology™ 670DCXXR) with a cut-off wavelength of ~ 670 nm and went into a water immersion objective (Olympus® XLUMPlanFL-N 20x/1.00 W). The measured point-spread function (PSF) of the microscope had a full width at half maximum (FWHM) of 1 µm in the X and Y dimensions, and 10 µm in the Z direction. In a region inside this volume, the sample is bathed with a high enough density of photons to allow the 2-photon excitation of the fluorophores. The absorbed energy in these molecules is then released with an Stokes shift, emitting a photon with a lower energy than the total energy absorbed, but that has a higher wavelength than the excitation light. The fluorescent light gets scattered while traversing the sample, and some of it is captured by the objective. The incoming light from the objective passes again to the dichroic mirror, and only the

short wavelengths produced by the fluorophores are reflected to a Photomultiplier tube (Hamamatsu® PMT H7422-40). The resulting electrical signals from the PMT were transformed into ultra-fast digital pulses by an edge detector (Hamamatsu® C9744). Such pulses were individually counted by a National Instruments® card (NI - BNC2090A) and sent to a desktop computer. The data was processed using Igor Pro 6.37 with the "NIDAQ tools MX" external operation software, in conjunction with the Igor2P repository developed by Brandon Stell, (Stell, 2015/2018).

To easily locate the positions of interest on the surface of the animal for the imaging, an additional hot or cold mirror (BrightLine® FF735-Di02-50x36) was put between the galvanometers and the dichroic mirror to extract some of the incident light into an USB camera (PCO® Pixelfly, or Thorlabs® DCC1545M). An extra light source (any general lamp) was used to illuminate the tissue.

Over the course of this thesis, a device to add more I/O control to the Hamamatsu® PMT was made available (M13414). This device allows software control of the PMT over-voltages, which are dangerous to the equipment and occur regularly while doing *in vivo* imaging. However, no power supply nor interface were included on the product. So, a simple circuit was designed to add these functional blocks, plus protection circuits. The design was manufactured and tested in real experiments.

Two different software were used as the graphical interfaces to control the devices, make real-time images and record the signals. For the experiments using anesthetized animals, the set-up available worked with Igor Pro 6.37 (Wavemetrics™) with the Igor2P module (Stell, 2015/2018). For the experiments with awake animals, the set-up used the open-source Python-based platform of ACQ4 (Campagnola, Kratz, & Manis, 2014). Both programs were capable of I/O control of all devices through the NI card.

2.3.2. Behavioral set-up components

The set-up used for awake experiments had some additional features that were fundamental for its imaging capability and behavioral tests. First, the stability of the mouse's head was critical to reduce movement artifacts while imaging. The best arrangement consisted of a structure of two Ø 2.5 cm steel columns holding a Ø 1.3 cm horizontal bar in the front of the animal, while a secondary Ø 1.3 cm steel column with an angle clamp was used on the back (all from Thorlabs®).

In the middle of the horizontal bar, there was a customized pressure clamp designed to restrain the headpieces of the mouse. An extra metal piece was cemented to the animal on the back of its head to improve stability by clamping it to the secondary back column.

The other additional feature in the set-up was the use of a 3D-printed plastic wheel with a mesh flooring, so that the animal could run while imaging its cerebellum. The wheel was positioned in the center between the steel columns, at an optimized position to allow the access of the immersion objective to the animal (see Fig. 2.1.C). The movements of the wheel were captured using a rotary encoder (CUI Inc.™ AMT112S-V) attached to the rotation axis of the running wheel, and directly connected to the NI card.

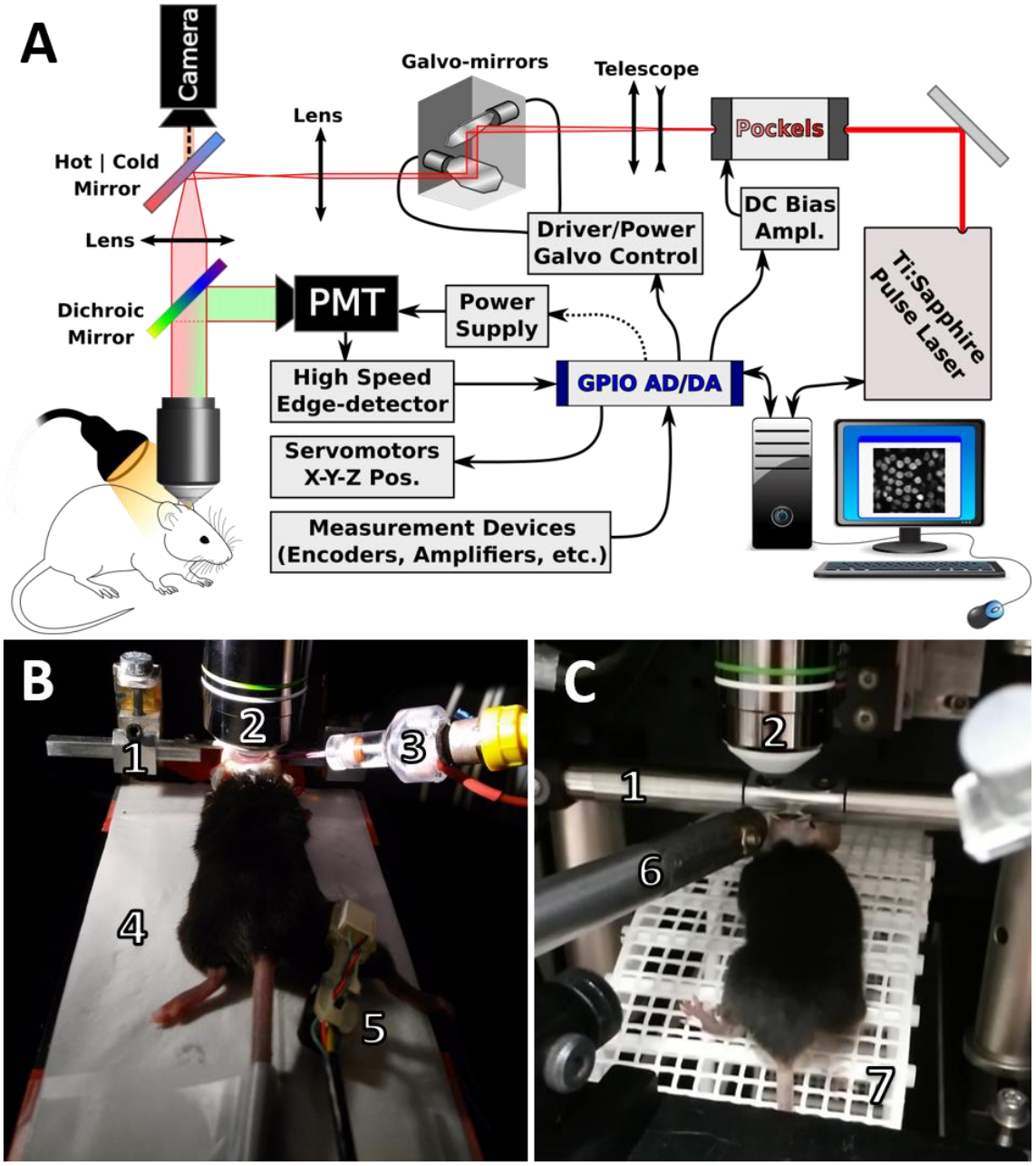

Figure 2.1. Experimental set-up configurations.

Note: **A.** Diagram showing the basic functional structure for the scanning 2P microscope with photon counting. **B.** Set-up arrangement for experiments with the anesthetized animal. **C.** Set-up arrangement for behavioral experiments. 1: Horizontal metallic bar, 2: Objective, 3: Electrode holder, 4: Platform with thermal pad, 5: Pulse oximeter, 6: Back clamp, 7: Running wheel.

2.3.3. Viral injections in mice

Transgenic animals (PV-Cre and L7-Cre) between 40 and 60 days old were anesthetized by intraperitoneal injection (IP) of ketamine/xylazine (see Solutions above). After 5-15 minutes, once the effect of the anesthesia lulled the animal and it didn't move voluntarily, its head was shaved with a disposable surgical blade and then the animal was mounted in a stereotaxic frame. It was of utmost importance to restrain the head of the animal tightly on the frame to avoid mechanical displacements for the next steps. No additional oxygen could be provided to the animal throughout the procedure because the clamps of the stereotaxic frame blocked the access of our ventilation mask to its nostrils. The level of anesthesia in the animal was checked from time to time by the involuntary muscle contractions in response to mild pinches given to its posterior paws.

Given that the ketamine/xylazine combination produces a dysregulation of the autonomic system in rodents (Gaertner, Hallman, Hankenson, & Batchelder, 2008), accompanied with a low metabolic rate from subsequent mild hypoxia, the anesthetized animal was kept at around 34°C. At this temperature, the thermoregulatory disorder caused by ketamine might be reduced (M. T. Lin, Chen, & Pang, 1978) and is not too hot to cause unwanted effects such as heat spikes or accelerating the metabolism of the animal leading to more hypoxia. The animal's temperature was maintained by a system of a rectal thermistor and heat plate controlled from an FHC® DC Temperature Controller.

With the animal on position, its head was cleaned with iodine solution (Betadine®) and a sagittal cut on its skin was made to uncover both the parietal, interparietal bones, and a third of the trapezoidal muscles (just above of the occipital bone). To ease the accessibility for the upcoming steps, the insertions of the neck muscles (trapezoidal, splenius and semispinalis muscles) were partly cut and the muscles were put aside with an absorbent cotton tip. When strong hemostasis was needed, various hemostatic composites were used (Ethicon® Surgicel, Bloxang®).

Once the skull was exposed, the tilt of the head was corrected by leveling the coordinates of the bregma and lambda positions with the stereotaxic caliper (Fig. 2.2.). Using the adjusted bregma as an origin, the position around X = 0.5 mm, Y = -5.5 mm was marked which corresponds to the right side of the cerebellar lobule V. As the measurements of the animals were variable, another criterion was used to confirm this position by re-locating the Y coordinate at least 0.5 mm more anterior to its projection from the occipital suture (Fig. 2.2.A). On the chosen position, a hole

of diameter ~ 0.8 mm was drilled with an spherical drillbit of 0.5 mm using a Dremel® rotary tool. The hole was made deep enough to reach the dura mater, it was cleaned from all remainder bone pieces using fine tweezers and the dura was softly pierced with a syringe needle.

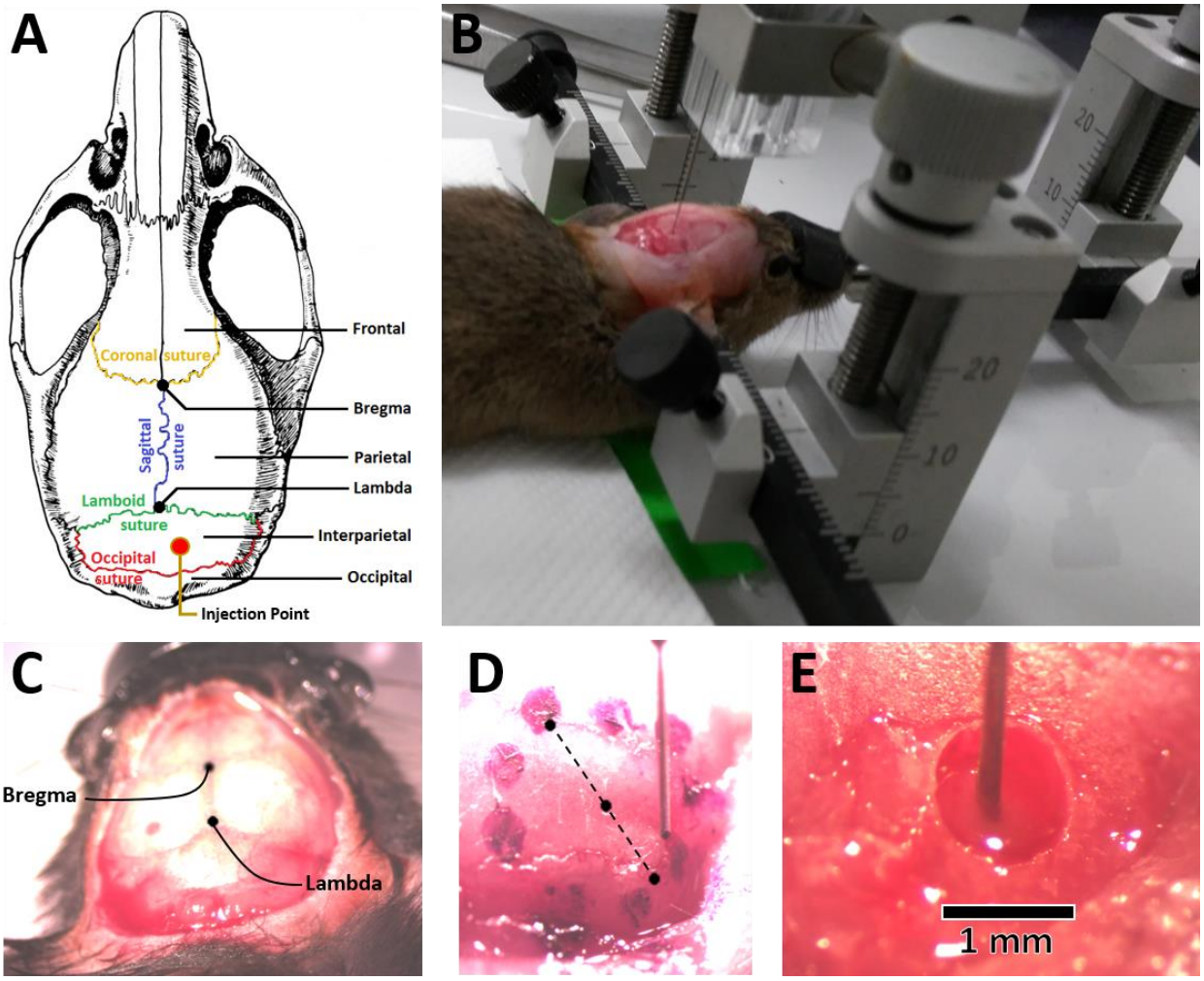

Figure 2.2. Viral injections on mice.

Note: **A.** Anatomical illustration of the main stereotaxic features used to position the injection point. Original from (Geoface, 2016). **B.** Photo of an anesthetized mouse held by the stereotaxic frame while being injected. **C.** Close-up to the exposed skull identifying the bregma and lambda positions. **D.** Example of a marked area prepared for viral injection + chronic window procedures. Diameter of 3 mm, 25x magnification. **E.** Injecting needle inserted through the drilled craniotomy at 40x magnification. Zoomed images taken with a Leica® Stereoscope MS5.

Through the opening, a WPI™ beveled needle of gauge 34 (with ~200 µm diameter) pre-loaded with 2 µl of viral solution (see Solutions) was inserted into the cerebellar tissue down to a depth of 450 µm. Extra attention was taken to ensure that the needle was getting inside the cerebellum and not only pushing the meninges, which is seen as a small tensile displacement on

the surrounding tissue. After some seconds, the needle was raised 100 µm and then 1.5 µl of viral solution were pumped at a flux of 0.1 µl/min using the hydraulic pressure of a water-filled propylene tube connected to a Hamilton® microliter syringe, in turn pushed by a Harvard Apparatus® pump model 11 Plus. Once finished, the needle was kept on the tissue for some minutes and then carefully removed.

The procedure was ended by suturing the skin wound with a resorbable thread (Ethicon® Vicryl Rapide). The animal was removed from the stereotaxic frame and put under an incandescent lamp until it recovered consciousness. In the meantime, a hypodermic injection of isotonic saline solution was given to the animal to compensate for dehydration and/or loss of blood volume during the procedure.

2.3.4. Anesthetized (acute) experiments

Transgenic animals expressing GCaMP6f for 2-3 weeks after their viral injection were anesthetized with an IP of ketamine/xylazine. Once the animal was deeply anesthetized, its head was shaved, and its skin antisepsis was done with iodine solution (Betadine®). Then, the skin between its ears was cut off to expose the parietal and interparietal bones. All the muscle insertions of the neck were gently detached with a microblade, and the remainder connective tissue was cleaned off. Special care had to be taken when cleaning the injection site, as it was still on recovery and very soft.

The head of the animal was glued with dental cement to a steel bar and secured in a metallic base as shown in Fig. 2.3. As soon as the animal was fixed, a mask with a constant oxygen flow of 1 cm^3/s was put on the animal and its blood oxygen saturation was monitored using a pulse oximeter (Starr™ MouseOx). Also, the animal's temperature was kept at 37ºC with a closed-loop controller (FHC® DC Temperature Controller). Once stabilized, a pool of cement (bigger than the immersion objective for imaging, see 2P Imaging) was made to allow the exposed cranium to be covered in HBS solution. While the skull was still dry, an aperture of ~ 2x3 mm was drilled to expose the cerebellum with its injection point on a side. Then, the area was washed profusely with HBS solution to clean the debris. The bone lid was removed slowly, as the healing tissue from the injections was always tightly adhered to the skull. Most of the time some bleeding started as soon as the bone was removed, which was held off by hemostatic composites (Ethicon® Surgicel, Bloxang®) and cotton tips.

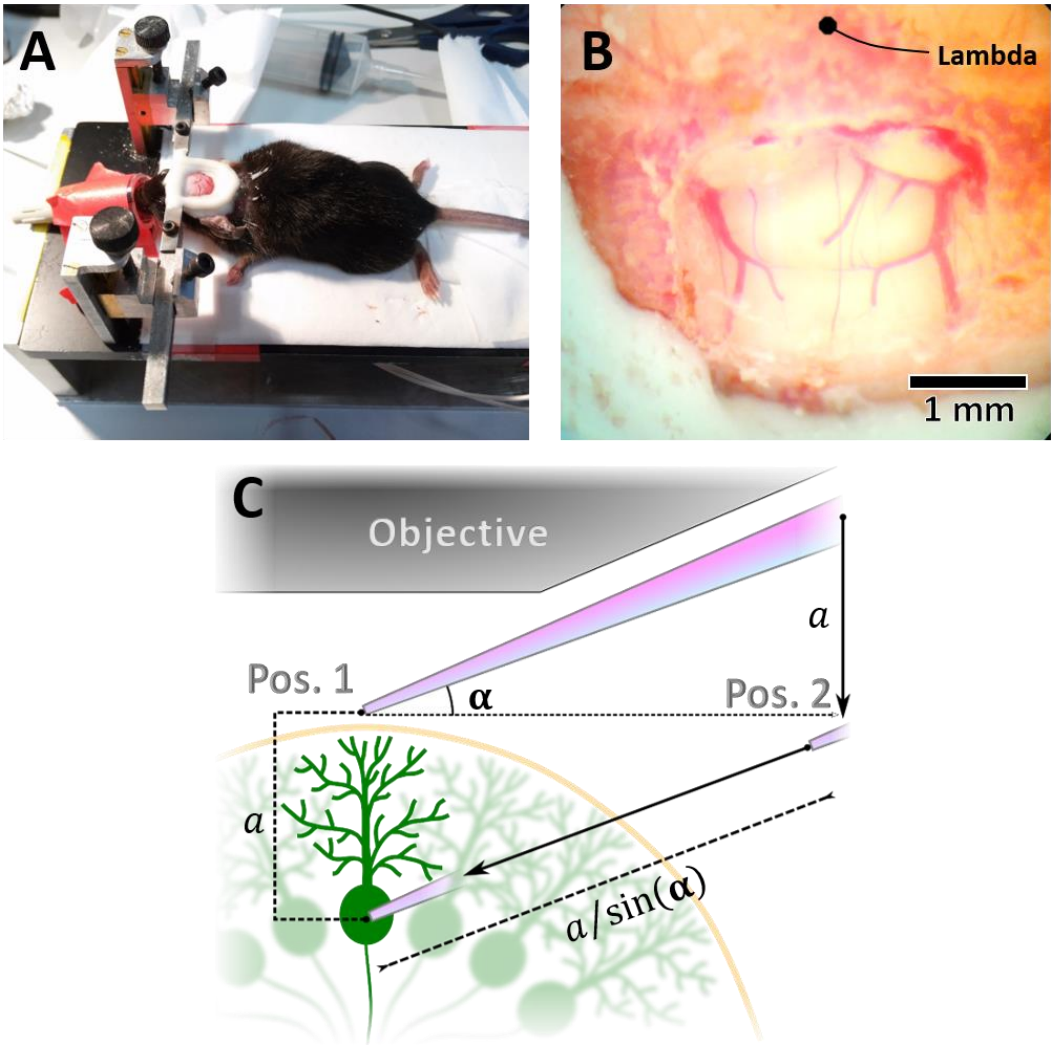

Figure 2.3. Anesthetized (acute) experiments on mice.

Note: **A.** Photo showing the set-up for holding the mouse and the dental cement pool used to keep its craniotomy immersed in solution. **B.** Magnified photo (25x) of the craniotomy showing is overall size and location. **C.** Diagram showing the procedure to position the electrodes inside the cerebellum (description in text).

Usually, a portion of the meninges got ripped off from the injection point in the process of opening the skull. That area was not used in experiments. For procedures requiring cell-attached recordings of Purkinje cells and extracellular stimulation of parallel fibers, the meninges were completely removed using a fine lancet and the craniotomy was covered with agar (0.04 g/ml) made with HBS solution (see Solutions). Once finished, the animal was positioned on the 2P imaging set-up to conduct the experiments (Fig. 2.4.B).

2.3.5. *In vivo* cell-attached recordings with calcium imaging

To perform a simultaneous recording of both the extracellular electrical behavior of the cells and their concomitant internal calcium signals, a glass electrode with a long-shank was needed to fit in the interstice between the objective and the cemented pool on the animal's brain while reaching into the tissue. A two-step vertical pipette puller (HEKA® PIP6) was adjusted to pull for a longer distance in its second step and make asymmetrical electrodes. The temperatures of each step were calibrated until pipettes of ~ 1 cm shank and Ø 3-5 µm of opening were obtained. To ease the filling of the electrodes, borosilicate glass capillaries with internal glass filament were used (Hilgenberg® length 80, Ø outside 1.5, wall thickness 0.225, all in mm). For the filling of the pipette, the tip was immersed in the supernatant of a centrifuged HBS solution with Alexa 594 (see Solutions), and then a negative-pressure was applied to the other end through a tube and a syringe until the shank was filled. Then, the rest of the internal solution was injected through the wider end of the pipette. The final resistance of the electrode was around 30 MΩ.

To place the electrode onto a target cell selected for imaging, additional preparations were needed. The angle of the electrode holder in the set-up was adjusted so that the direction of entry of the glass pipette was parallel to the wall of the objective, at around 23° from the horizontal. Also, the movement of the electrode had to be controlled with micromanipulators (Luigs & Neumann™ SM-10) that measure position with low error. Given the angle and measured distances, a trigonometrical solution was employed which is depicted in Fig. 2.3.C. First, the tip of the electrode was placed directly over the target cell and as close to the surface of the brain as possible (Position 1). The distance (a) between the two was calculated from the image control software (see 2P Imaging). Then, the electrode was pulled out of the field of view in its entry direction (Θ ~ 23°) for at least a distance equal to $[a/\sin(23°)]$, before it was lowered exactly a in depth (Position 2). Finally, in this new parallel direction, the electrode was pushed into the tissue very slowly and with positive pressure to prevent clogging of the electrode and tensile displacements until the cell was reached. The detection of spikes around 1-10 Hz (from climbing fiber discharges in dendrites) marked the moment when the electrode entered the healthy tissue. Once inside the cerebellum, the tip of the electrode was followed with imaging and could be moved relative to the cell (only around 20 µm in the XY plane). The amount of error in the final position was usually acceptable if the target cells were not too deep (minimal a distance), and if the electrode entered without tissue displacements. If the electrode was not on target and the electrode wasn't clogged

the whole procedure could be repeated after retracting the pipette from the brain and adding a starting shift equal to the error of the previous try.

The electrical signals were detected using AgCl electrodes for both the direct channel (in the electrode) and ground reference (on the pool solution). An Axopatch 200B amplifier (Molecular Devices®) was used to filter (at 1 kHz; Bessel) and amplify the signal for the ADC range of a NI® card connected to a desktop PC. The 2-photon images were synchronously acquired by using the same internal clock from the card (more details in the 2P Imaging section).

2.3.6. Chronic window implantations

PV-Cre animals of 30-60 days old were anesthetized and injected with a viral solution (see Viral injections in mice). Additionally, mice were given a hypodermic injection with 50 µl of an analgesic drug (buprenorphine, 0.03mg/ml) and an intramuscular injection with 5 µl per gram of weight of an anti-inflammatory (dexamethasone, 0.7 mg/ml).

After the injecting needle was removed from the animal's cerebellum, an ink marking on the surface of the skull was made following the template of a round coverslip (Ø 3 mm), as depicted in Fig. 2.2.D. The position for the markings was chosen so that their perimeter followed the lamboid suture with the injection site circumscribed. When the marking was done, the skull was drilled (with an spherical drillbit of 0.5 mm using a Dremel® rotary tool) following an elliptical shape with its minor and major diameters bounded by the most anterior-posterior and left-right markings respectively (see Fig. 2.4.B). The drilling was stopped when the perimeter of the ellipse was deep enough to reach the dura, and the piece of bone detached from the rest of the skull and removed with fine tweezers. When bleeding occurred after bone removal, it was contained using hemostatic composites (see Viral injections in mice). The exposed cerebellum was kept moisturized with isotonic saline solution and the borderline bone pieces were carefully removed. This cleaning step was critical, both for its risk of causing more bleeding from the blood vessels on the tissue, and because the small bone pieces could pierce the tissue while inserting the window on the skull.

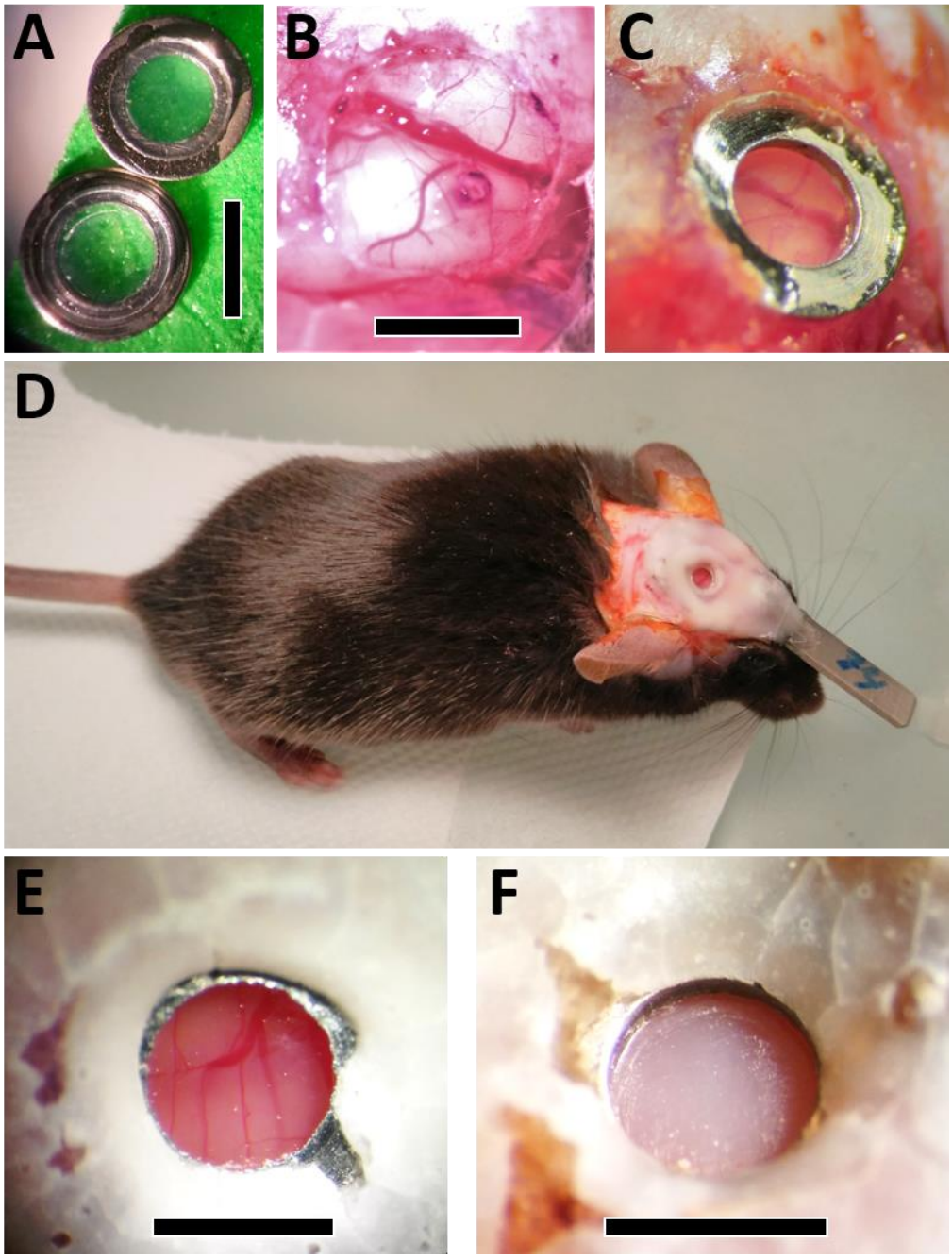

Figure 2.4. Chronic window implantations.

Note: **A.** Custom-made windows with a round coverslip glued to a metallic O-ring. **B.** Example of a craniotomy with slightly elliptical shape opened for the insertion of the window. **C.** Chronic window already implanted and adhered to the skull with cyanoacrylate. **D.** Photo of a mouse after recovery from the implantation, with one head piece cemented to its skull. **E.** Example of a healthy chronic window keeping its transparency after several days of recovery from the surgery. **F.** Example of an opaque chronic window from an unsuccessful surgery made the same day as E. Zoomed photos taken at 40x magnification. All the scale bars correspond to 3 mm.

The window was previously prepared by gluing a Ø 3 mm glass coverslip with a metallic O-ring of Ø 4 mm and around 0.2-0.3 mm of thickness (Fig. 2.4.A) using tissular adhesive (3M® VetBond). The window was inserted on the elliptical hole through its major diameter, at least until its border was not protruding from the surface of the skull. The metallic O-ring was then adhered to the bone using cyanoacrylate (Loctite® SuperGlue). Once the adhesive was cured, the skull of the animal was dried with compressed air and a custom headpiece made of stainless steel was glued using strong dental cement (SunMedical® Super-Bond C&B). The rest of the exposed skull was covered with normal dental cement (GC Fuji I®).

Finally, the animal was put under an incandescent lamp for recovery. In the meantime, it was given one hypodermic injection of 1 ml of isotonic saline solution and an IP with 10 µl/g of antibiotic (enrofloxacin, 0.1 µg/ml).

2.3.7. Running wheel experiments in awake mice

The animals with implanted chronic windows were anesthetized using a vaporizer (VetEquip™) set up at an air flow rate of 1 liters/min with 3% isofluorane for the first induction. The extra isofluorane gas was discarded with a pump filter system (RWD™ R546W). After sedation, the animal was held on a table with a ventilation mask using 1-2% of isofluorane and its window was gently scratched to regain transparency using a stereoscope. The mouse was removed from the table and it was quickly clamped on the running wheel set-up (see Fig. 2.1.C) before it awoke from the anesthesia.

To monitor the movement artifacts generated by the animal's locomotion, we exploited the secondary peak wavelength for 2-photon absorption of GCaMP6f at ~ 820 nm (see Fig. 2.5.). Under this stimulation wavelength, all the GCaMP6f molecules with or without bounded Ca^{2+} are excited, so the final emitted fluorescence is not calcium dependent. In consequence, we recorded two sets of images from the animals: (1) with a 910 nm laser stimulation that reported the [Ca^{2+}] intracellular changes, and (2) with a 820 nm stimulation that showed a constant fluorescence only modified by the tissular movements and proportional to the 2P excitation/emission conditions and the GCaMP6f concentration. Given that these two excitations are very different in terms of average power and diffraction on the tissue, they could only be compared in relative terms by using dF/F normalizations.

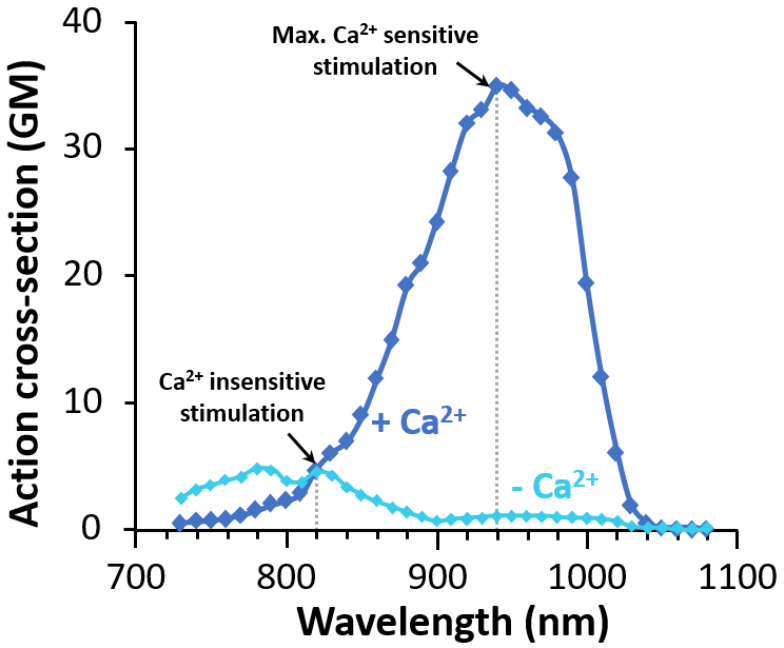

Figure 2.5. Two photon excitation spectra for GCaMP6f.

Note: Action spectra are determined by comparison to fluorescein. Adapted from Janelia, 2018. + Ca^{2+}: Spectra with saturating calcium concentration. - Ca^{2+}: calcium free spectra. A very similar action spectra for a closely related protein, GCaMP6m, is published by (Barnett, Hughes, & Drobizhev, 2017).

The animals were used for imaging experiments two weeks after the chronic window implantation. Animals were imaged immediately after this recovery period to fully profit from the time window before overexpression of the GCaMP6f started. To motivate the animal to run on the recordings, an air puff was delivered to its back via a silicon tube attached to an air duster. Once finished, the animals were put back in their cage and received a food reward.

2.4. Data Analysis

All of the analysis was performed in Igor Pro 6.37 (Wavemetrics™). In general, all data analysis relied on the following methods:

- Image analysis calculating the mean pixel signals inside hand-drawn regions of interest (ROIs) were done by using the Igor2P repository developed by (Stell, 2015/2018).
- Image registration for reducing movement artifacts on *in vivo* 2-photon recordings was performed using the built-in function "imageregistration" in Igor Pro.

- Extraction of spikes and raster plots from electrophysiological recordings was done with the Neuromatic package version 2.9j using user-defined thresholds.
- All optimization of fitting models to the data was implemented with an iterative least-squares method using the built-in "optimize" function in Igor Pro, set up with the quasi-Newton method for line search steps and a Hessian with finite differences (for details, refer to Igor Pro 6.37 documentation).

2.4.1. Change-point detection in time series based on differentiation

To extract the fluctuations of the fluorescence data from Purkinje cells loaded with OGB1 in slices, we first denoised the signal using a binomial smoother with a window of 10-50 points depending on the noise amplitude (see "smooth" function in Igor Pro). Then, we used the second derivative of the smoothed trace to reveal the extremum points of the signals. The identification of the change-points in the traces was done by the extraction of the first crossings points above an arbitrary threshold for positive and negative incursions of the second derivative trace.

2.4.2. Correlation analysis of imaging data in slice experiments

Imaging recordings in slices with at least two Purkinje cells were segmented into 20 second recordings. ROIs were drawn on the Purkinje somas to extract their mean fluorescence signal per frame. The fluorescence signals were smoothed and their second derivative was calculated by using the change-point detection method based on differentiation. The Pearson's correlation coefficient (r-value) between pairs of second derivatives coming from simultaneous recordings on different cells were calculated and assigned to a group composed of synchronous pairs (seen in Fig. 2.6.B as the center diagonal with blue dots). In the same way, Pearson's r-values were also calculated for asynchronous recordings between cells (shuffled or non-unities), which corresponds to the rest of the dots (in red) inside the matrix shown in Fig. 2.6.B. Once the matrix was completed, a Student t-test (unpaired, one-tailed, with different sample sizes) was performed between the means of the unity and the non-unity groups to determine the significance of any possible correlation between the two pairs of cells. If a significant difference was found (with α=0.05), it was interpreted as the cells having coordination of their activities.

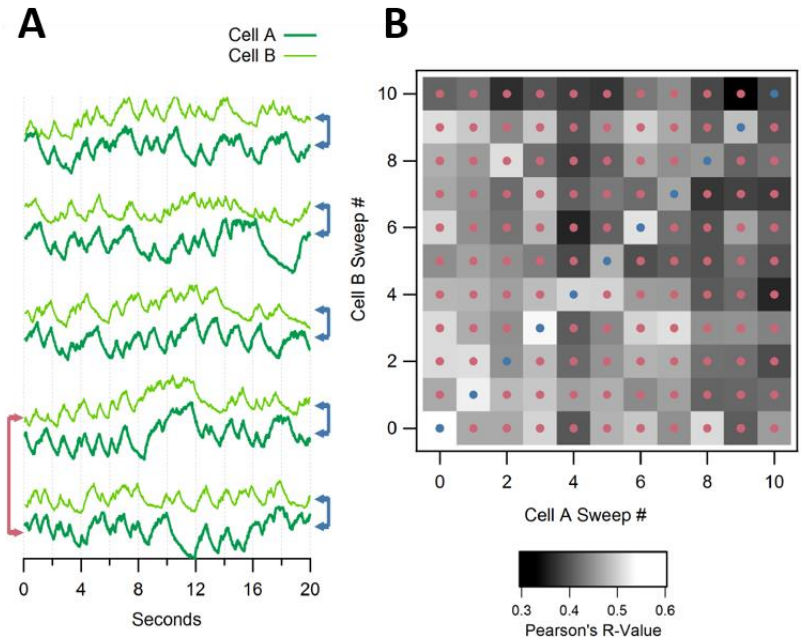

Figure 2.6. Illustration of the correlation analysis for calcium imaging in Purkinje cells on slices.

Note: **A.** Simultaneous calcium recordings from two cells. Blue arrows indicate correlations between paired recordings from 2 cells and the pink arrow indicate correlations between shuffled recordings. **B.** Matrix of Pearson's correlation coefficient calculated for all simultaneous recordings (unity line / blue dots) and shuffled recordings (pink dots). To determine whether there was a correlation between two cells, a Student's t-test was performed between the resulting populations of simultaneous (unities) and shuffled (non-unities) correlation coefficients and a significant difference was interpreted as a significant correlation. Figure taken from (Ramirez & Stell, 2016).

2.4.3. Correlation analysis of electrophysiological data

Raster plots were created by detecting threshold crossings using the package Neuromatic (Rothman & Silver, 2018) in Igor Pro. Interspike intervals (ISIs) were calculated by differentiating the spike timings of the rasters. We considered the median as the parameter that best reflects the central tendency of the ISI distributions. Then, we defined pauses as silent times that lasted more than three times the median (in other words, missing at least two simple spikes), to avoid detecting irregular spiking patterns caused by jittered or misfired spikes. Windows of one median ISI were then attached to the beginning and end of pauses in individual recordings, and if these windows overlapped in simultaneous recordings they were considered to be synchronous transitions. We then randomly reordered the trains of recorded ISIs 500 times for each recording and performed the same analysis to find the simultaneous transitions when the ISIs occurred randomly. This

randomization process produced a normal distribution of overlapping transitions to which we compared the number of simultaneous transitions that were recorded in the experiments. This permutation test (also known as Monte Carlo test) allowed us to evaluate whether the coordinated pauses in Purkinje cell spiking were significantly different from random coincidences by performing a one-sided Z-score test with α=0.001 (Ramirez & Stell, 2016).

2.4.4. Change-point detection in time series based on slope threshold

The differentiation method to detect slope changes used in slice experiments was not very efficient for the analysis of *in vivo* Ca^{2+} imaging data. Derivatives are quite able to measure the local, short-time changes in the slope of time series (towards an infinitesimal limit). However, our *in vivo* recordings have significant noise embedded in them that substantially hinders these changes on the derivatives. Because of this, the data has to be previously denoised to reduce the spurious changes created by the noise, but this process also causes blurring of the changes in the derivatives we sought to recover. This generates a bias of the differentiation method towards the detection of very abrupt changes, disregarding slow changes even if they are visibly greater than the noise (for an example, see Fig. 3.8.).

To avoid this, a new heuristic method arbitrarily called envelope thresholding was designed to avoid the use of derivatives, and its algorithm is explained in the flowchart of Fig. 2.7. The algorithm requires (1) an already denoised signal $F(t)$, (2) an estimation of the noise amplitude, that in our case were confidence intervals approximated from gaussian noise ($W \sim N(0, \sigma 2)$ and Z-score * σ), and (3) a priori knowledge the maximum duration of the changes to identify (T_{thres}). A graphical example is shown in Fig. 2.8. to illustrate the functioning principle of this algorithm. In the first stage of the algorithm, the signal has to be denoised [$F(t)$] and its noise envelopes are calculated as $F(t) \pm Z_{score} * \sigma$ (assuming a gaussian-type noise). Then, $F(t)$ is transformed into $F^*(t)$ by projecting a horizontal line from each point of $F(t)$ and extracting the "hitting time" when the signal crosses the noise envelopes (ΔT_{cross}). Self-crossing of $F(t)$ with itself or projections where there are no possible crossings are invalid. To avoid extremely high values from very long projections (with no changes) all ΔT_{cross} values are inverted and then stored into $F^*(t)$. In the second stage of the algorithm, the change-points are detected as the zero-crossings of $F^*(t)$ that are also bigger than $1/T_{thres}$. Overall, this heuristic method detects points where the signal

$F(t)$ changes its slope for more than a minimal threshold given by the uncertainty of the noise and the time duration of the expected changes.

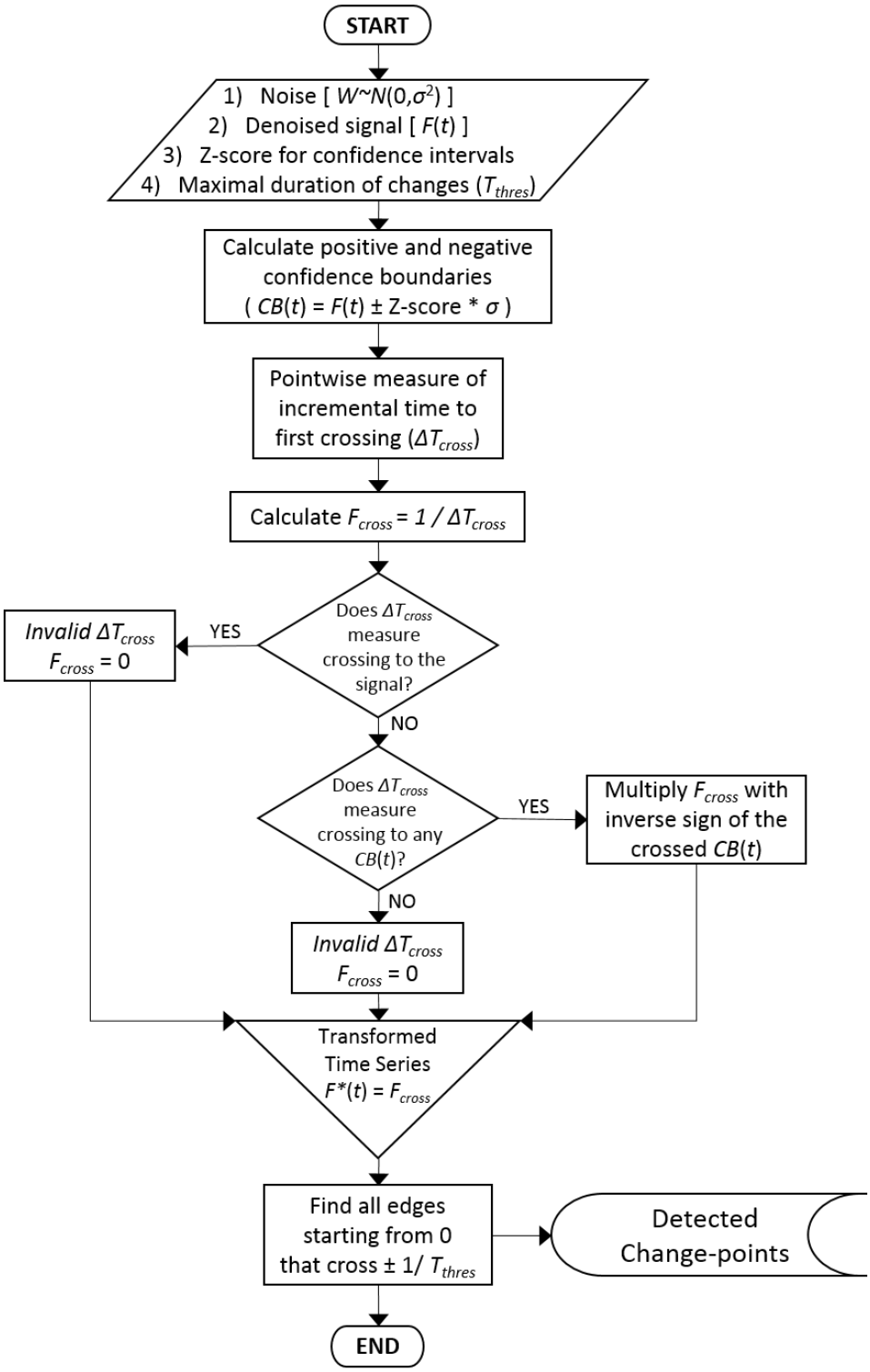

Figure 2.7. Flowchart of the envelope threshold algorithm used to detect changes in time series.

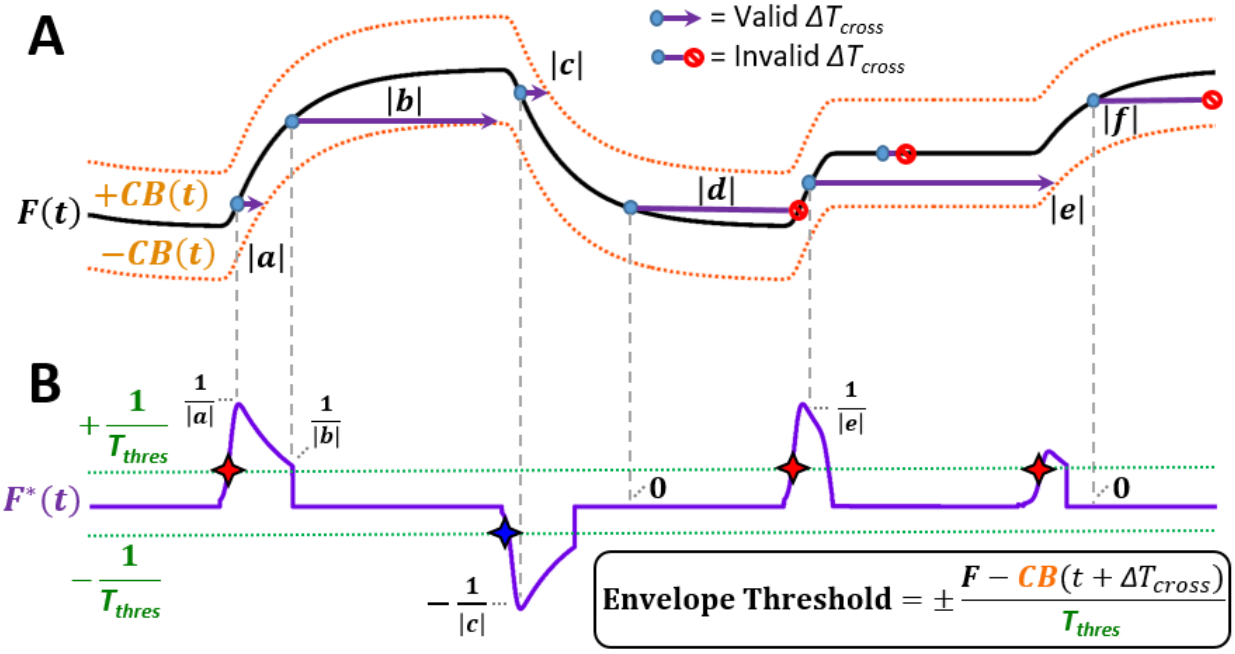

Figure 2.8. Illustration showing the envelope threshold algorithm.

Note: **A.** Simulated time series [$F(t)$] and confidence interval boundaries [$\pm CB(t)$] with an exemplary set of time crossings ΔT_{cross} = {a - f}. **B.** Transformed time series $F^*(t)$ calculated from the traces in A. Each ΔT_{cross} example has been projected into its corresponding transformed point in the trace (F_{cross}). The edges of $F^*(t)$ that start from 0 and cross the time threshold ($\pm 1/T_{thres}$) contain the slope change-points (marked as red/blue stars).

2.4.5. Correspondance between fluorescence signals and spiking activity of Purkinje cells

One of our goals was to recognize the relationship between the somatic Ca^{2+} signals reported by fluorescent indicators and the spiking activity of Purkinje cells extracted with cell-attached recordings. There are three mechanisms that govern this relationship: (1) the calcium entry to the intracellular space through voltage-dependent sources activated by each action potential spike, (2) the clearance mechanisms in the cells that pushes the calcium concentration to baseline levels, and (3) the conversion of the calcium increments into detectable fluorescence signals by a Ca^{2+}-dependent fluorophore. In our case with the chemical calcium indicator OGB1, that has an almost linear fluorescence response to changes in calcium concentration in the range of the expected intracellular calcium, the relationship can be approximated to a single exponential kernel (Yaksi & Friedrich, 2006):

$$k(t) = Ae^{-t/\tau} \quad (1)$$

where A is the amplitude of the fluorescence signal generated by a single spike and τ is the time constant of the Ca^{2+} clearance mechanisms inside the cell. Consequently, if the cell generates trains of action potentials in time (codified as an spike raster [$S(t)$]), each of them will contribute a $k(t)$ amount that will summate into the output fluorescence signal (or $F_{Real}(t)$). This can also be expressed as a transfer function that has the form:

$$F_{Real}(t) = S(t) * k(t) + W(t) \quad (2)$$

where the asterisk denote convolution and $W(t)$ is the noise component on the signal.

To find the transfer function in Eq. 2 that explains the relationship between $S(t)$ and $F_{Real}(t)$, an inverse problem methodology (blind deconvolution) can be implemented. This consists in finding the parameters A and τ of $k(t)$ that minimize the least-squares distance between the estimated signal $S(t)*k(t)$ from the model and $F_{Real}(t)$ from the recordings. If the found parameters make the two functions fit adequately well, the system is assumed to be explained by this linear transfer function.

However, despite the simplicity of this linear model to explain the OGB1 signals, the known nonlinear behavior of certain Ca^{2+} indicators (as GCaMP6f) undermine its application to all cases. GCaMP6f is a genetically encoded indicator that has four binding sites to Ca^{2+} located on a modified calmodulin domain. The cooperativity of these binding sites results in a supralinear reaction with calcium that produces a response of the indicator shifted towards higher calcium concentrations (Fig. 2.9.). A sigmoidal Hill model with a slope (n) between 1.9 and 3.4 (Berlin et al., 2015; Chen et al., 2013; Helassa et al., 2016) can describe this binding reaction of GCaMP6f to Ca^{2+}.

As stated by (Akerboom et al., 2012), this nonlinearity of GCaMP-based indicators prevents the good fitting of the linear transfer function (Eq.1) by (1) underestimating the spike rate at low calcium levels and (2) overestimating it at high levels. To suppress these distortions, they adjusted the convolution output with an arbitrary nonlinear function that re-scaled their extreme limits, resulting in a better fit. Although this approach to neutralize the nonlinear portion with an arbitrary transfer function was effective for the fitting, it was not based in any biophysical interpretation of its causes.

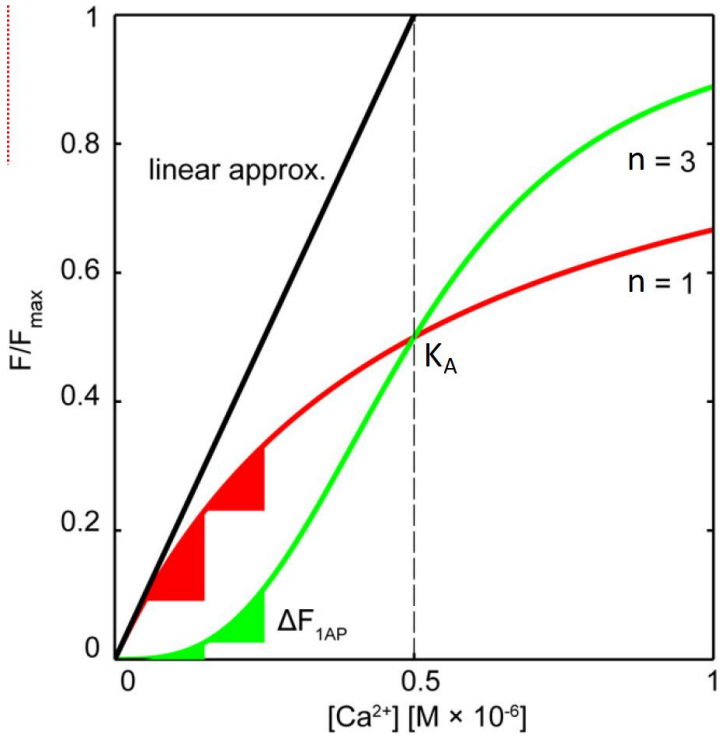

Figure 2.9. Relative fluorescent changes of two hypothetical Ca^{2+} indicators similar to OGB1 (red trace, Hill slope (n) = 1) and to GCaMP indicators (green trace, n = 3).

Note that the same absolute change in Ca^{2+} starting from different resting calcium levels will lead to very different fluorescence changes of the nonlinear indicator (GCaMP-like, green triangles) whereas the linear indicator responds with similar changes (OGB1-like, red triangles). This triangle approach, taken to its minimal limit, is approximating the derivative of the Hill curves. This means that the derivative contains information about the expected amplitude of fluorescence changes depending on the calcium level. Figure taken from (Yamada & Mikoshiba, 2016).

To make a closer approximation of the underlying model, we separated it into three subsystems (see Fig. 2.10.): (1) the Ca^{2+} entry to the cell per each spike event that can be approximated by a linear convolution (ref), (2) the nonlinear conversion of calcium concentration into fluorescence signals by the Ca^{2+} indicator and (3) the detection of the fluorescence-emitted photons by the known linear behavior of the PMT (Hammamatsu Photonics, 2007), with the added Poisson noise coming from the photon counting process (Hasinoff, 2014). Since the first and third subsystems are linear with well-known approximations, we focused on modelling the middle subsystem which holds the nonlinear behavior of the model.

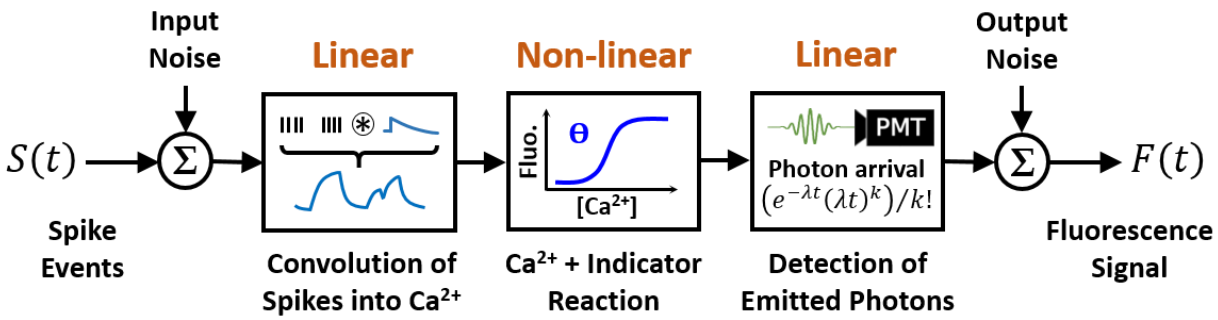

Figure 2.10. Illustration of the modeled system from the *in vivo* imaging experiments.

Fortunately, this nonlinear subsystem defined by the Ca^{2+} and GCaMP6f reaction kinetics has already been described several times in the literature (Berlin et al., 2015; Chen et al., 2013; Helassa et al., 2016) using a Hill model between the Ca^{2+} concentration in solution or $[Ca^{2+}]$, and the normalized GCaMP6f fluorescence with its minimum bounded to 0 and maximum to 1 (called θ):

$$\theta = \frac{[Ca^{2+}]^n}{K_A^n + [Ca^{2+}]^n} \tag{3}$$

where K_A corresponds to the $[Ca^{2+}]$ at half the normalized fluorescence level, and n is the Hill slope coefficient.

As depicted in Fig. 2.9., the slope of this Hill function reports the change in fluorescence amplitude that depends on the initial calcium level, which corresponds to the nonlinear relationship we seek to model. Thus, the first derivative of Eq. 3 should provide the feature of this relationship:

$$\theta' = \frac{n \cdot K_A^n \cdot [Ca^{2+}]^{(n-1)}}{(K_A^n + [Ca^{2+}]^n)^2} \tag{4}$$

Because the amplitude A of the kernel changes $k(t)$ in the fluorescence signal is going to be found iteratively, we need to scale θ' between 0 and 1 to only reflect the nonlinear changes for A. For nonlinear Hill models with $n > 1$, the function θ' has a defined maximum that can be found from its corresponding derivative:

$$\theta'' = \frac{n \cdot K_A^n \cdot [Ca^{2+}]^{(n-2)} \cdot ((n-1) \cdot K_A^n - (n+1) \cdot [Ca^{2+}]^n)}{(K_A^n + [Ca^{2+}]^n)^3} \tag{5}$$

The maximum point can be found using the defined zero-crossing of θ'':

$$(n-1) \cdot K_A^n \; - \; (n+1) \cdot [Ca_{max}^{2+}]^n = 0 \tag{6}$$

$$[Ca^{2+}_{max}]^n = K_A \cdot \sqrt[n]{\frac{n-1}{n+1}} \qquad \text{for } n > 1 \tag{7}$$

where $[Ca^{2+}_{max}]$ corresponds to the calcium concentration where the maximum slope in θ is seen. Then, we can define the scaled function θ_{Ca}, which conveys the nonlinear relationship between the amplitude of the calcium unitary response *A* and the level of $[Ca^{2+}]$ as:

$$\theta_{Ca}([Ca^{2+}]) = \frac{\theta\prime([Ca^{2+}])}{\theta\prime([Ca^{2+}_{max\_}])} \qquad \text{for } n > 1 \tag{8}$$

At this moment θ_{Ca} is only defined from $[Ca^{2+}]$, a variable we can not measure on our system. However, we can estimate it from the fluorescence signals by implementing an approximation also based on the Hill equation from (Takahashi et al., 1999):

$$[Ca^{2+}](F) = K_A \cdot \sqrt[n]{\frac{F-F_{min}}{F_{max}-F}} \tag{9}$$

where *F* is the measured fluorescence level and F_{min} and F_{max} corresponds to the minimum and maximum possible fluorescence levels the cell can achieve. Then, by combining the functions in equations 8 and 9, the non-linear transformation in terms of fluorescence results in:

$$\theta_{trans}(F) = \theta_{Ca}([Ca^{2+}](F)) \qquad \text{for } n > 1 \tag{10}$$

Finally, to get the nonlinear model we first multiply *S*(*t*) with their corresponding values of $\theta_{trans}(F(t))$, and obtain a transformed version *S**(*t*). Then, we do a convolution to obtain the final nonlinear output $F(t) = S^*(t) * k(t)$. This transformation effectively works as if the amplitudes *A* of the fluorescence signals per spike depend on the level of the estimated calcium concentration (derived from the fluorescence levels), thus it conveys the effect of nonlinear Ca^{2+} indicators (illustrated in Fig. 2.11.). The free parameters of this model are *A*, τ, F_{min}, F_{max} which were adjusted independently in the least-square optimization; and also K_A, n which were fixed to the measured values from (Berlin et al., 2015) (K_A = 390 nM, *n* = 1.95).

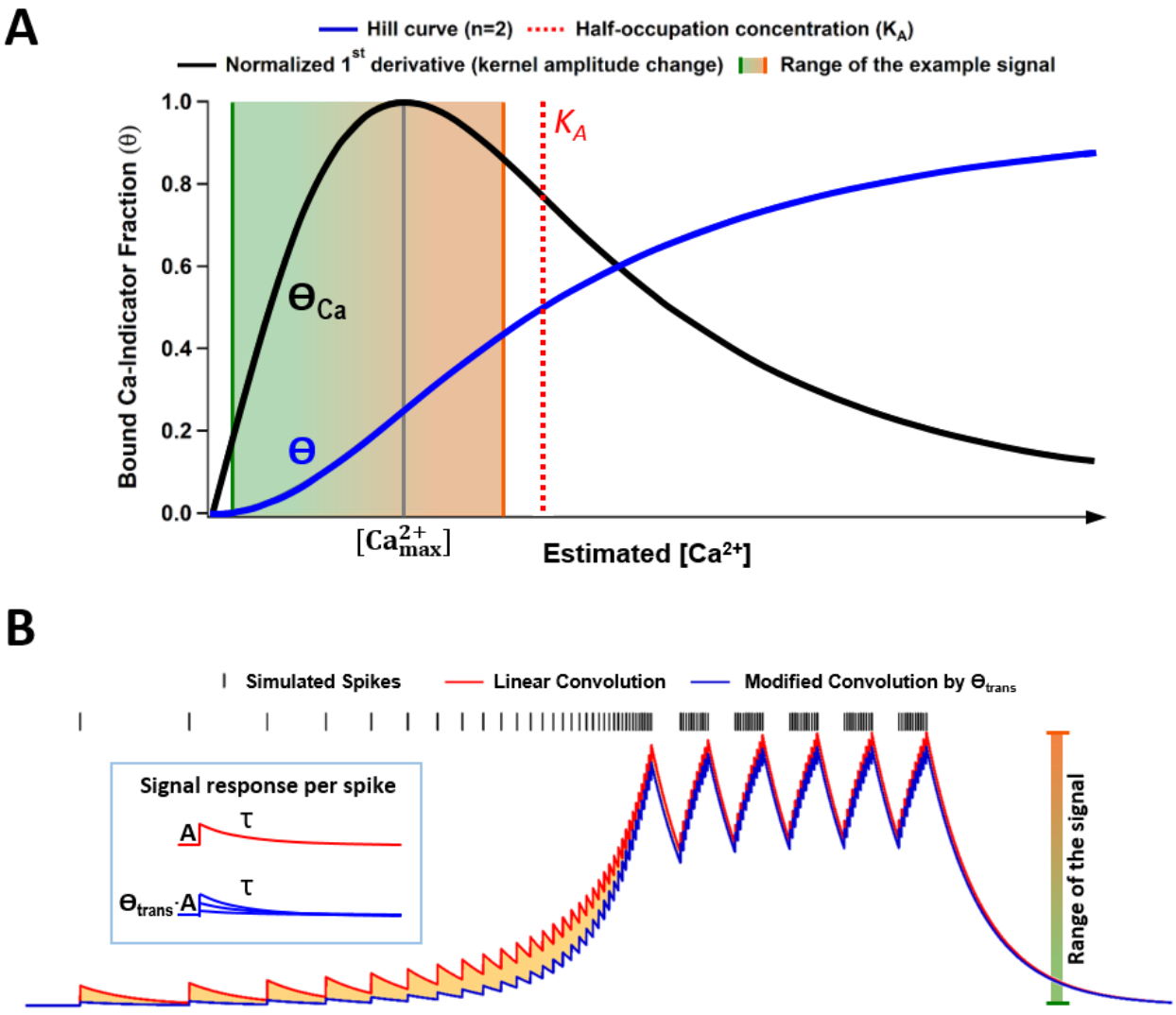

Figure 2.11. Illustration of the theta transformation model (Θtrans) modifying the kernel response to a single action potential spike.

Note: **A.** Hill curve (Θ) describing the reaction between the Ca^{2+} concentration and a theoretical nonlinear Ca^{2+} indicator with a Hill slope coefficient (n) of 2. The normalized first derivative (Θ_{Ca}) is shown in black. **B.** Comparison of the nonlinear Ca^{2+} indicator described in A (blue traces) with its linear counterpart (red traces) on the fluorescence signal from a simulated set of spikes. When the spike rate and the signal level are low, there is a big difference between the resulting signal from the Θ_{trans}-modified kernel and the conventional linear kernel. However, if the spike firing pattern keeps the range of the signal outside the nonlinear region, the two systems behave almost identical. The color scale at the right spans the range of the signal and corresponds to the color-shaded domain in A, thus showing the extent of Θ_{Ca} that modulates the kernel change amplitude.

3. RESULTS

3.1. Calcium imaging reveals coordinated simple spike pauses in Purkinje cells from slices

3.1.1. Somatic calcium imaging reports Purkinje cell simple spike activity in slices.

Our first objective was to determine whether somatic calcium imaging followed the changes in simple-spike firing rate of Purkinje cells. We started to test this possibility in slices of rat cerebellum, in which parallel and climbing fibers processes are severed during the slicing process. Under this context of reduced excitatory signals, Purkinje cells had spontaneous action potential discharges in the form of simple spikes (SS) and also spontaneous silent periods as has been previously reported (Oldfield, Marty, & Stell, 2010; Tank et al., 1988). To see if those firing patterns produced a detectable calcium signal, we performed simultaneous electrophysiological recordings (cell-attached) and intracellular calcium imaging from OGB1-loaded Purkinje cells (see section 2.2.3.), which are seen on Fig. 3.1.

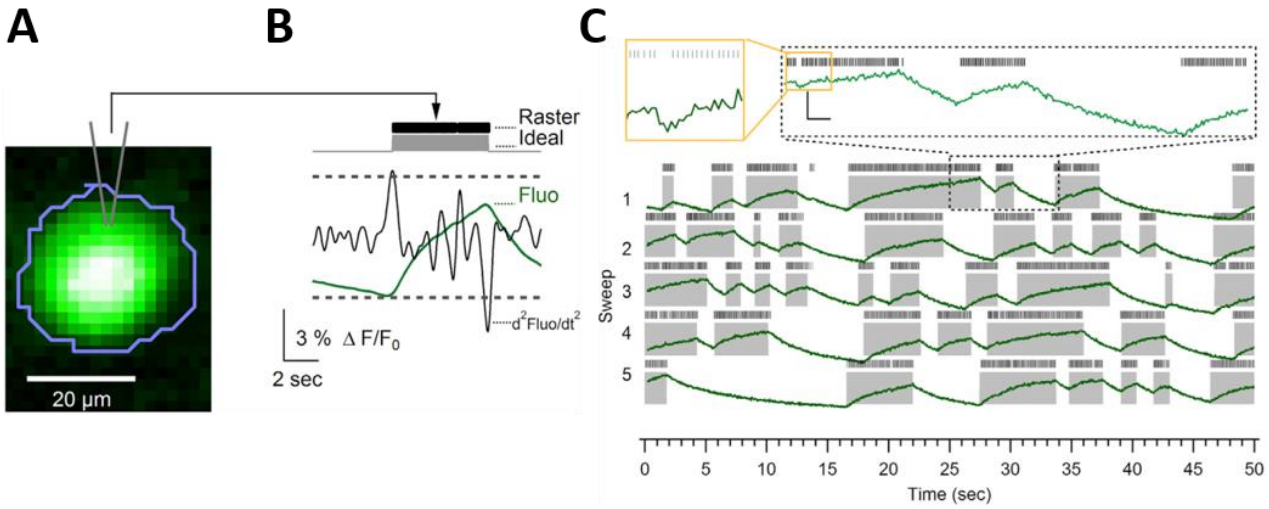

Figure 3.1. Somatic calcium dynamics relay the simple spike activity of Purkinje cells in slices.

Note: **A.** Image from a Purkinje cell preloaded with 100 µM OGB1 using a patch pipette. **B.** Raster plot of spontaneous activity from a cell-attached electrode on the same cell shown in **A** with its corresponding smoothed calcium signal (green), its second derivative (black), and the activity diagram (gray) constructed from the threshold (dashed lines) crossings. **C.** A longer timescale of the same data shown in **B**. The cell was firing with an average firing frequency of 20.3 spikes/s, and the orange inset calls out a section of the recording with an inter-spike interval of 151 ms. Scale bars of inset indicate 0.3% $\Delta F/F_0$ and 100 ms. Images taken from (Ramirez & Stell, 2016).

From these initial experiments, we observed that fluorescence increased whenever the cell was spiking, and slowly decayed when it wasn't. Also, Purkinje cells showed a stereotyped activity with two states, SS firing and complete silence, with abrupt transitions when the cell switched between them. Given the high contrast of the signals against noise (Fig. 3.1.C), we thought that simple calculus transformations, such as derivatives of the fluorescence signal, would reveal the transitions between firing and silent periods. In fact, by setting an arbitrary threshold on the second derivative from the smoothed traces, it was possible to detect those transitions with great accuracy (Fig. 3.1.B and C).

Although this heuristic tool was useful to detect transitions, it is limited to relate the extremum points between the somatic fluorescence signal and the rate of simple-spikes in Purkinje cells, disregarding other functional relationships. So, we evaluated if the somatic calcium signals were linearly related to the spike timings of the cells by applying a convolution model, which is widely used in the calcium imaging field (Henry Lütcke and Fritjof Helmchen, 2011). In this model, it is assumed that every time the cell fires an action potential a consistent calcium response is generated, and can be approximated by an exponential kernel function: $k(t) = A \times \exp(-t / \tau)$ (as seen in Fig.3.2.A). These calcium responses are summed up if their timings are close together and the result creates a bigger amplitude than each individual kernel. In our case the kernel is unknown, but we had both the simple spike timings $[S(t)]$ from the cell-attached recording and the somatic calcium signal $[F(t)]$ from the imaging. If the convolution model holds in our cells, then it would be possible to perform a blind deconvolution that finds the kernel function parameters (A and τ) that adequately fits the estimated output of the convolution $(S * k)(t)$ with the real output $F(t)$ using a least-squares optimization method (see Data Analysis for more information). We found that the convolution model fit the calcium signals recorded from Purkinje cells remarkably well, with the resulting kernel parameters of $A = 0.1 \pm 0.03\%$ $\Delta F/F$ and $\tau = 7.2 \pm 2.1$ seconds (n = 6 cells). One example of this analysis is shown in Fig. 3.2.B.

The accurate fit of the convolution model indicated that the simple spike rate is linearly related to the somatic calcium signals. It also suggested that the OGB1 loaded inside the Purkinje cells is far from being saturated, with the intracellular calcium concentration never rising much beyond the KD of the OGB1 (170 nM). If the calcium levels were higher, the majority of OGB1 molecules would have been already bounded to Ca^{2+} and only a small fraction of the indicator

would have been available to respond to new calcium signals, reducing the net fluorescence change. This effect dampens the fluorescence increments at high fluorescence levels, which would have worsened the fitting of the convolution model. The fact that the OGB1 showed no signs of saturation is in agreement with the high buffering capabilities of the Purkinje cells described in previous studies (Fierro & Llano, 1996; Fierro, DiPolo, & Llano, 1998).

Nonetheless, the fitting results also let us identify some unavoidable limitations of using the Purkinje's somatic calcium imaging as an estimator of simple-spike rate. The amplitude of the calcium response per spike was very small, suggesting it is nearly impossible to detect single spike events from the noise in the calcium imaging. Furthermore, the decay time of the calcium response is slow (on the order of seconds), reducing the resolution available to detect short pauses and subtle changes in firing rate. Nevertheless, the somatic calcium imaging could be used to estimate changes in SS firing rates despite these technical difficulties and most of the noise problems could be greatly reduced by shifting from spontaneous recordings to experiments with triggered stereotyped responses that allow averaging.

Other observations in favor of the convolution model was the relatively low variability of the kernel parameter estimation between cells, meaning that the linear relationship of somatic calcium and SS firing rates is not affected by Purkinje cell variability. To independently test this consistency, another analysis was carried out by exploiting the stereotypical activity of these cells in slices. By focusing only on the beginning of the transitions from silent-to-firing states, we could approximate the behavior of the fluorescence signal with two lines: (1) the decrement line from the end of the pause (like the one shown in Fig. 3.2.C), and (2) the increment line driven by the spikes at the beginning of firing. When the decrement line is subtracted from the increment line the resulting slope reflects only the proportional change in fluorescence caused by the spikes without the decaying component of the signal (Fig. 3.2.D). If all cells share the same linear relationship of calcium and spiking activity, the pooled results across all transitions and cells should aggregate in a line even if their firing frequencies are different, which is seen in Fig. 3.2.E. In summary, even if the somatic calcium imaging could not ascertain single simple spikes, they could be used to estimate general changes of SS firing rate through all Purkinje cells and across a wide range of firing rates.

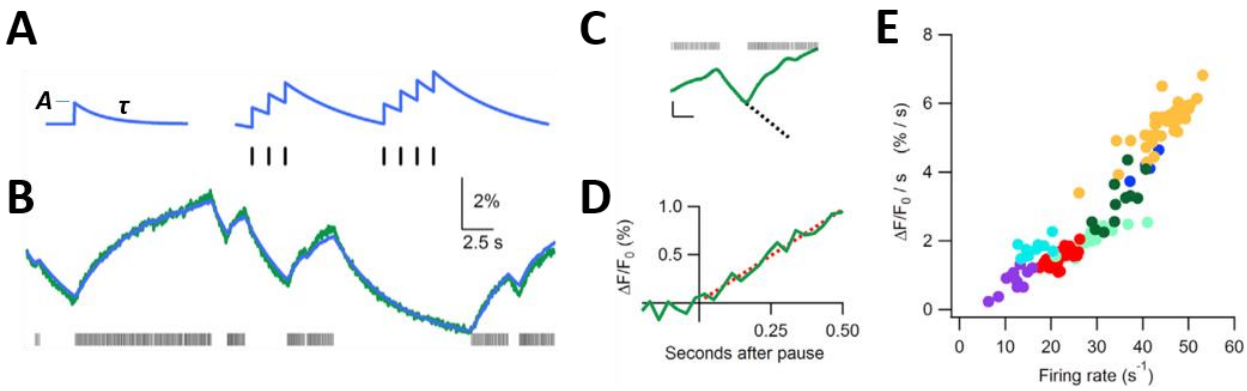

Figure 3.2. Somatic calcium signals are linearly related to firing frequency changes of simple spikes.

Note: **A.** Schematic of an idealized calcium response with a single exponential decay (on the left) and the summation of seven such responses at the times indicated by the points in the black raster plot below (on the right). **B.** Green trace shows a portion of the data from the calcium recording depicted in the first sweep of Figure R1C and the corresponding raster plot of the simple spikes recorded from the cell in cell-attached mode in black below. Blue trace shows the sum of a single exponential with a tau of 4.9 s and an amplitude of 0.06% for each simple spike in the raster plot. **C.** Smoothed fluorescence trace recorded from the soma of a Purkinje cell (green) and a raster plot of the corresponding simple spikes recorded in cell-attached mode (black). Dashed line is a linear fit to the average fluorescence recorded from the soma during the 10 frames just prior to the end of the pause in spiking. Scale bar, 10 counts and 1 s. **D.** Same data from **C** converted to $\Delta F/F_0$ using the dashed line in **C** as F_0. Dashed red line is a linear fit to the data recorded in the 500 ms following the pause. **E.** Data from seven cells (indicated by different colors; red points are from the cell shown in **C** and **D**) in which the change in $\Delta F/F_0$ during the 500 ms following a pause (slope of dashed red line in **D**) is plotted against the average firing rate (1/average inter-spike interval) of simple spikes recorded in cell-attached mode over the same period. Images taken from Ramirez & Stell, 2016.

3.1.2. Somatic calcium reports simple spikes but not complex spikes.

In addition to simple spikes Purkinje cells produce another type of spiking activity in the form of complex spikes (CS), which do not occur spontaneously in slices but could become a potential confounding signal in *in vivo* experiments. The CS originate from the activity of multiple glutamatergic synapses between a single climbing fiber (CF), a neuronal process coming from Inferior Olive (IO) cells inside the brainstem, and the Purkinje dendritic arbor. The excitation of the climbing fiber results in the widespread opening of various ion channels through ionotropic (AMPA, NMDA) and metabotropic glutamate receptors (Ohtsuki, Piochon, & Hansel, 2009), resulting in an inward current that strongly depolarizes the cell (Llano et al., 1991) and transiently increases the calcium concentration in the dendrites (Kano et al., 1992; Llinás & Sugimori, 1992). Previous studies have found that the CS-driven calcium rises are confined to the dendritic region of the Purkinje cells with just a tiny effect on their soma (Eilers et al., 1995; Kano et al., 1992). In

order to examine the potential contribution that CS signals have in the somatic calcium fluctuations, we performed electrical stimulations on climbing fiber axons with simultaneous calcium imaging of their connected Purkinje cells (preloaded with OGB1; see section 2.2.3.).

When the CF was electrically stimulated, a calcium spike was triggered in the dendritic arborization of the Purkinje cell and only a very small fraction of this calcium signal reached the center of the soma — as expected by previous reports (Eilers et al., 1995; Kano et al., 1992). Specifically, the CF stimulation generated a conspicuous calcium spike of 36.2% ± 5.4% ΔF/F (n = 12 cells) in the dendrites, with a much smaller response in the soma of just 1.9% ± 0.2% ΔF/F as illustrated in Fig. 3.3. In addition, another intriguing observation was that the accumulated SS calcium increments, measured 2 second after the end of a pause, did not transmit beyond the proximal dendrites (Fig. 3.3.C).

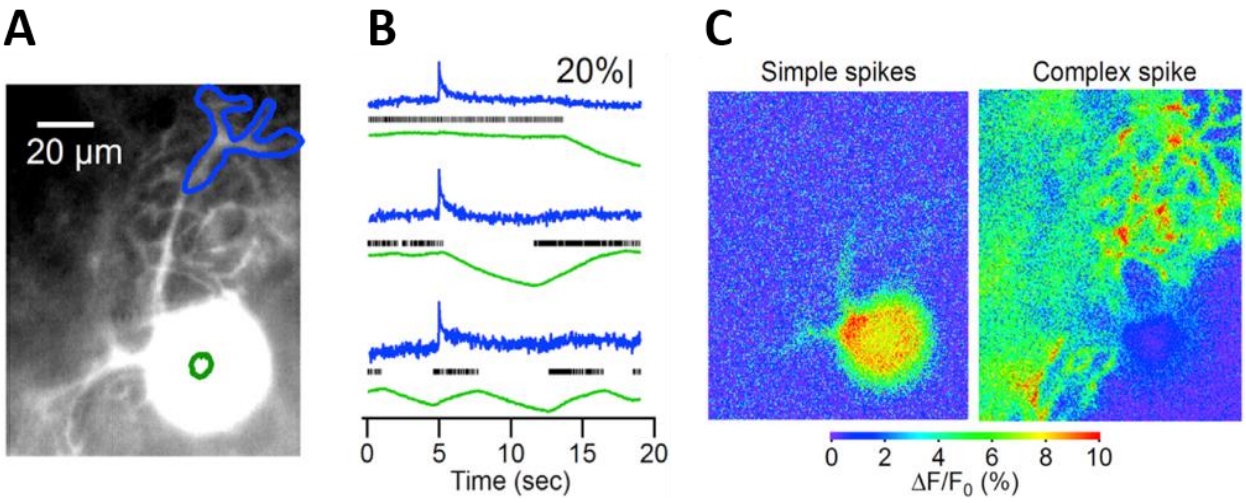

Figure 3.3. Comparison of Complex vs Simple Spike calcium signals in the Purkinje cell soma.

Note: **A.** Purkinje cell loaded with 100 µM OGB-1 via the patch pipette for 20 min. **B.** $\Delta F/F_0$ of fluorescence recorded from the two regions of interest shown in **A** (dendrites in blue and soma in green) and the corresponding raster plot of simple spikes recorded in cell-attached mode (black). Climbing fiber stimulation (at 5 s) produces a large increase in fluorescence in the dendrites that is not recorded in the soma. Scale bar, 20% $\Delta F/F_0$. **C.** Peak response of cell shown in **A** and **B** to simple or complex spikes. Images display the peak in the average $\Delta F/F_0$ of 14 repetitions for the simple spikes and 28 repetitions for the complex spikes. F_0 is the average for each pixel taken across the five frames just prior to either simple spike train or the complex spike. Same scale bar as in **A**. Each image is scaled to show minimum to maximum fluorescence from 0% to 10% $\Delta F/F_0$. Images taken from (Ramirez & Stell, 2016).

Considering that the CS contribution to the calcium influx in the soma is very small and that the frequency of these events *in vivo* is low (on average 1.5 Hz Gaffield et al., 2015), the

individual and summed effects of this calcium transients is unlikely to be detected. This implies that somatic calcium imaging can be used to monitor simple spike firing rate while dendritic imaging can be used to monitor complex spikes.

3.1.3. Coordination of activity between Purkinje cells mediated by GABA-A receptors.

Since somatic calcium reports the simple spike rate of Purkinje cells, we used it to investigate whether there is coordination of simple spike rate between Purkinje cells. From the anatomical organization of the cerebellum, it is known that Purkinje cells receive inhibitory inputs from interneurons on the same sagittal plane (Castejón, 2003). Thus, it is possible that sagittal Purkinje cells pause synchronously through common interneurons, and thereby relieve the DCN cells from their inhibition. We explored the coordination of Purkinje cells using both electrophysiology and calcium imaging experiments.

2.1.3.1. Coordination of simple spike pauses between sagittal Purkinje cells measured electrically

We performed electrophysiological experiments to characterize the pauses on Purkinje cells and their coordination as accurately as possible. To start, we evaluated the relationship between the spontaneous inhibitory signals reaching the Purkinje cells and their spontaneous spike pauses in the slices. To do so, we performed cell-attached recordings immediately followed by whole-cell voltage clamp in Purkinje cells to measure the spontaneous frequency of their spike pauses and compare them to the frequency of their inhibitory postsynaptic currents (IPSC). We found a high correlation (r-value = 0.867, n = 9 cells) between both measured frequencies as seen in Fig. 3.4.F. As the principal source of IPSCs in Purkinje cells comes from $GABA_A$ synapses, this result points to a role of the cerebellar GABAergic activity in the generation of spontaneous pauses in PCs.

Interneuron-to-Purkinje and Purkinje-to-Purkinje collateral synapses are the main inhibitory connections that contain postsynaptic $GABA_A$ receptors in the Purkinje cells (Orduz & Llano, 2007). Hence, to further examine the role of inhibition on Purkinje pauses, we blocked $GABA_A$ receptors by perfusing gabazine (SR-95531) while making cell-attached recordings from Purkinje cells in cerebellar slices. The occurrence of pauses was almost completely ceased in presence of 10 μM gabazine, as illustrated in the pair of Purkinje cells of Fig. 3.4.C. In average, this increased the mean instantaneous firing rate (IFR) from 13.2 ± 1.5 spikes/s in control versus 14.6 ± 2.0 spikes/s with gabazine ($p = 0.04$, paired Student's t-test; n = 18 cells), as previously

shown by (Häusser & Clark, 1997). However, very large pauses can have an oversized effect on the mean IFR and therefore underestimate the real average activity of the cells. Instead of the mean, we used another measure of the average firing rate, the median IFR, which is not affected by extreme data. The median IFR resulted in a decrease of the average activity from 18.6 ± 2.1 spikes/s in control versus 16.5 ± 1.9 spikes/s in gabazine ($p = 0.001$, paired Student's t-test; $n = 18$ cells). Interestingly, the two estimators reported opposite results for the effect of gabazine on spiking rate (as shown in Fig. 3.4.D), suggesting that there are two effects of blocking $GABA_A$ inhibition. On the one hand, gabazine occludes the IPSCs in Purkinje cells, therefore causing a decrease in their number of pauses as expected from the previous results (Fig. 3.4.F); which increments their mean IFR. On the other hand, gabazine also lead to a reduction of their median IFR by suppressing a mechanism that increases their average firing rate. This means that $GABA_A$ -R activity might have a tonic inhibitory effect in Purkinje cells that is abolished by gabazine. One possibility is that Purkinje cells that pause repeatedly have low intracellular [Ca^{2+}] that inactivate the hyperpolarizing effect from Ca^{2+}-activated K channels (BK type) present in the cell (Womack, Chevez, & Khodakhah, 2004), in turn inducing a higher firing frequency of spikes while the calcium slowly rises in the soma of the cell. However, with the pauses blocked by gabazine the [Ca^{2+}] stays high and the cell remains slightly more hyperpolarized by these channels, generating a decrease in the median IFR. Altogether, this results suggest that interneuron activity is strongly related to Purkinje cell pausing in slices.

Since Purkinje cell pause intervals are modulated by interneurons, and interneurons can connect to several PCs at the same time (Castejón, 2003), it is expected that Purkinje cells sharing the same connected interneurons could have coordinated firing activity. Moreover, interneurons can toggle Purkinje cells into their opposite state (Oldfield et al., 2010), firing or silent respectively, and therefore two PCs receiving the same interneuron input could have opposite reactions. Therefore, to test the coordination between PCs, we had to find a method to quantify this possible interaction and we started by defining a pause. From the previous results, we found the median IFR to be a robust measure of the average activity of Purkinje cells. For this reason, we employed its reciprocal (the median ISI) which corresponds to the average time the cell takes to fire an action potential. Then, we defined a pause interval as any given ISI that was longer than three times the median ISI. In other words, a pause occurred whenever the cell missed at least two consecutive (median ISI) spikes.

The criterion to identify pausing periods allowed us to identify when cells stopped or started a pause and therefore allowed us to detect synchronized transitions of firing activity between Purkinje cells. If the start or end of a pause on one cell coincided with the start or end of a pause in another (within the length of the shortest average ISI between both cells), then those transitions were considered simultaneous; as depicted in the inset of Fig. 3.4.D. This criteria not only identifies synchronous transitions when cells fire and pause at the same time, but also includes opposite toggling transitions between them (e.g. one cell pauses when another starts firing), as shown in some instances of Fig. 3.4.C. Finally, the two cells were considered to be synchronized or coordinated if the proportion of their simultaneous transitions compared to their asynchronous transitions surpassed the expected proportion attained by random coincidences (evaluated with a Monte Carlo permutation test; see section 2.4.3.).

This method to quantify the degree of coordination between PC transitions was used on simultaneous cell-attached recordings from 59 sagittal pairs of neighboring PCs at different soma-to-soma distances. Sagittal Purkinje cells close to each other were more likely synchronized than distant ones, up to 200 µm. After that distance, the coordination is lost (Fig. 3.4.B). Strikingly, this spatial extent of the synchronization matches with the average length of the interneuron axons in the sagittal plane (211.7 ± 54.9 µm, (Zorrilla de San Martin, Jalil, & Trigo, 2015), hinting that interneurons are a source of coordination of Purkinje cell transitions in slices.

2.1.3.2. Coordination of somatic calcium signals in groups of Purkinje cells

After observing local synchronicity between sagittal Purkinje cells with electrophysiology, the next step was to use the calcium imaging approach to better evaluate the spatial extent of coordination between Purkinje cells. Unlike with the electrophysiology, the imaging approach allowed us to monitor cells that were at different sagittal planes in transverse slices. For this purpose, several Purkinje cells in both transverse and sagittal cerebellar slices were loaded with OGB1 using a patch-pipette and their fluorescent calcium signals were recorded with epifluorescence, as the example seen in Figure 3.4.A.

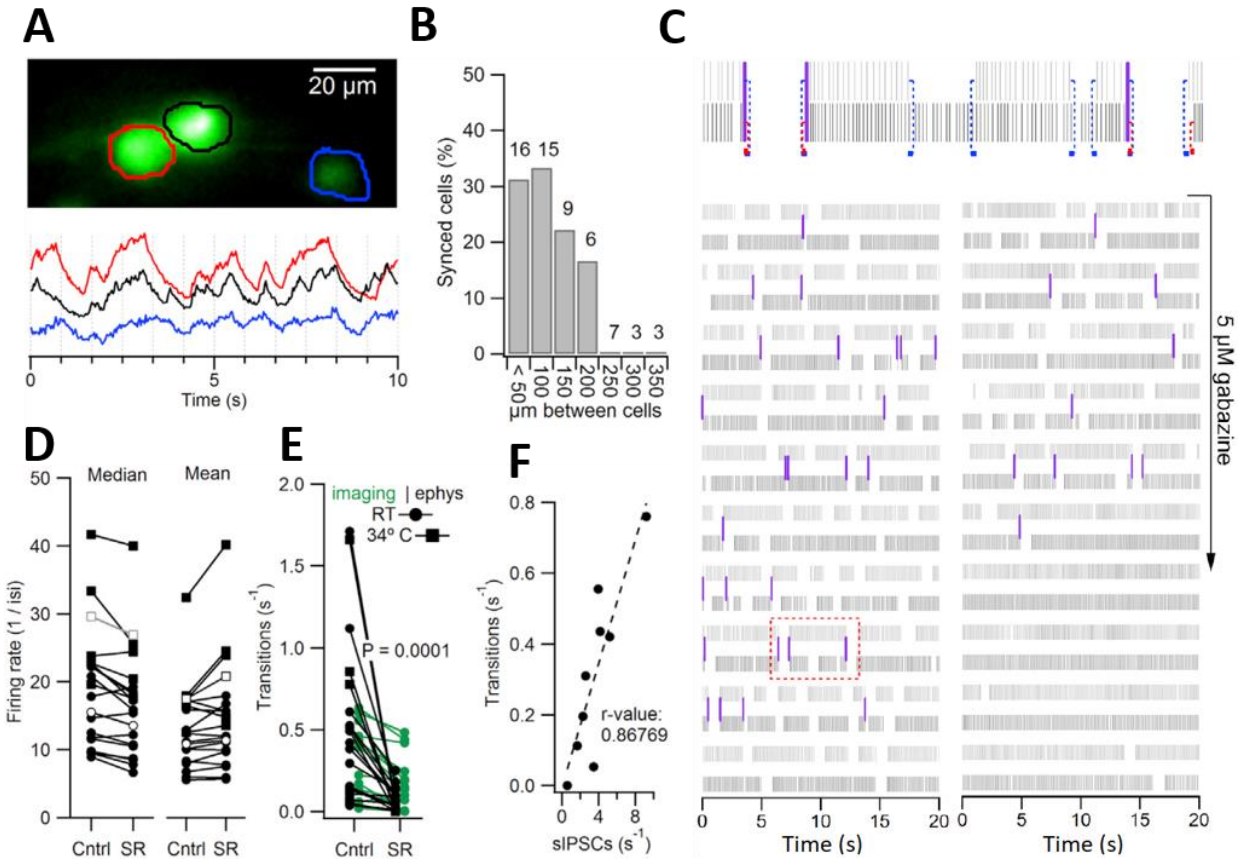

Figure 3.4. $GABA_A$ receptors correlate activity between direct Purkinje cell neighbors in the same sagittal plane.

Note: **A.** Three Purkinje cell somas in roughly the same sagittal plane of a transverse slice (Purkinje cell dendrites descending into the plane of the slice) individually preloaded with 100 mM OGB-1 for ~ 5 min each. Lower panel plots $\Delta F/F_0$ from the ROIs drawn on the upper image. **B.** Percentage of pairs of cells recorded in cell-attached mode that show significant synchrony in transitions into and out of pauses (lasting longer than three times their median firing frequency) as a function of distance between somas. The number of pairs recorded at each distance is indicated above each bar. **C.** Raster plot of simple spikes detected in two Purkinje cells (each cell in different shades of gray) with loose cell-attached recordings from two neighboring Purkinje cells (represented in different shades of gray). The upper panel illustrates an expanded section of the lower raster (shown in red dashed box) and demonstrates how simultaneous transitions between pauses were detected: one median inter-spike interval is indicated with a dashed line in blue or red at the beginning and end of a pause (any inter-spike interval more than three times the median) that indicates a simultaneous transition when overlapping (purple bars). Gabazine is washed into the recording chamber where indicated and clearly decreases the frequency of simultaneous transitions. **D.** Firing rate (median and mean) recorded with cell-attached electrodes in control conditions and after washing 5 mM gabazine into the bath. As in **E**, boxes represent recordings made at 34°C and circles represent recordings made at room temperature; open symbols represent the averages for each condition. **E.** Rate of transitions to and from pauses in control conditions and in the presence of 5 mM gabazine. Gabazine significantly reduced the frequency of transitions ($p = 0.0001$). Electrophysiology data shown in black and imaging data shown in green were not significantly different ($p > 0.05$). **F.** Transitions to and from pauses lasting longer than three times the median inter-spike interval recorded in loose cell-attached recordings plotted versus spontaneous IPSC frequency recorded in subsequent whole-cell recordings from the same cells ($n = 9$ cells). Images taken from Ramirez & Stell, 2016.

In this case, the synchronicity between cells was revealed with a different method, designed from the previous finding that the second derivative of the smoothed somatic calcium traces contains information of their firing frequency transitions. First, we quantified the coordination between calcium traces with the Pearson's correlation coefficient (r) using the absolute values of their second derivative. Then, we calculated this r-value between all the combination of traces from the cells and classified the correlations into two groups: the simultaneous and the asynchronous pairs. To test if there was a coordination above random chances of synchrony, the r-values for correlations between synchronously recorded calcium traces were compared to the r-values of asynchronously recorded calcium traces with an unpaired Student's t test (one-sided). When the r-values from correlations performed between synchronously recorded calcium traces were bigger than the r-values for asynchronous correlations (below $\alpha = 0.05$ error rate) the cell's transitions were considered to be synchronized or coordinated. A diagram illustrating this analysis is shown on the Data Analysis section.

The results derived from these experiments showed that pairs of Purkinje cells localized to the same sagittal plane were synchronized ($p < 0.05$, $n = 10$ pairs), while pairs between transverse planes were not ($p > 0.05$, $n = 5$ pairs). If we combine these results with the previous electrophysiological approaches, they suggest that the transitions of Purkinje cells on cerebellar slices are mainly synchronized by the spontaneous activity of interneurons, as these cells only project inhibitory connections to other cells localized on their same sagittal plane (Castejón, 2003).

3.2. Somatic calcium imaging as reporter of simple spike firing *in vivo*

Taken together, the previous results from slices demonstrate that somatic calcium imaging can be used to follow changes in the SS firing rate of Purkinje cells. However, an enormous potential for cerebellar research could be unlocked if this method is successfully combined with 2-photon microscopy, which would allow the study of the cerebellar cortex output *in vivo*. First of all, the Purkinje cell soma is located deep below the molecular layer, the cerebellar region where the cells receive inputs, so this non-invasive imaging method could keep the cell inputs unharmed while recording the somatic output (unlike the intrusion required for electrical recordings). Second, this method could be used to record tens or hundreds of spatially identified Purkinje cell somas simultaneously, a mandatory data acquisition requirement since Purkinje cell coordination is the

essential feature that modulates the output of DCN cells (Gauck & Jaeger, 2000; Person & Raman, 2011). Third, this imaging method could enable both behavioral and longitudinal studies on the cerebellum output, for instance, by relating the Purkinje soma activity patterns with a corresponding animal action or learning task through several recording sessions. Overall, this imaging method could open avenues for more integrative experiments to elucidate the fine-tuning of cerebellar function.

To begin testing this approach *in vivo*, we decided to use the genetically encoded calcium indicator (GECI) GCaMP6f instead of the OGB1 we used in slices because of the several advantages of the GCaMP6f system.

To verify if the calcium fluctuations seen in slices could also be recorded *in vivo*, PV-Cre or L7-Cre transgenic mice were injected with a GCaMP6f adenoviral construct and left 3-4 weeks until optimal expression of the indicator was achieved in Purkinje cells. On the day of an experiment, the animals with the viral GCaMP6f expression were anesthetized with ketamine and xylazine and their cerebellum was visualized through 2-photon microscopy as described in detail on the Methodology section. Two different experiments were carried out on the Purkinje cells of these animals: (1) simultaneous cell-attached voltage clamp with somatic calcium imaging recordings, and (2) recordings of spontaneous calcium signals.

3.2.1. Action potential frequency reported by somatic calcium imaging in Purkinje cells

Using electrophysiology, many labs have reported spontaneous firing of Purkinje cells with pauses in firing in both awake and anesthetized preparations (Cao, Liu, Jaeger, & Heck, 2017; S. Chen, Augustine, & Chadderton, 2016; Ramakrishnan et al., 2016; Zhou, Voges, Lin, Ju, & Schonewille, 2015). We wanted to determine if this firing could be reported with the calcium indicator approach. Analogously to the slice experiments, recordings from simultaneous cell-attached patch clamp and calcium imaging of Purkinje cells were obtained *in vivo*. This data could confirm if the simple spike rate can be followed with the somatic calcium fluctuation as seen before. However, it is worth mentioning that the technical difficulty of the *in vivo* procedures was much greater than in slices, resulting in a lower number of successful experiments. Nevertheless, we recorded from 3 cells (Fig. 3.5.) that served as a proof of concept to examine this potential estimation of firing frequency from the *in vivo* somatic calcium imaging.

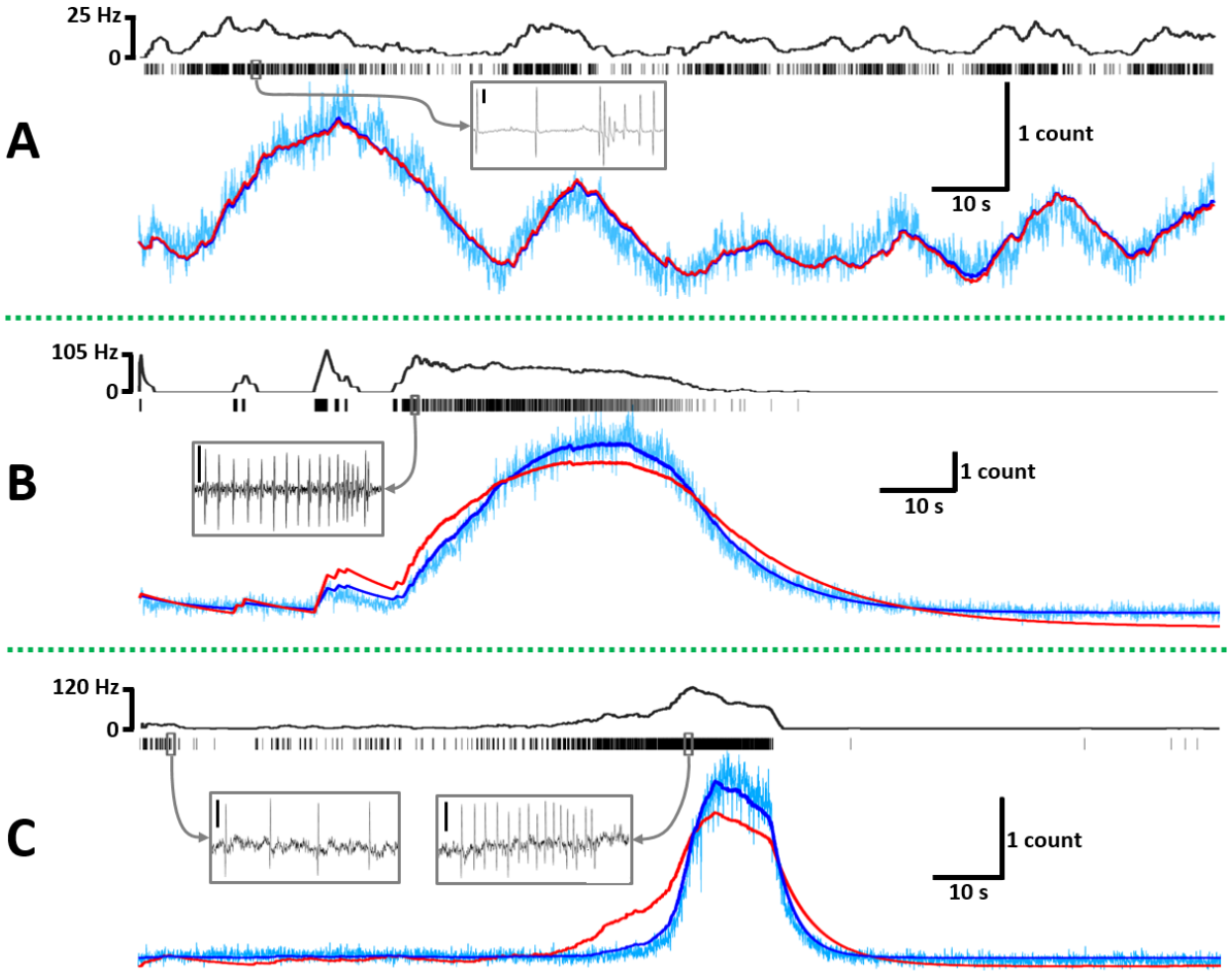

Figure 3.5. Simultaneous recordings of *in vivo* cell-attached patch clamp and GCaMP6f calcium imaging in Purkinje cell somas.

Note: **A.** Recorded cell from Ramirez & Stell, 2016. **B, C.** Other recorded cells. In top of each section lies the time-averaged SS firing rate with a sliding window of 2 seconds. Below it, each spike event is shown in a raster plot. *Cyan traces:* raw fluorescence signal. *Red traces:* linear convolution of spike events and optimized kernel (same method from slice experiments). *Dark blue traces:* Theta transformed convolution. *Insets:* sample segments of 100 ms from the cell-attached recording in each cell. The black bar inside all insets represents 20 pA.

In two of the three cells shown in Fig. 3.5., there is a marked lack of activity for very long periods of time; a finding that contradicts previous results (Schonewille et al., 2006) in ketamine/xylazine anesthetized mice. In fact, the pattern of firing activity with long silent periods resembles much more the ones reported for anesthetized guinea and rat Purkinje cells (Loewenstein et al., 2005).

Nevertheless, in these simultaneous electrophysiology and imaging experiments we can see a clear correlation between the simple spike activity and the somatic calcium imaging. However, owing to the switch of calcium indicators from OGB1 to GCaMP6f, the analytical procedure used to verify the linear relationship between the firing rate and the fluorescence traces in slices was no longer valid for all cases *in vivo*. It was an expected problem, since the non-linear calcium kinetics of GCaMP6f distort the fluorescence fluctuations when the Purkinje cell has a low or high intracellular calcium concentration (see Fig. 2.9.). There are several published methods found in recent literature that were designed to resolve part of this problem in other biological models using GCaMP6f (Theis et al., 2016). However, they require that each fired spike generates a fluorescence transient with reasonable signal-to-noise ratio, which is not our case. Also, none of them consider the nonlinear behavior at low calcium concentrations. Fortunately, the origin of these specialized methods traces back to more general solutions coming from signal transmission and restoring problems (i.e. Weiner filters, Henry Lütcke and Fritjof Helmchen, 2011). Starting from this basis, we developed an analysis more suited to describe our model by using a blind deconvolution (see section 2.4.5. for more details).

In practical terms, the only difference between the previous linear convolutional model used in slice recordings and the nonlinear model presented here is the inclusion of θ_{trans}, which modulates the amplitude of the calcium changes depending on the fluorescence level. This additional transformation was added to the previous fitting routines, and the results of both the new and old fitting models are compared with the *in vivo* recordings in Fig. 3.5. (see improved fit with θ_{trans} in blue and classic convolution in red).

The fitting results from the three cells recorded *in vivo* (illustrated in Fig. 3.5. and summarized in Table 3.1.) demonstrate the nonlinear effects caused by the GCaMP6f, and the efficacy of the θ_{trans} model to compensate for them. In the first cell (Fig. 3.5.A), both the nonlinear and linear models fit well the fluorescence data as a result of a firing activity that doesn't have long pauses, which kept the intracellular calcium concentration around the linear range of GCaMP6f. For the second cell (Fig. 3.5.B), the nonlinear model outperforms the linear model, with the latter overestimating the signal at low fluorescence levels and underestimating it at higher levels as is expected from the GCaMP6f Hill model (see Data Analysis for details). And lastly, the third cell (Fig. 3.5.C) shows the case when very low firing activity is impossible to discern from

the noise, concealing the onset of an slow increment in firing rate by the nonlinearity of the GCaMP6f indicator.

In general, the nonlinear model had a better fit than the linear model, denoted by its lower sum-of-squares values in the difference between real and modeled traces (columns SSQ in Table 3.1.). However, the variability of the parameter values between cells is very high, for instance, the kernel decays are similar between cell A and B but lower in C, and the kernel amplitude was similar in B and C but higher in A. More data is needed to know the extent of this cell variability, which could encumber the ability to approximate the firing activity of cells using only its Ca^{2+} imaging recordings.

Table 3.1. Estimated parameters of the fitted models from the simultaneous cell-attached and calcium imaging recordings of *in vivo* Purkinje cells.

	Nonlinear model with θ_{trans}					Linear model			
Cell ID	**Kernel decay (τ)**	**Amplitude (count)**	**F_{MIN} (count)**	**F_{MAX} (count)**	**SSQ**	**Kernel decay (τ)**	**Amplitude (count)**	**F_{MIN} (count)**	**SSQ**
A (6 traces)	8.83 ± 1.76 s	0.0371 ± 0.0089	1.51 ± 0.36	43.22 ± 6.27	30.25 ± 9.51	10.01 ± 6.53 s	0.0149 ± 0.0040	1.77 ± 0.74	171.2 ± 112.8
B (9 traces)	7.62 ± 1.92 s	0.0088 ± 0.0027	0.65 ± 0.06	49.74 ± 10.28	39.94 ± 18.42	14.18 ± 6.16 s	0.0033 ± 0.0016	0.41 ± 0.26	274.8 ± 235.8
C (3 traces)	2.77 ± 0.38 s	0.0113 ± 0.0047	0.25 ± 0.09	49.75 ± 12.97	4.51 ± 4.97	4.49 ± 1.62 s	0.0029 ± 0.0008	0.20 ± 0.04	81.26 ± 101.6

Note: Rows A, B and C correspond to the cells in Fig. 3.5. (same nomenclature). In each entry of the table, the mean parameter value is located at the top and its standard deviation at the bottom. SSQ stands for the final sum of the squared difference between the model and the real fluorescent recording obtained from the blind deconvolution optimization.

3.2.2. Somatic vs dendritic calcium signals from complex spikes in anesthetized mice

Previous studies have focused on imaging complex spikes *in vivo* (Gaffield et al., 2015; Kitamura & Häusser, 2011; Najafi et al., 2014a) presumably because of the large fluorescent signal they produce in the dendrites of Purkinje cells. However, our results above indicated that fluorescent signals produced by complex spikes are excluded from the somas in the cerebellar slice

preparation. To determine if this is also the case *in vivo* we imaged spontaneous spiking from Purkinje cells in anesthetized mice. In some trials with the anesthetized animals, it was possible to see lateral regions of the cerebellum where fluorescent Purkinje cells were sparse or separated and had a tilted orientation, with part of their dendrites and somas in the same imaging plane. We used these cases to simultaneously image the soma and dendrites of Purkinje cells to compare the spontaneous signals in each compartment; an experiment analogous to the one in cerebellar slices using the controlled activation of climbing fibers as seen in Fig. 3.3. An example is shown in Fig. 3.6.(A-C). The dendritic Ca^{2+} transients shown in the example have kinetics that are consistent with those reported for complex spikes (Gaffield et al., 2015).

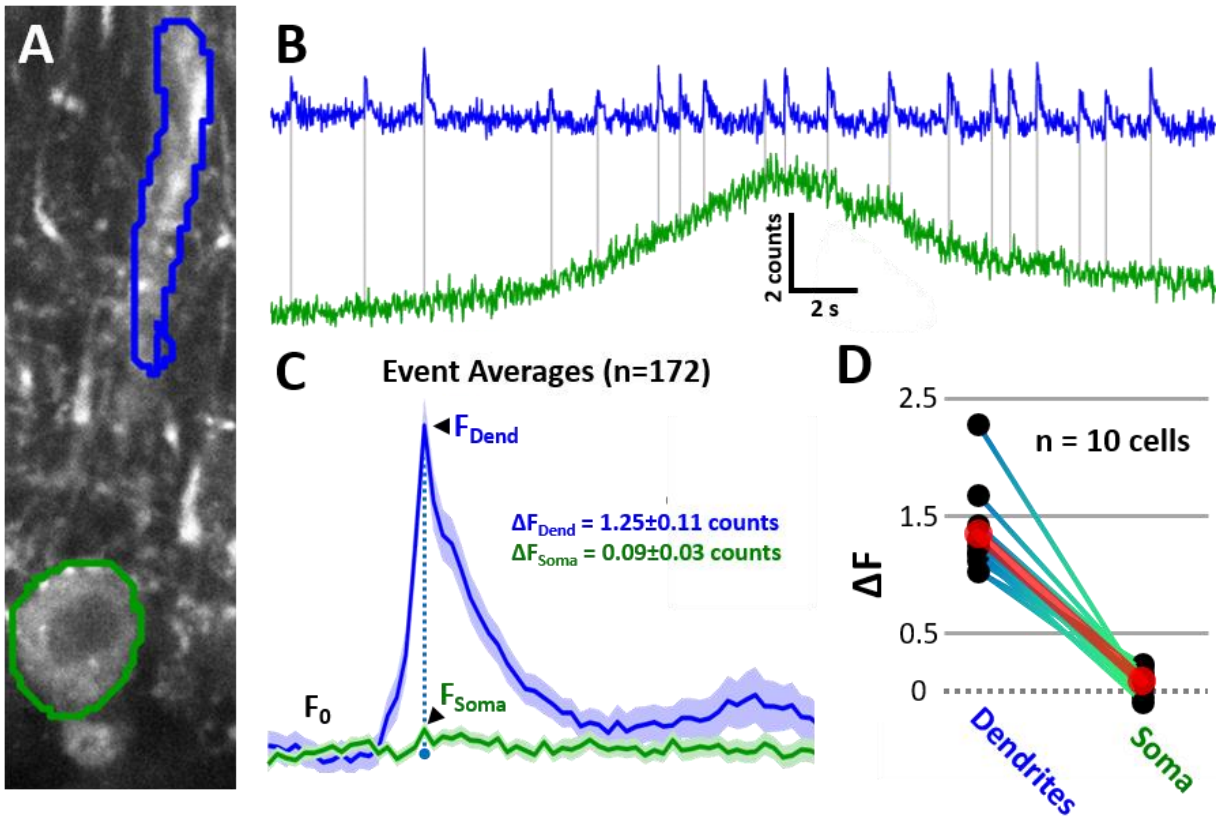

Figure 3.6. Somatic vs. Dendritic Ca^{2+} images with GCaMP6f in anesthetized animals.

Note: **A.** Average 2-photon image in a PV-Cre animal expressing GCaMP6f with a Purkinje cell oriented laterally with its soma (green ROI) and portion of its dendrites (blue ROI) in the same optical plane. **B.** Fluorescence signal from each drawn region showing spontaneous dendritic activity and somatic fluctuations. **C.** Average signals of all the detected events in the dendrites and in their corresponding somatic time windows. In this cell, 172 events with more than 1 count of amplitude were selected for the average and the others were discarded. **D.** Compiled results of the average events from 10 tilted Purkinje cells. The red line corresponds to the average values of the 10 cells, with a dendritic and somatic signal of 1.35±0.38 and 0.08±0.10 counts respectively.

In slices, the events were triggered by electrical stimulation of the climbing fiber so their extraction was trivial, but in our *in vivo* recordings we had to detect such events. For this reason, the slope threshold algorithm was employed with sensibility for fast changes using a threshold of a Z-score = 2.6 for the noise and 200 ms for the threshold duration (see Data Analysis). Because there was variability in the size of the dendritic transients (as described by Kitamura & Häusser, 2011), an additional selective criterion was used to only consider those events with at least 1 count of amplitude, thus extracting the biggest changes that could had a noticeable effect. The results obtained from this method turned out similar to those in slices, with almost a 20-fold difference between the dendritic and somatic calcium transients (Fig. 3.6.D). These results confirm that somatic simple spike calcium signals *in vivo* are isolated from the confounding calcium transients coming from the complex spike signaling.

3.2.3. Spontaneous calcium signals in populations of Purkinje cell somas

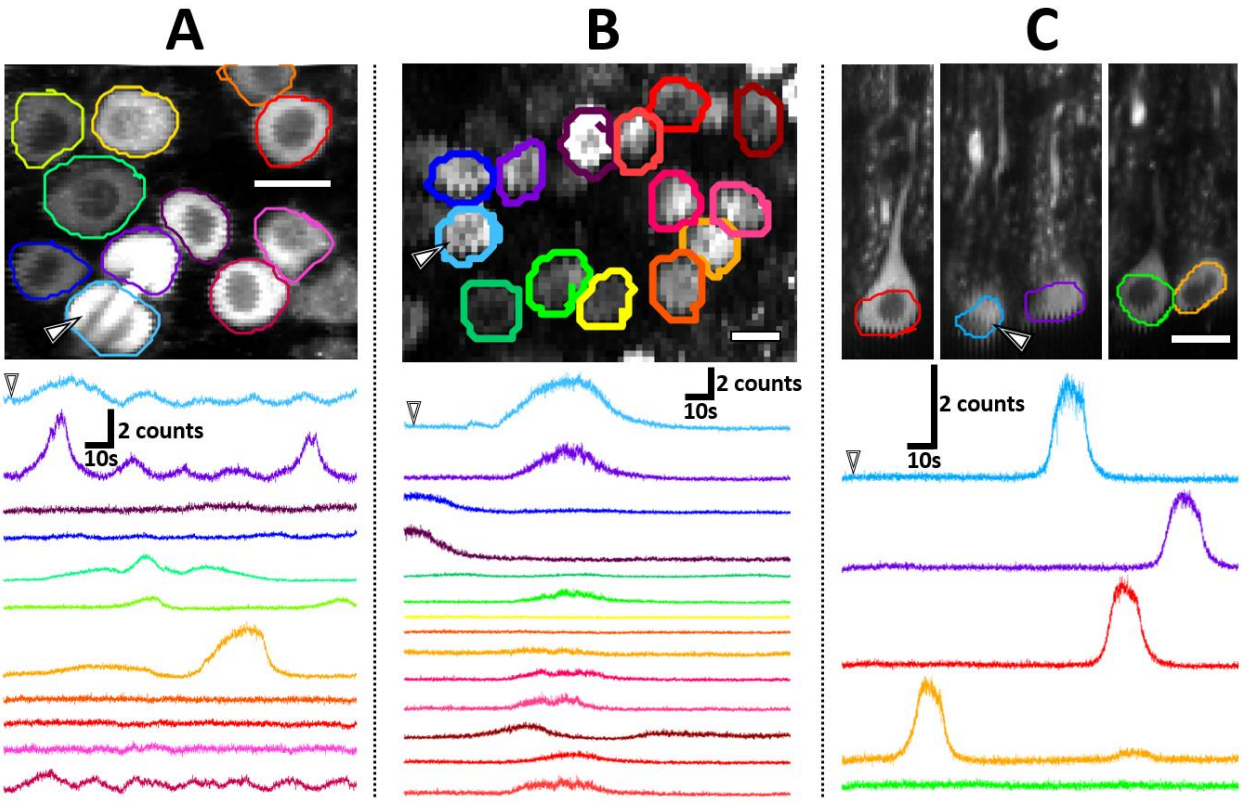

Figure 3.7. Two-photon calcium imaging of cerebellar Purkinje cell somas expressing viral GCaMP6f in anesthetized mice.

Note: **A.** Purkinje somas in the most dorsal portion of lobule V from a PV-Cre transgenic mouse with 22 days of expression. **B.** Purkinje somas in the most dorsal portion of lobule V from an L7-Cre transgenic

mouse with 38 days of expression. **C.** Purkinje cell somas at different depths on a side of lobule V from a L7-Cre transgenic mouse with 23 days of expression. All recordings were made at a laser wavelength of 910 nm from mice anesthetized with ketamine/xylazine. The white triangles marks are pointing to the cells that had accompanying cell-attached recordings (same traces of Fig. 3.5.). Scale bar on the images correspond to 20 µm.

The spontaneous calcium activity recorded from the somas of Purkinje cells in the anesthetized *in vivo* preparation, unlike the somas in slice experiments, generally presented constant fluorescence without trends or deviations. Sometimes, somatic signals had few fluctuations with very slow time courses and with enough amplitudes to stand out of the signal noise (Fig. 3.7., Appendix). Under these circumstances, the differentiation algorithm that was employed to detect transitions in slice experiments was not reliable because the change events were not abrupt enough to be revealed by the second derivative. Instead, a custom method to replace the previous one was designed, envelope thresholding (see Data Analysis), which could detect slope changes from these noisy time series (Fig. 3.8.). This new heuristic algorithm was used to recognize change events throughout 656 Purkinje cell somas from 24 anesthetized animals that had spontaneous *in vivo* imaging. A selection of the traces showing the most prominent fluctuations in each imaged region, including their detected change-points, are shown in Appendix.

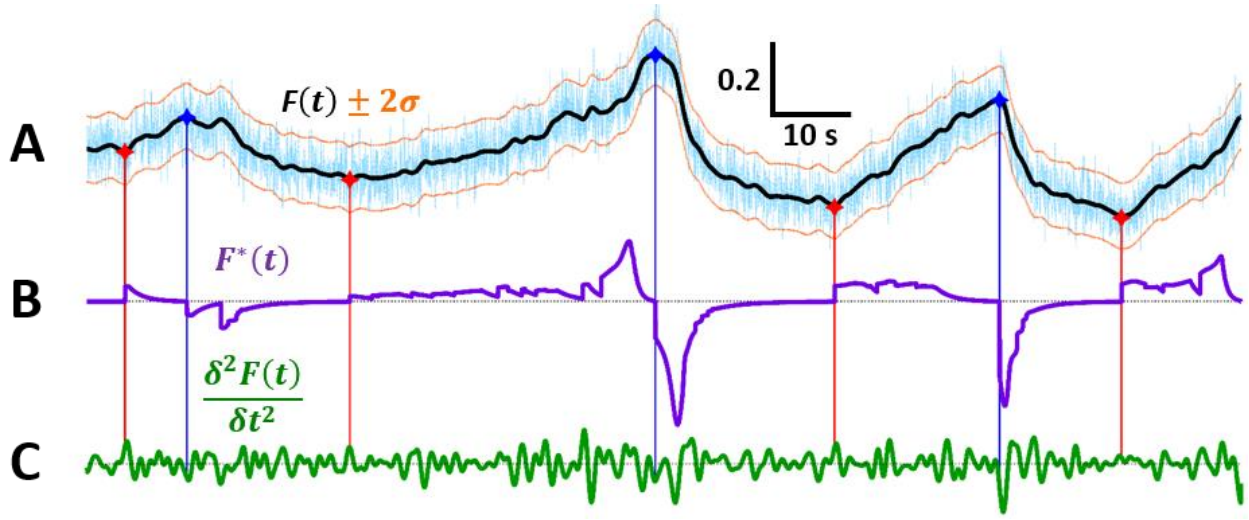

Figure 3.8. Example of the slope thresholding algorithm in action.

Note: **A.** Raw fluorescence data collected from a Purkinje soma (blue trace). The trace was denoised with binomial smoothing using a 20 second window in 1 pass ($F(t)$; black trace) and the noise residuals were used to estimate gaussian confidence intervals with Z-score = 2 (orange traces). The detected slope changes are shown as red points for increments and blue points for decreases. Vertical scale bar unit is in average photon counts. **B.** Transformed time series ($F^*(t)$) calculated with the slope threshold algorithm (T_{thres} = 120 s) showing features associated with the observable fluctuations. **C.** Second derivative of the denoised trace ($\delta^2 F(t)/ \delta t^2$) with no clear features visibly related to the minimums and maximums (slope changes) detected with the algorithm.

The pooled histograms of frequency and signal-to-noise ratios of the fluctuations from all recordings is shown on Fig. 3.9. One third of the cells (224 out of 656) didn't have any detectable deviation above the estimated noise from its fluorescence recordings. Overall, the total median frequency of detected changes was of 3.6 mHz (around 1 transition per 5 minutes of recording), and their median amplitude was only 1.58 times bigger than the estimated noise. These few and small-amplitude fluctuations recorded from Purkinje cells somas, which are the point of integration of the multiplicity of inputs converging to the cell, might be reflecting a low or tonic spike firing rate arising from reduced cerebellar cortex activity. This is most likely caused by the neuro-depressing effects of the ketamine/xylazine anesthesia in rodents. For instance, ketamine and xylazine are known to greatly reduce both parallel and climbing fiber discharges *in vivo* (Bengtsson & Jörntell, 2007), with ketamine having a direct inhibition of granule cells through the activation of specific $GABA_A$ receptors (Hevers, Hadley, Lüddens, & Amin, 2008). Furthermore, ketamine appears to reduce the firing activity in subpopulations of Purkinje cells located in lobules V and VI (Aida, Fujiwara, & Shimoji, 1994; Schonewille et al., 2006) . However, the degree of the inhibitory effect from ketamine/xylazine seems to be highly variable across PCs and also in different regions in the cerebellum, as other researchers have found smaller effects of ketamine in lateral lobules like the Crus II (Schonewille et al., 2006), or higher effects causing low firing rates in PCs on lobule VIII (Xiao et al., 2014).

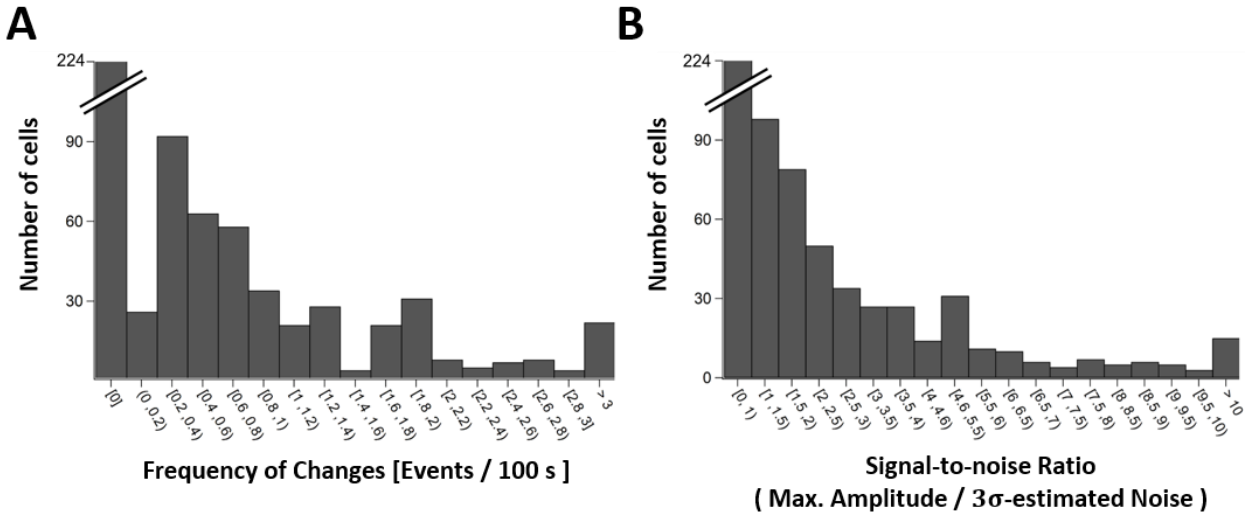

Figure 3.9. Assessment of the average spontaneous activity in Purkinje cells on anesthetized animals.

Note: **A.** Histogram showing the frequency of change events found with the slope threshold method in all the traces collected from Purkinje somas. **B.** Histogram showing the maximal amplitude of the events in the cells compared to the estimated noise amplitude used for the slope threshold algorithm (Z-score ~ 3.1; see the Appendix for more details on the estimation). The total number of cells is 656 from 24 anesthetized animals.

Not only the *in vivo* fluctuations of the fluorescence signal were less frequent and seemingly smaller than in slices, but also they lasted longer and had less sharp transitions. In the slices, the crisp kinks in the calcium signals came from abrupt changes in SS firing activity on the cells, which implies that the slow *in vivo* deviations might be produced by more gradual spiking rate changes. Moreover, a third of the cells recorded *in vivo* were not fluctuating at all, which could be the consequence of stable firing rates or completely inactive cells. In any case, to corroborate the link between the fluorescent signal and the spiking behavior of the cells expected from the slice experiments, we performed a new round of simultaneous electrophysiological and imaging recordings *in vivo*. Fortunately, the widespread expression of the calcium indicator allowed us to search for lobule regions with Purkinje cells that had more activity than the average, in order to have contrast in the fluorescence fluctuations to relate with the spike timings as done previously in slices.

3.3. Preliminary results of somatic calcium activity in behaving mice

Although extracting information from spontaneous Ca^{2+} fluctuations proved to be difficult due to noise recorded during experiments with anesthetized animals, we thought that if we could sync the experiment to a stereotypical behavior in awake animals we could average our analysis and increase the signal-to-noise ratio. To accomplish this, we implemented a behavioral paradigm using a running wheel that allowed us to simultaneously monitor the locomotion of the animal and the Purkinje cell activity using 2-Photon imaging on the cerebellar vermis. (Ozden et al., 2012) showed that the running behavior in mice was tightly correlated with changes in activity of granule cells, interneurons, and Purkinje dendrites on the cerebellar lobules V-VI. With the use of Ca^{2+} indicators, they saw that locomotion caused a direct increment of the Ca^{2+} signals from these 3 cerebellar elements. Accordingly, these results suggest that the Purkinje cell output on this region might also change with locomotion, which should correspond to Ca^{2+} fluctuations on their somas as well.

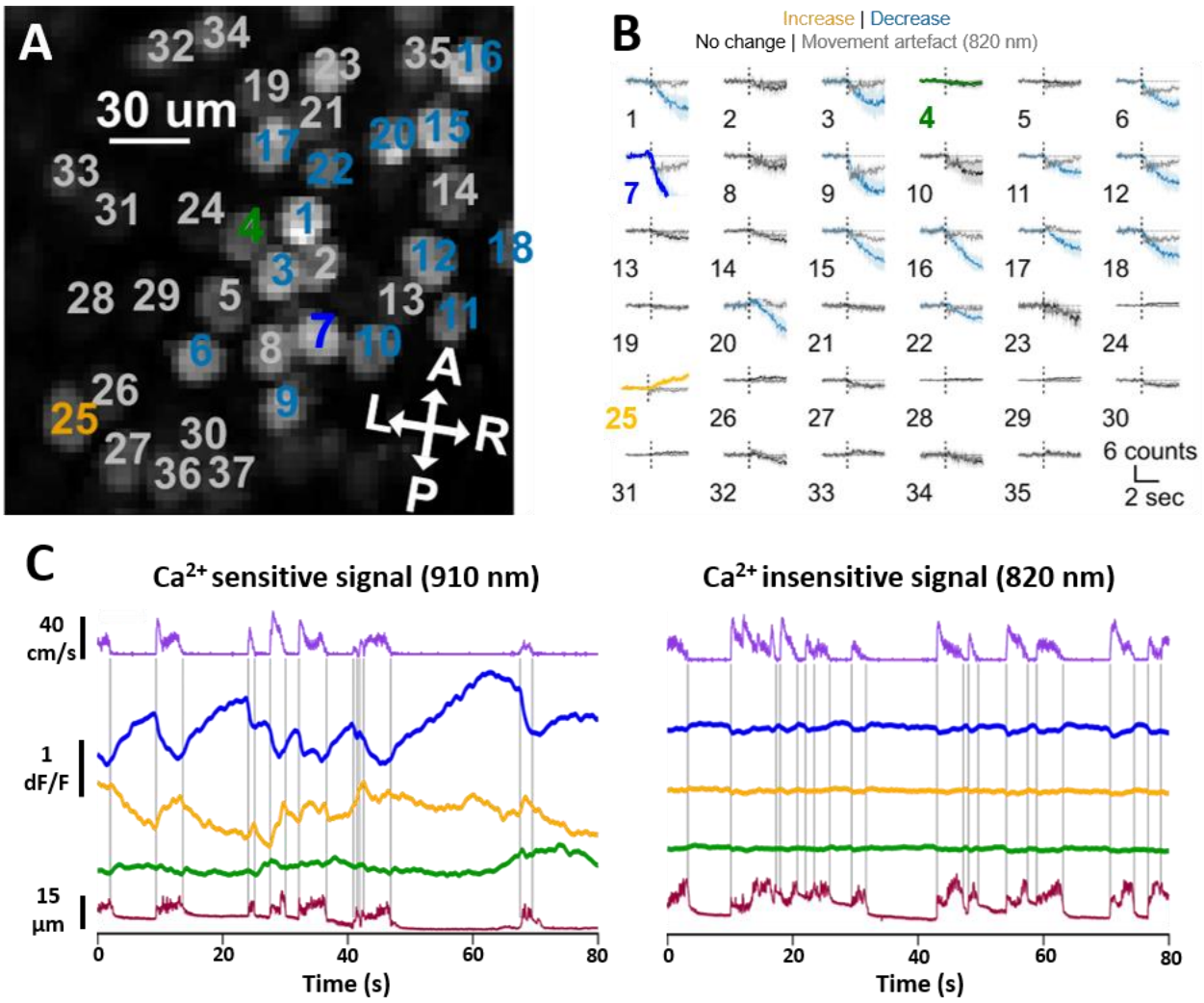

Figure 3.10. Running wheel experiments with 2-photon calcium imaging of an L7-Cre mouse with GCaMP6f expression in cerebellar Purkinje cells.

Note: **A.** Average imaging field of Purkinje cell somas recorded from lobule V of the cerebellar vermis. The cross at the bottom shows the anterior/posterior and left/right directions of the animal extracted from the PC dendrite orientation (data not shown). **B.** Average fluorescence traces in a 5 second time window of the ROIs identified in **A** from all the events where the animal started a locomotion. Traces and ROIs with a color different than gray have changes significantly different than the estimated movement artifacts reported by the Ca^{2+} insensitive fluorescence at 820 nm (judged by the overlap of the shaded confidence intervals with 1.96×SEM). **C.** Examples of dF/F traces at 910 and 820 nm excitation showing the correlation between 3 representative ROI signals and the locomotion of the animal. *Purple line*: Linear speed of the mouse in the running wheel obtained from a rotary encoder. *Blue, orange, green lines*: Fluorescence traces showing inverse, congruent and uncorrelated responses upon start of locomotion of the animal from the ROIs 7 (blue), 25 (orange) and 4 (green) respectively. *Dark red line*: Total XY displacements from movement artifacts affecting the recordings that were compensated by the image registration procedures. *Gray vertical lines*: Epochs of onset or end of running events.

To reproduce this experiment, we started by implanting chronic windows (CW) with stainless steel head restraints on several L7-Cre mice transfected with the GCaMP6f adenovirus used in our previous procedures. This allowed us to visualize the activity of cerebellar Purkinje cells using our 2-photon microscope while the animal was held in a running wheel with its head immobilized. However, the movement artifacts caused by the animal's locomotion tampered the imaging quality, with a partial improvement after image registration was applied to the data. To control these confounding artifacts, we recorded additional images using the Ca^{2+}-insensitive 2-photon excitation wavelength of GCaMP6f at 820 nm, which let us estimate the effect that the artifacts could generate on the Ca^{2+}-sensitive signals at 910 nm (for details, see Fig. 2.5.). The locomotion of the animals was recorded using a rotary encoder attached to the axis of the running wheel. Following the guidelines from (Ozden et al., 2012), the animals were persuaded to run by using an air-puff to the back of their bodies.

Only one animal from the batch we processed had sufficiently low noise artifacts that allowed a clear extraction of the Ca^{2+} sensitive fluorescence signals, which are presented in Fig. 3.10. As expected from the (Ozden et al., 2012). results, the firing activity of Purkinje cells (monitored by their somatic calcium signals) was coordinated with the running events on the animal as the other cell elements in this cerebellar region. Remarkably, three different response patterns of Purkinje cell were seen: (1) inverted responses with a conspicuous decrease in firing activity on locomotion, (2) congruent responses having an increment on activity, and (3) uncorrelated responses with fluctuations not visibly related to the running events. From Fig. 3.10.B, it is clear that the uncorrelated cells were the most abundant (62% of cells), followed by the inverted-type cells (35% of cells) and lastly, the rarely seen congruent-type cells (3% of cells). Although the Purkinje cells with the inverted response were spatially aggregated (Fig. 3.10.A), there was no obvious relation with the sagittal direction as would have been expected from interneuron-mediated coordination. However, more data and bigger imaging fields would be required to fully test this hypothesis.

4. DISCUSSION

To understand how the cerebellum works, we need to study the emergent properties of the cellular machineries that compose it. Interestingly, the essential features of these machineries are present in many neuronal structures across the evolutionary tree of the vertebrate subphylum. The research done over these cerebellar-like circuits suggested that the function emerging from these assemblies solves a common problem: the identification of relevant information against the background introduced by external and self-generated trends (Sawtell, 2017). From this evolutionary history, it is currently acknowledged that a high amount of information has to be integrated within these circuits to achieve: (1) the compilation of an internal modeled version of the sensorial "footprint" of such trends (the negative image), and (2) the subtraction of these negative images from the real sensory signals to enhance the relevant features (the adaptive filter). Inside the mammalian cerebellum, both functions are joined together by the Purkinje cells which collect all signals form parallel and climbing fibers, and project an inhibitory (hence subtracting) signal to their principal cells in the deep cerebellar nuclei (Bell et al., 2008). Considering their role, in this thesis we focused on developing a method to monitor Purkinje cell activity *in vivo*, in a way that preserves their integrity while acquiring most of the information encoded in both their location inside the cerebellum and in their firing activity.

In this thesis, we demonstrated for the first time that somatic calcium imaging can be used to follow changes of simple spike firing activity in Purkinje cells and we set those signals apart from complex spike signals. Both inputs are known to modulate the function of Purkinje cells, with complex spikes acting as a teaching/training signal and simple spikes as carriers of the output of the cerebellar cortex (Dean et al., 2009). Thanks to this imaging method, it is now possible to acquire simultaneously both input signals while the animal is performing a cerebellar-dependent behavior, thus opening many new avenues on the cerebellar research field.

4.1. Detectability of firing activity changes in Purkinje cells using somatic calcium imaging

For our Ca^{2+} imaging method to work, we exploited two different factors: (1) the intrinsic relationship between the increases in somatic calcium with depolarization of Purkinje cells, and

(2) the high Ca^{2+} buffering capacity of the Purkinje cell somas. The first relationship was established long ago from the in vitro electrophysiological characterization of Purkinje cells made by (Llinás & Sugimori, 1980b). When they removed the free extracellular Na^{+} from the cells, they isolated a calcium current generated by depolarization in the soma. The origin of this Ca^{2+} current was further studied, and it was attributed to the activation of P-type voltage-dependent Ca^{2+} channels (Usowicz, Sugimori, Cherksey, & Llinás, 1992).

The second factor that influenced our measurement of the somatic Ca^{2+} signals in the Purkinje cells is their highly capable Ca^{2+} buffering system. These cells contain a high concentration of calcium buffers such as calbindin, calmodulin, and parvalbumin (Bastianelli, 2003) that confers them a very high Ca^{2+} binding ratio around 2000 (in rats; Fierro & Llano, 1996), an order of magnitude higher than other cell types in the nervous system. This buffering system allowed us to use relatively high concentrations of Ca^{2+} indicators inside the cells, as their additional buffering capacity would unlikely alter the Ca^{2+} homeostasis of the cell. In turn, the high concentration of the fluorophore ensured more brightness of the imaging signals, increasing their detectability.

However, this high buffer capacity of Purkinje cells was also responsible for the impossibility to discern single action potentials from their Ca^{2+}-dependent fluorescence signals. The calcium concentration changes in the Purkinje cells are greatly reduced by this high concentration of Ca^{2+}-binding proteins, which only enables a possible range of changes between 30 nM (baseline level from Fierro et al., 1998) and around 200 nM with realistic cell depolarizations (in current clamp; Tank et al., 1988). This means that the Ca^{2+} buffers rapidly capture the Ca^{2+} ions traversing the membrane after each action potential, and also that just a fraction of the available dynamic range from the Ca^{2+} indicators is usable to report fluorescence changes. Therefore, each action potential can only contribute with a very small increase in fluorescence as we see on the slices ($0.1\% \pm 0.03\%$ $\Delta F/F$) and the *in vivo* results (maximum estimated of 0.0371 ± 0.0089 counts).

In tandem with the protein buffer system, Purkinje cells have mechanisms for slow clearance of Ca^{2+} from the cell cytoplasm, such as membrane pumps, transporters and sequestration inside organelles (Fierro et al., 1998). These mechanisms contribute to the slow decay times of the fluorescence fluctuations seen in our results. The measured value of this decay

time in slices ($\tau = 7.2 \pm 2.1$ s) and in two of the cells *in vivo* ($\tau = 8.83 \pm 1.76$ s; 7.62 ± 1.92 s) was slightly slower that the values found by (Leonardo Fierro et al., 1998) ($2 < \tau 2 < 6.5$ s). Considering the fact that the decay time decreases with higher calcium concentrations (Leonardo Fierro et al., 1998), this modest difference might come from the lower calcium concentration in our spontaneous recordings compared to their voltage-clamped depolarizations. Nonetheless, one of our *in vivo* recordings showed a faster decay time in agreement with those previous reports ($\tau = 2.77 \pm 0.38$ s), which implies that the big variability of decay times seen in (Leonardo Fierro et al., 1998) might also appear *in vivo*.

In a more recent batch of experiments, it was confirmed that depolarization of the soma (produced by current injection in PC cells on cultures in (Gruol et al., 2010); or by indirect stimulation of PCs in slices via mossy fibers in Gandolfi et al., 2014) causes an increase in calcium proportional to the strength of the stimuli (measured with fura-2). We confirmed that it was also our case, as the fluorescence changes in stereotypical responses extracted from several cells showed the same linear relationship to the depolarization strength (measured as the density of action potentials in a fixed time; see Fig. 3.2.E). In agreement with the both results from Gruol et al., 2010 and Gandolfi et al., 2014, it was not possible to discern the effect of a single action potential just as we demonstrated before.

Additionally, Gruol et al., 2010 also found that there are nuclear Ca^{2+} signals triggered by PC depolarization that could reach higher amplitudes than the cytoplasmic Ca^{2+} signals (probably caused by a different calcium buffering environment). We avoided these nuclear signals in our experiments by loading our Ca^{2+} indicators only to the cytoplasm through the targeted cytosolic expression of the GCaMP6f gene *in vivo* (when no overexpression occurred).

4.1.1. Specificity of the somatic calcium signals for simple spikes, not complex spikes

In our slice experiments, we saw that the Ca^{2+} signals coming from simple and complex spikes were different between the somatic and dendritic compartments, in agreement with previous reports on the subject (Eilers et al., 1995; Kano et al., 1992; Tank et al., 1988). However, the epifluorescence technique that we used for imaging was inadequate to resolve the spatial fluorescent signals coming from neighboring structures on the OGB1-loaded cells. Therefore, it was not possible to confirm unequivocally that the somatic signals were not contaminated with the

high brightness of the dendritic signals, or even from the nuclear responses mentioned before (Gruol et al., 2010). We performed 2-photon calcium imaging on *in vivo* experiments where the cells had both their dendrites and somas in the same plane, thus conserving the signals without any mixing. We can confirm that both slices and *in vivo* experiments showed the same difference between somatic and dendritic signals coming from complex spikes, as the estimated dendrite/soma signal ratio in slices (36.2 ± 5.4 % / 1.9 ± 0.2 % = 19.05 ± 3.48) contains the found ratio of 16.875 *in vivo*. In turn, this validates the previous findings that complex spike Ca^{2+} signals are confined to the dendrites, and in consequence, that somatic Ca^{2+} signals are essentially conveying only the simple spike behavior of the cells.

4.1.2. Detection of somatic calcium fluctuations in Purkinje cells of awake animals

It is also worth mentioning that the somatic Ca^{2+} fluctuations associated with Purkinje cell activity were detected in awake animals as seen in our preliminary results with the running wheel behavior. On the writing process of this thesis, an additional evidence was uploaded as a preprint showing Ca^{2+}-dependent fluctuations on fluorescent Purkinje cell somas triggered by a reward-anticipation paradigm using licking behavior in Crus II (Deverett, Koay, Oostland, & Wang, 2018).

4.2. Limitations of our imaging method for estimation of firing activity in Purkinje cells

Most of the published literature regarding the use of calcium imaging as an estimator of spike timings in neurons concur with a consistent unitary calcium response per spike in accordance to a convolutional model (Deneux et al., 2016; Henry Lütcke and Fritjof Helmchen, 2011; Park, Bobkov, Ache, & Principe, 2013; Theis et al., 2016; Vogelstein et al., 2009; Yaksi & Friedrich, 2006). However, in almost all cases studied the calcium response per spike was clearly above the background noise, considering that the individual calcium events could be spotted by eye. In our case, it is not possible to recognize the effect of a single action potential on the PC somatic calcium signal above the noise; instead, only the summation of several of them is detectable. To make things more difficult, the Ca^{2+} indicator we used *in vivo* has a known nonlinearity that distorts the signals, which hinders the action potentials fired in a context of low (and also high) internal Ca^{2+} concentration (Yamada & Mikoshiba, 2016). To overcome these difficulties, we designed a

different convolutional model that took into consideration the nonlinear biophysical characteristics from the GCaMP6f (or similar) calcium indicator. To achieve this, we had to deconstruct the complete data acquisition process and analyze its components separately as will be described below.

4.2.1. Calcium imaging signal acquisition as a block-structured nonlinear system

From a signal processing perspective, any open system with measurable inputs and outputs but an inaccessible intermediate stage can be approximated to a set of simpler and independent subsystems connected through cause-effect relationships (also known as transfer functions; Hunter & Korenberg, 1986). This approach is colloquially recognized as the "black box" interpretation. Applying this to our case, the acquisition process starts with the input corresponding to the spike timings of the Purkinje cell, and finishes with an output of the fluorescence counts coming out of the imaging set-up. In between the two, we have the "black-box" with all the intermediate subsystems inaccessible for us to measure from the preparation: (1) the Ca^{2+} entry to the cell per spike or Ca^{2+}-spike convolution, (2) the Ca^{2+} binding to GCaMP6f, and (3) the detection of photons arriving to the PMT (for a graphical representation, see Fig 2.10.). In general, this particular array of subsystems corresponds to a Linear – Non-linear – Linear sandwich (called also an LNL cascade). For our purposes in the thesis, only the modeling of the LNL system was required to test the relationship between the firing activity and the GCaMP6f fluorescence from Purkinje cells. To understand more easily the limitation of this model, we could try to go conceptually "backwards" and try to extract the original input using an already modeled system (therefore, estimating the spike activity directly from a fluorescence trace).

To start, the LNL system can be interpreted as a filter with a non-linear transfer function. Conversely, if its transfer function is known and invertible (its anti-function is defined) then applying its inverse function to the outputs must reverse its effect on the system and retrieve the original inputs (Y. Jung & M. Enqvist, 2013). This can be done by using a Wiener system designed as an exact inverse from the modeled LNL cascade (Solé-Casals & Caiafa, 2011). In theory, this Wiener system would first deconvolve the output of the LNL system (with a Wiener deconvolution) and then "linearize" its outcome by applying the inverse function from the non-linear block (the inverted θ_{trans} function, which is defined), resulting in a estimation of the original spiking activity. However, there are some practical limitations of this approach arising

from (1) the noise that contaminate the signals which limit the efficiency of the deconvolution and (2) the inaccuracy of the estimated parameters for θ_{trans} that could miscalculate the linear function.

4.2.2. Confounding noise in the signal deteriorates estimation of spike activity

In respect to the noise limitation, each subsystem in the model can have its own noise sources causing an accumulation of "misinformation" that result in erroneous estimations. For instance, one of such noise sources was the putative calcium signals from complex spikes in the Purkinje cell somas that could have tampered the detection of the simple spike signals at the level of the first linear operand (the Ca^{2+}-spike convolution). Fortunately, it seems that there is not a significant contribution of these collateral noises in our system, corroborated by the good fit of the responses, so the estimation should be very close to the original signal. However, the low level of photon counts recorded from the *in vivo* experiments predispose the signal to a high influence of shot noise, which heavily deteriorates the estimation (i.e. the variance of the shot noise can be modelled as the square root of the number of photon counts; (Wilt et al., 2013). Fortunately, this noise is partly reduced by the averaging of pixels using the Region of Interest (ROI) analysis. So, to avoid this noise, it is recommended to employ recording configurations with a spatial resolution that has at least 20 pixels covering the area of a Purkinje soma (as the shot noise variance in that condition would be divided by 20, e.g. for a signal average of 1 count: $\sqrt{1}/20 = 0.05$ counts of variance).

4.2.3. Estimation accuracy of the nonlinear function parameters

In terms of the limitations on the model parameter estimation, it is hard to guess ab initio their values to use in the fitting of the GCaMP6f calcium signals. Nevertheless, in this particular problem the nonlinearities can help to find these values, as they serve as "internal boundaries" of the fitting procedure. For instance, as the cell approaches one of the nonlinear states (baseline or saturation), it gets easier to estimate the true asymptotic level as it naturally limits the incursions of the cell signals (in our model, F_{min} for baseline, or F_{max} for saturation respectively). As an example, our *in vivo* recordings in anesthetized animals showed two cells with very long silent states that let the calcium reach its baseline levels, thereby giving up the value for the F_{min} value by default. This approach has been already studied and exploited to aid the fitting of convolutional models designed to estimate calcium concentrations without ratiometric probes

(Maravall, Mainen, Sabatini, & Svoboda, 2000) and to improve the spike estimation of blind deconvolution approaches (Vogelstein et al., 2009).

However, Purkinje cells in awake animals are more likely to stay in an almost constant firing state that settles their calcium range far from the nonlinearities and in the linear regime of the calcium indicator (as the case of cell A in Fig 3.5.). We assume this might be the case as many reports of spontaneous electrical recording in Purkinje cells *in vivo* exhibit high spiking activity (Cao et al., 2017; S. Chen et al., 2016; de Solages et al., 2008; Johansson, Jirenhed, Rasmussen, Zucca, & Hesslow, 2014; Schonewille et al., 2006; Shin et al., 2007). For this reason, it might be useful to construct a set of initial guesses from measurement in simultaneous cell-attached and calcium imaging recordings of GCaMP6f-loaded Purkinje cells in slices. The advantage of such an experiment is the high number of cells that can be recorded with only one set of slices from one animal, thus sampling enough cases to address the variability that is readily seen in our current fitting results of the cells.

4.3. Synchronization of Purkinje cells mediated by GABAergic network

Profiting from the high number of cells that can be recorded in cerebellar slices, we performed experiments to test the synchronization of several pairs of Purkinje cells employing spontaneous cell-attached and OGB1 imaging recordings (Fig 3.4.). We found clear non-random synchronization of the PCs confined to the parasagittal planes of the cerebellum, which extended up to 200 µm away from the cell in the same direction (which corresponds to the orientation and length of interneuron axonal projections; Zorrilla de San Martin et al., 2015). This result is also supported by the findings of (Dizon & Khodakhah, 2011), who stimulated granule cells using spotted glutamate uncaging at several distances around the Purkinje cells. They saw a very similar loss of responses at the same length and orientation as in our results. Also, both the measurement of synchronization we obtained and the responses to granule cell excitation from (Dizon & Khodakhah, 2011) were blocked by gabazine, an antagonist of the $GABA_A$ receptor, implying that GABAergic synapses are involved.

Although it looks likely that the GABAergic activity of interneurons is responsible for this results, there's also the possibility that Purkinje cells collaterals play a role too. Both types of synapses are constricted to the sagittal plane, delivering an inhibitory signal to Purkinje cells

(Orduz & Llano, 2007) and potentially synchronizing their activity at long distances. Other inhibitory elements, such as Golgi cells, are unlikely to cause this response pattern as their action is not restricted exclusively to the sagittal plane and they are not connected directly to the Purkinje cells (Palay & Chan-Palay, 1974) .

4.4. Considerations for populational calcium imaging on Purkinje cells *in vivo*

From the experience gathered in performing and analyzing our *in vivo* experiments, both in anesthetized and awake conditions, we collected hints and methods that could be useful to consider for next experimentation attempts.

4.4.1. Microdomain differences in firing rate of Purkinje cells ensembles

The cerebellum is a complex organ organized at many different levels. Although it has a conserved cytoarchitecture throughout its extension, it presents regional subdivisions identified with the expression of specific proteins (e.g. Zebrin II, EAAT4, CART) in the Purkinje cells, which are arranged in stripes along the sagittal plane (Cerminara, Lang, Sillitoe, & Apps, 2015). These bands run symmetrically along the sagittal axis through the cerebellum but are not equally distributed along the lobules, for example, lobule V contains predominantly Zebrin II- Purkinje cells whilst lobule VIII contains mostly Zebrin II+ (Ozol, Hayden, Oberdick, & Hawkes, 1999). To date, it is known that each microdomain have different physiological behavior in terms of the firing activity of Purkinje cells (Zhou et al., 2014, 2015), being higher in Zebrin II- than in Zebrin II+. It has also been demonstrated that each microdomain preserves its differences even in presence of anesthetics, like urethane and ketamine/xylazine (Xiao et al., 2014). Overall, this regional differentiation suggest a more complex distribution of cerebellar functions than predicted from the classical cerebellum conceptions (Cerminara et al., 2015).

It is possible that most of the result variability within our findings in anaesthetized mice has to do with the difference between the physiology of the cerebellar microdomains. For instance, our difficulty locating the spontaneously active groups of Purkinje cells might come from the lobule V predominance of Zebrin II- cells with fast and regular spiking patterns (Zhou et al., 2014). With calcium imaging, those cells would have been seen with an almost constant fluorescence signal that would have passed inadvertently while searching for fluctuating cells. Consequently, it

is very likely that the Purkinje cells with spontaneous activity that we recorded were part of the scarce Zebrin II+ cells in the small patches of the lobule V (Ozol et al., 1999). According to the results from Xiao et al., 2014, Zebrin II+ cells are very sensitive to ketamine/xylazine anesthesia, generating a strong increase in their spiking irregularity (the standard deviations of their spike timings increase dramatically). This fact, which might explain the variety of ketamine effects reported in the cerebellum (as outlined in Section 3.2.3.), might also explain why our recorded cells had such strange firing behavior. Therefore, to address this source of variability it is recommended to keep track of the type and/or location of cells recorded when possible.

4.4.2. Pseudo-ratiometric imaging of GCaMP6f and next frontiers in calcium indicators

The use of the 820 nm excitation wavelength to detect the fluorescence of the calcium-unbound GCaMP6f protein turned out to be a very useful control to measure the effect of the movement artifacts on the *in vivo* experiments. It might be possible to develop this method into a pseudo-ratiometric approach by calibrating the ratio of the Ca^{2+} sensitive and insensitive measurements, analogous to the situation with two dye / two wavelength approaches (Oheim, Naraghi, Muller, & Neher, 1998). However, in the current state of Ca^{2+} indicator development, there are two intriguing options that could further potentiate the imaging techniques: the ratiometric GCaMP-R (Cho et al., 2017) which would overrule the need to perform the previous pseudo-ratiometric calibrations, and the advancements of genetically encoded voltage indicators (GEVIs) for 2-photon imaging (Xu, Zou, & Cohen, 2017). With GEVIs, it might be possible to overcome the slow dynamics of the calcium imaging techniques we have experienced in this thesis (with low spike identification resolution and slow decay of responses) and directly measure the more relevant electrical behavior of Purkinje cells.

4.4.3. Spontaneous vs stereotyped behavior for somatic calcium imaging in awake experiments

In this thesis, we used two different approaches to record activity of ensembles of Purkinje cells in the cerebellar cortex: (1) the single-shot recordings of spontaneous activity from cells in acute experiments, and (2) the averaged recordings over a stereotyped behavioral response in awake mice. At first glance, the averaged approach has indisputable advantages over the single-shot in terms of noise reduction and generalization capabilities, as is seen in the analysis summary of the preliminary results in the awake animal (Fig 3.10). However, it is important to keep in mind

that Purkinje cells are nonlinear elements in the circuitry of the cerebellum that have the mechanism to toggle from different activity states by the same type of stimuli (Oldfield et al., 2010) and that can acquire new activity regimes from learned input associations (Johansson et al., 2014). These facts erodes the assumption that Purkinje cells have a completely stereotyped activity in normal conditions, as these cells have to (un)learn trends from the ever-changing context of the animal (as expected from the adaptive filter model of the cerebellum; Bell et al., 2008).

In order to unfold the development of such changes, in this thesis we proposed a method (*envelope thresholding*, section 2.4.4.) to extract the relevant features of single-shot recordings from th0e spontaneous activity of Purkinje cells in 2-photon imaging. The advantage of this method, compared to many other possible heuristic implementations, is its easy application to any kind of time series, its straightforward interpretation based on noise-driven uncertainty, and its effective detection of multiple change-points. Moreover, it could be used in conjunction with the averaged recording approach to automatize the detection of features for big data scenarios.

5. CONCLUSIONS

The cerebellum, and its evolutionary relatives, are remarkable biological control processors. They are in charge of the selection and association of a huge amount of information collected by the animal about itself and its surroundings, so that they are transformed into a modeled negative image (Sawtell, 2017). This negative "mold" of the animal's experience of the world is stored inside the cerebellum circuit to compute a mask of expected outcomes. For usual and expected chores, the predicted mask fits and cancels the perceived task, thus concealing the irrelevant sensory information of the chores from the attention of other processes. However, if this mask stops fitting, suddenly the "mold is broken" and an exception is detected; hence prompting a correction or an enhancement to be done over the animal's behavior. This filtering mechanism becomes truly useful once it is accompanied by the learning of new "molds" to make new fitting masks, so the filter adapts itself to new trends and captures new changes. Incredibly, all of these processes are carried out by just a few types of cellular elements arranged in a crystal-like structure in the cerebellum.

In biological terms, the negative image molded from the mossy and climbing fiber inputs reaching the molecular layer elements in the cerebellum is compiled by the Purkinje cells to form a collective masking signal that attenuates the output of deep cerebellar nuclei cells. Inside of this processing cascade, the functional block of the collective Purkinje-to-DCN link stands out as being the place where the negative image and the sensory input collide and subtract each other out. However, for the proper analysis of this functional block inside the cerebellum, a method to record the output from multiple Purkinje cells was required (for at least 20 to 50 cells that connect to a DCN cell; (Person & Raman, 2012). As the time being, multi-photon calcium imaging is the best solution to record simultaneously from Purkinje cells deep inside the molecular layer of the cerebellum. In this thesis, I am pleased to show the development of a calcium imaging approach designed to acquire the output information encoded from populations of these cells.

The imaging method we devised was inspired from the physiological characteristics of Purkinje cells, exhaustively researched since the late 1970's (Llinás & Sugimori, 1980a, 1980b). We showed that spontaneous actions potentials in the Purkinje cell membrane cause a proportional influx of Ca^{2+} ions inside the cell, as expected from the described activity of its P/Q-type voltage-dependent Ca^{2+} channels. This Ca^{2+} influx in the Purkinje soma was only related to the contribution

from simple spike depolarizations, and it was isolated from the large dendritic Ca^{2+} influx generated by complex spikes. Therefore, we used Ca^{2+} indicators (OGB1 and GCaMP6f) to report the calcium concentration changes generated by the spontaneous discharges of simple spikes, without any indication of disruption of the cell's tight intracellular Ca^{2+} regulation. Despite the limitations attributable to the slow signal kinetics and occasional nonlinearities of the calcium fluorescent indicators that distort the estimations of the underlying electrical activity in Purkinje cells, our method could extract the output activity of Purkinje cells in slices, acute experiments and awake animals.

Furthermore, this imaging method allowed us to examine the coordination of Purkinje cell activity between the sagittal and horizontal planes by using cerebellar slices. OGB1-loaded Purkinje cells oriented in the horizontal plane did not show synchronized activity, however, cells oriented in the sagittal plane had a significant number of synchronized changes in their activity. This result was confirmed with paired electrical recordings of spontaneous simple spike discharges between neighboring Purkinje cells in sagittal slices, which showed coordination of Purkinje cells separated by less than 200 μm in the molecular layer. This sagittal coordination of Purkinje cells is dependent on the GABAergic network of the cerebellum that is confined to that plane, such as the one constituted by molecular layer interneurons, and possibly from recurrent axonal collaterals form Purkinje cells.

6. PERSPECTIVES

With the imaging method we developed in this thesis, it is now possible to extract information from the activity patterns of Purkinje cells that modulate the activity of downstream targets in the DCN. It should be possible to identify the groups of Purkinje cells associated to a particular behavior by just looking for fluctuations of their somatic calcium signals triggered by the corresponding behavioral changes *in vivo* (like we did for the awake preliminary results by seeing fluctuations whenever the animal run; section 3.3). Some other behaviors, like licking or whisking (Cao, Maran, Dhamala, Jaeger, & Heck, 2012; Rahmati et al., 2014), might also be possible to study at the Purkinje cell output level as long as the cerebellar region related to the behavior is optically accessible.

Microdomains in the cerebellum have been characterized with electrophysiology and molecular markers (Zhou et al., 2014), but a more comprehensive study of their physiological relevance might be attained by studying the simultaneous activity of the cells between each Zebrin band. By using specific markers of the Zebrin bands (e.g. EAAT4) the identification of the bands for imaging experiments might also be straightforward.

To date, the study of cerebellar learning processes related to Purkinje activity have mostly focused in reduced numbers of Purkinje cell units recorded at a time through electrophysiological methods (e.g. Johansson et al., 2014). However, as Purkinje cells project onto the DCN with a high convergence ratio (Person & Raman, 2012), it is more likely that the learning processes are spread across large groups of Purkinje cells. Our imaging method might be able to follow the acquisition of new activity patterns associated to learning in several Purkinje cells simultaneously. However, specific experiments are needed that can isolate the cerebellar learning from the contribution of other brain areas. For that, two disjoint inputs from different sensory modalities can be used to make the animal associate them in anticipation of a reward (e.g. Whisker stimuli and licking, Rahmati et al., 2014).

7. REFERENCES

Aida, S., Fujiwara, N., & Shimoji, K. (1994). Differential regional effects of ketamine on spontaneous and glutamate-induced activities of single CNS neurones in rats. *British Journal of Anaesthesia*, *73*(3), 388–394. https://doi.org/10.1093/bja/73.3.388

Akerboom, J., Chen, T.-W., Wardill, T. J., Tian, L., Marvin, J. S., Mutlu, S., … Looger, L. L. (2012). Optimization of a GCaMP calcium indicator for neural activity imaging. *The Journal of Neuroscience : The Official Journal of the Society for Neuroscience*, *32*(40), 13819–13840. https://doi.org/10.1523/JNEUROSCI.2601-12.2012

Astorga, G., Bao, J., Marty, A., Augustine, G. J., Franconville, R., Jalil, A., … Llano, I. (2015). An excitatory GABA loop operating in vivo. *Frontiers in Cellular Neuroscience*, *9*, 275. https://doi.org/10.3389/fncel.2015.00275

Baker, C. A., Kohashi, T., Lyons-Warren, A. M., Ma, X., & Carlson, B. A. (2013). Multiplexed temporal coding of electric communication signals in mormyrid fishes. *The Journal of Experimental Biology*, *216*(13), 2365–2379. https://doi.org/10.1242/jeb.082289

Barnett, L. M., Hughes, T. E., & Drobizhev, M. (2017). Deciphering the molecular mechanism responsible for GCaMP6m's Ca2+-dependent change in fluorescence. *PLOS ONE*, *12*(2), e0170934. https://doi.org/10.1371/journal.pone.0170934

Basson, M., & J Wingate, R. (2013). *Congenital hypoplasia of the cerebellum: Developmental causes and behavioral consequences* (Vol. 7). https://doi.org/10.3389/fnana.2013.00029

Bastianelli, E. (2003). Distribution of calcium-binding proteins in the cerebellum. *The Cerebellum*, *2*(4), 242–262. https://doi.org/10.1080/14734220310022289

Bell, C. (1981). An efference copy which is modified by reafferent input. *Science*, *214*(4519), 450–453. https://doi.org/10.1126/science.7291985

Bell, C., Han, V., & Sawtell, N. (2008). Cerebellum-Like Structures and Their Implications for Cerebellar Function. *Annual Review of Neuroscience*, *31*(1), 1–24. https://doi.org/10.1146/annurev.neuro.30.051606.094225

Bengtsson, F., & Jörntell, H. (2007). Ketamine and Xylazine Depress Sensory-Evoked Parallel Fiber and Climbing Fiber Responses. *Journal of Neurophysiology*, *98*(3), 1697–1705. https://doi.org/10.1152/jn.00057.2007

Berlin, S., Carroll, E. C., Newman, Z. L., Okada, H. O., Quinn, C. M., Kallman, B., … Isacoff, E. Y. (2015). Photoactivatable genetically encoded calcium indicators for targeted neuronal imaging. *Nature Methods*, *12*, 852. Retrieved from http://dx.doi.org/10.1038/nmeth.3480

Bodznick, D., Montgomery, J. C., & Carey, M. (1999). Adaptive mechanisms in the elasmobranch hindbrain. *Journal of Experimental Biology*, *202*(10), 1357.

Callewaert, G., Eilers, J., & Konnerth, A. (1996). Axonal calcium entry during fast 'sodium' action potentials in rat cerebellar Purkinje neurones. *The Journal of Physiology*, *495*(Pt 3), 641–647. Retrieved from http://www.ncbi.nlm.nih.gov/pmc/articles/PMC1160771/

Campagnola, L., Kratz, M. B., & Manis, P. B. (2014). ACQ4: an open-source software platform for data acquisition and analysis in neurophysiology research. *Frontiers in Neuroinformatics*, *8*. https://doi.org/10.3389/fninf.2014.00003

Cao, Y., Liu, Y., Jaeger, D., & Heck, D. H. (2017). Cerebellar Purkinje Cells Generate Highly Correlated Spontaneous Slow-Rate Fluctuations. *Frontiers in Neural Circuits*, *11*. https://doi.org/10.3389/fncir.2017.00067

Cao, Y., Maran, S. K., Dhamala, M., Jaeger, D., & Heck, D. H. (2012). Behavior-Related Pauses in Simple-Spike Activity of Mouse Purkinje Cells Are Linked to Spike Rate Modulation. *The Journal of Neuroscience*, *32*(25), 8678. https://doi.org/10.1523/JNEUROSCI.4969-11.2012

Castejón, O. J. (2003). The Basket Cells. In O. J. Castejón (Ed.), *Scanning Electron Microscopy of Cerebellar Cortex* (pp. 77–80). Boston, MA: Springer US. https://doi.org/10.1007/978-1-4615-0159-6_10

Cerminara, N. L., Lang, E. J., Sillitoe, R. V., & Apps, R. (2015). Redefining the cerebellar cortex as an assembly of non-uniform Purkinje cell microcircuits. *Nature Reviews Neuroscience*, *16*, 79. Retrieved from http://dx.doi.org/10.1038/nrn3886

Chen, S., Augustine, G. J., & Chadderton, P. (2016). The cerebellum linearly encodes whisker position during voluntary movement. *ELife*, *5*, e10509. https://doi.org/10.7554/eLife.10509

Chen, T.-W., Wardill, T. J., Sun, Y., Pulver, S. R., Renninger, S. L., Baohan, A., … Kim, D. S. (2013). Ultra-sensitive fluorescent proteins for imaging neuronal activity. *Nature*, *499*(7458), 295–300. https://doi.org/10.1038/nature12354

Cho, J.-H., Swanson, C. J., Chen, J., Li, A., Lippert, L. G., Boye, S. E., … Chow, R. H. (2017). The GCaMP-R Family of Genetically Encoded Ratiometric Calcium Indicators. *ACS Chemical Biology*, *12*(4), 1066–1074. https://doi.org/10.1021/acschembio.6b00883

de Solages, C., Szapiro, G., Brunel, N., Hakim, V., Isope, P., Buisseret, P., … Léna, C. (2008). High-Frequency Organization and Synchrony of Activity in the Purkinje Cell Layer of the Cerebellum. *Neuron*, *58*(5), 775–788. https://doi.org/10.1016/j.neuron.2008.05.008

Dean, P., Porrill, J., Ekerot, C.-F., & Jörntell, H. (2009). The cerebellar microcircuit as an adaptive filter: experimental and computational evidence. *Nature Reviews Neuroscience*, *11*, 30. Retrieved from http://dx.doi.org/10.1038/nrn2756

Deneux, T., Kaszas, A., Szalay, G., Katona, G., Lakner, T., Grinvald, A., … Vanzetta, I. (2016). Accurate spike estimation from noisy calcium signals for ultrafast three-dimensional imaging of large neuronal populations in vivo. *Nature Communications*, *7*, 12190. https://doi.org/10.1038/ncomms12190

Deverett, B., Koay, S. A., Oostland, M., & Wang, S. S.-H. (2018). A cerebellar role in evidence-guided decision-making. *BioRxiv*. https://doi.org/10.1101/343095

Dizon, M. J., & Khodakhah, K. (2011). The role of interneurons in shaping Purkinje cell responses in the cerebellar cortex. *The Journal of Neuroscience*, *31*(29), 10463–10473. https://doi.org/10.1523/JNEUROSCI.1350-11.2011

Eilers, J., Callewaert, G., Armstrong, C., & Konnerth, A. (1995). Calcium signaling in a narrow somatic submembrane shell during synaptic activity in cerebellar Purkinje neurons. *Proceedings of the National Academy of Sciences of the United States of America*, *92*(22), 10272–10276. Retrieved from http://www.ncbi.nlm.nih.gov/pmc/articles/PMC40778/

Fierro, L, & Llano, I. (1996). High endogenous calcium buffering in Purkinje cells from rat cerebellar slices. *The Journal of Physiology*, *496*(Pt 3), 617–625. Retrieved from http://www.ncbi.nlm.nih.gov/pmc/articles/PMC1160850/

Fierro, Leonardo, DiPolo, R., & Llano, I. (1998). Intracellular calcium clearance in Purkinje cell somata from rat cerebellar slices. *The Journal of Physiology*, *510*(Pt 2), 499–512. https://doi.org/10.1111/j.1469-7793.1998.499bk.x

Floreano, D., Ijspeert, A. J., & Schaal, S. (2014). Robotics and Neuroscience. *Current Biology*, *24*(18), R910–R920. https://doi.org/10.1016/j.cub.2014.07.058

Franconville, R. (2010). *L' imagerie calcique pour l'étude des réseaux de neurones, possibilités et limites : application à l'étude in vivo des interneurones du cervelet de souris par microscopie biphotonique*.

Franconville, R., Revet, G., Astorga, G., Schwaller, B., & Llano, I. (2011). Somatic calcium level reports integrated spiking activity of cerebellar interneurons in vitro and in vivo. *Journal of Neurophysiology*, *106*(4), 1793–1805. https://doi.org/10.1152/jn.00133.2011

Gaertner, D. J., Hallman, T. M., Hankenson, F. C., & Batchelder, M. A. (2008). Chapter 10 - Anesthesia and Analgesia for Laboratory Rodents A2 - Fish, Richard E. In M. J. Brown, P. J. Danneman, & A. Z. Karas (Eds.), *Anesthesia and Analgesia in Laboratory Animals (Second Edition)* (pp. 239–297). San Diego: Academic Press. https://doi.org/10.1016/B978-012373898-1.50014-0

Gaffield, M. A., Amat, S. B., Bito, H., & Christie, J. M. (2015). Chronic imaging of movement-related Purkinje cell calcium activity in awake behaving mice. *Journal of Neurophysiology*, *115*(1), 413–422. https://doi.org/10.1152/jn.00834.2015

Gandolfi, D., Pozzi, P., Tognolina, M., Chirico, G., Mapelli, J., & D'Angelo, E. (2014). The spatiotemporal organization of cerebellar network activity resolved by two-photon imaging of multiple single neurons. *Frontiers in Cellular Neuroscience*, *8*, 92. https://doi.org/10.3389/fncel.2014.00092

Gauck, V., & Jaeger, D. (2000). The control of rate and timing of spikes in the deep cerebellar nuclei by inhibition. *The Journal of Neuroscience*, *20*(8), 3006–3016. Retrieved from http://www.jneurosci.org/content/20/8/3006.short

Geoface. (2016). *Mouse Brain Anatomy In Skull* [Website]. Retrieved from http://geoface.info/ef8714/mouse-brain-anatomy-in-skull

Giovannucci, A., Badura, A., Deverett, B., Najafi, F., Pereira, T. D., Gao, Z., … Wang, S. S.-H. (2017). Cerebellar granule cells acquire a widespread predictive feedback signal during motor learning. *Nature Neuroscience*, *20*(5), 727–734. https://doi.org/10.1038/nn.4531

Grienberger, C., & Konnerth, A. (2012). Imaging Calcium in Neurons. *Neuron*, *73*(5), 862–885. https://doi.org/10.1016/j.neuron.2012.02.011

Gruol, D. L., Netzeband, J. G., & Nelson, T. E. (2010). Somatic Ca2+ signaling in cerebellar Purkinje neurons. *Journal of Neuroscience Research*, *88*(2), 275–289. https://doi.org/10.1002/jnr.22204

Hammamatsu Photonics. (2007). Chapter 8: Photomultiplier Tube Modules. In *PMT Handbook* (3rd ed., p. 160). Retrieved from https://www.hamamatsu.com/resources/pdf/etd/PMT_handbook_v3aE-Chapter8.pdf

Harris, K. D., Quian Quiroga, R., Freeman, J., & Smith, S. (2016). Improving data quality in neuronal population recordings. *Nature Neuroscience*, *19*(9), 1165–1174. https://doi.org/10.1038/nn.4365

Hasinoff, S. W. (2014). Photon, Poisson Noise. In K. Ikeuchi (Ed.), *Computer Vision* (pp. 608–610). Boston, MA: Springer US. https://doi.org/10.1007/978-0-387-31439-6_482

Häusser, M., & Clark, B. A. (1997). Tonic Synaptic Inhibition Modulates Neuronal Output Pattern and Spatiotemporal Synaptic Integration. *Neuron*, *19*(3), 665–678. https://doi.org/10.1016/S0896-6273(00)80379-7

Helassa, N., Podor, B., Fine, A., & Török, K. (2016). Design and mechanistic insight into ultrafast calcium indicators for monitoring intracellular calcium dynamics. *Scientific Reports*, *6*, 38276. Retrieved from http://dx.doi.org/10.1038/srep38276

Henry Lütcke and Fritjof Helmchen. (2011). Two-photon imaging and analysis of neural network dynamics. *Reports on Progress in Physics*, *74*(8), 086602. Retrieved from http://stacks.iop.org/0034-4885/74/i=8/a=086602

Hevers, W., Hadley, S. H., Lüddens, H., & Amin, J. (2008). Ketamine, But Not Phencyclidine, Selectively Modulates Cerebellar $GABA_A$ Receptors Containing α6 and δ Subunits. *The Journal of Neuroscience*, *28*(20), 5383. https://doi.org/10.1523/JNEUROSCI.5443-07.2008

Hoogland, T. M., & Kuhn, B. (2010). Recent Developments in the Understanding of Astrocyte Function in the Cerebellum In Vivo. *The Cerebellum*, *9*(3), 264–271. https://doi.org/10.1007/s12311-009-0139-z

Hudson, A. E. (2018). Chapter Twelve - Genetic Reporters of Neuronal Activity: c-Fos and G-CaMP6. In R. G. Eckenhoff & I. J. Dmochowski (Eds.), *Methods in Enzymology* (Vol. 603, pp. 197–220). Academic Press. https://doi.org/10.1016/bs.mie.2018.01.023

Hunter, I. W., & Korenberg, M. J. (1986). The identification of nonlinear biological systems: Wiener and Hammerstein cascade models. In *Biological Cybernetics* (Vol. 55, pp. 135–144). Springer-Verlag. https://doi.org/10.1007/BF00341929

Ito, M. (2012). *The Cerebellum: Brain for an Implicit Self* (1st ed.). USA: Pearson Education. Retrieved from https://books.google.com.co/books?hl=es&lr=&id=RwR94p9wS-8C&oi=fnd&pg=PR7&dq=Ito,+M.+(2012).+The+Cerebellum:+Brain+for+an+Implicit+Self&ots=YsBPXEPcyg&sig=o3MeDbuB3F1teUXn_Uez6CiLado#v=onepage&q&f=false

Ito, M., & Kano, M. (1982). Long-lasting depression of parallel fiber-Purkinje cell transmission induced by conjunctive stimulation of parallel fibers and climbing fibers in the cerebellar cortex. *Neuroscience Letters*, *33*(3), 253–258. https://doi.org/10.1016/0304-3940(82)90380-9

Janelia. (2018, June 4). Two-Photon Fluorescent Probes | Janelia Research Campus | HHMI. Retrieved 4 June 2018, from https://www.janelia.org/lab/harris-lab-apig/research/photophysics/two-photon-fluorescent-probes

Johansson, F., Jirenhed, D.-A., Rasmussen, A., Zucca, R., & Hesslow, G. (2014). Memory trace and timing mechanism localized to cerebellar Purkinje cells. *Proceedings of the National Academy of Sciences*, *111*(41), 14930–14934. https://doi.org/10.1073/pnas.1415371111

Kano, M., Rexhausen, U., Dreessen, J., & Konnerth, A. (1992). Synaptic excitation produces a long-lasting rebound potentiation of inhibitory synaptic signals in cerebellar Purkinje cells. *Nature*, *356*(6370), 601–604. https://doi.org/10.1038/356601a0

Kitamura, K., & Häusser, M. (2011). Dendritic Calcium Signaling Triggered by Spontaneous and Sensory-Evoked Climbing Fiber Input to Cerebellar Purkinje Cells In Vivo. *The Journal of Neuroscience*, *31*(30), 10847–10858. https://doi.org/10.1523/JNEUROSCI.2525-10.2011

Langner, G., & Scheich, H. (2009). *Electric Senses in Monotremes: Electroreception and Electrolocation in the Platypus and the Echidna*. https://doi.org/10.1007/978-3-540-29678-2_2919

Lin, M. T., Chen, C. F., & Pang, I. H. (1978). Effect of ketamine on thermoregulation in rats. *Canadian Journal of Physiology and Pharmacology*, *56*(6), 963–967.

Lin, M. Z., & Schnitzer, M. J. (2016). Genetically encoded indicators of neuronal activity. *Nature Neuroscience*, *19*, 1142. Retrieved from http://dx.doi.org/10.1038/nn.4359

Llano, I., Marty, A., Armstrong, C. M., & Konnerth, A. (1991). Synaptic- and agonist-induced excitatory currents of Purkinje cells in rat cerebellar slices. *The Journal of Physiology*, *434*, 183–213. Retrieved from http://www.ncbi.nlm.nih.gov/pmc/articles/PMC1181413/

Llinás, R, & Sugimori, M. (1992). The Electrophysiology of the Cerebellar Purkinje Cell Revisited. In Rodolfo Llinás & C. Sotelo (Eds.), *The Cerebellum Revisited* (pp. 167–181). New York, NY: Springer US. https://doi.org/10.1007/978-1-4612-2840-0_8

Llinás, Rodolfo, & Sugimori, M. (1980a). Electrophysiological properties of in vitro Purkinje cell dendrites in mammalian cerebellar slices. *The Journal of Physiology*, *305*(1), 197–213. https://doi.org/10.1113/jphysiol.1980.sp013358

Llinás, Rodolfo, & Sugimori, M. (1980b). Electrophysiological properties of in vitro Purkinje cell somata in mammalian cerebellar slices. *The Journal of Physiology*, *305*(1), 171–195. https://doi.org/10.1113/jphysiol.1980.sp013357

Loewenstein, Y., Mahon, S., Chadderton, P., Kitamura, K., Sompolinsky, H., Yarom, Y., & Häusser, M. (2005). Bistability of cerebellar Purkinje cells modulated by sensory stimulation. *Nature Neuroscience*, *8*(2), 202–211. https://doi.org/10.1038/nn1393

MacIver, M. A., Sharabash, N. M., & Nelson, M. E. (2001). Prey-capture behavior in gymnotid electric fish: motion analysis and effects of water conductivity. *Journal of Experimental Biology*, *204*(3), 543.

Maravall, M., Mainen, Z. F., Sabatini, B. L., & Svoboda, K. (2000). Estimating intracellular calcium concentrations and buffering without wavelength ratioing. *Biophysical Journal*, *78*(5), 2655–2667. Retrieved from http://www.ncbi.nlm.nih.gov/pmc/articles/PMC1300854/

Montgomery, J. C., & Bodznick, D. (2016). *Evolution of the cerebellar sense of self* (First edition). Oxford, United Kingdom: Oxford University Press.

Najafi, F., Giovannucci, A., Wang, S. S.-H., & Medina, J. F. (2014a). Coding of stimulus strength via analog calcium signals in Purkinje cell dendrites of awake mice. *ELife*, *3*, e03663. https://doi.org/10.7554/eLife.03663

Najafi, F., Giovannucci, A., Wang, S. S.-H., & Medina, J. F. (2014b). Sensory-Driven Enhancement of Calcium Signals in Individual Purkinje Cell Dendrites of Awake Mice. *Cell Reports*, *6*(5), 792–798. https://doi.org/10.1016/j.celrep.2014.02.001

Nakai, J., Ohkura, M., & Imoto, K. (2001). A high signal-to-noise Ca2+ probe composed of a single green fluorescent protein. *Nature Biotechnology*, *19*, 137. Retrieved from http://dx.doi.org/10.1038/84397

Oheim, M., Naraghi, M., Muller, T. H., & Neher, E. (1998). Two dye two wavelength excitation calcium imaging: results from bovine adrenal chromaffin cells. *Cell Calcium*, *24*(1), 71–84. https://doi.org/10.1016/S0143-4160(98)90090-2

Ohtsuki, G., Piochon, C., & Hansel, C. (2009). Climbing Fiber Signaling and Cerebellar Gain Control. *Frontiers in Cellular Neuroscience*, *3*, 4. https://doi.org/10.3389/neuro.03.004.2009

Oldfield, C. S., Marty, A., & Stell, B. M. (2010). Interneurons of the cerebellar cortex toggle Purkinje cells between up and down states. *Proceedings of the National Academy of Sciences*, *107*(29), 13153–13158. https://doi.org/10.1073/pnas.1002082107

Orduz, D., & Llano, I. (2007). Recurrent axon collaterals underlie facilitating synapses between cerebellar Purkinje cells. *Proceedings of the National Academy of Sciences*, *104*(45), 17831. https://doi.org/10.1073/pnas.0707489104

Ozden, I., Dombeck, D. A., Hoogland, T. M., Tank, D. W., & Wang, S. S.-H. (2012). Widespread State-Dependent Shifts in Cerebellar Activity in Locomoting Mice. *PLOS ONE*, *7*(8), e42650. https://doi.org/10.1371/journal.pone.0042650

Ozol, K., Hayden, J. M., Oberdick, J., & Hawkes, R. (1999). Transverse zones in the vermis of the mouse cerebellum. *The Journal of Comparative Neurology*, *412*(1), 95–111. https://doi.org/10.1002/(SICI)1096-9861(19990913)412:1<95::AID-CNE7>3.0.CO;2-Y

Palay, S. ., & Chan-Palay, V. (1974). *Cerebellar Cortex. Cytology and Organization* (1st ed.). Berlin: Springer Berlin.

Park, I. J., Bobkov, Y. V., Ache, B. W., & Principe, J. C. (2013). Quantifying bursting neuron activity from calcium signals using blind deconvolution. *Journal of Neuroscience Methods*, *218*(2), 10.1016/j.jneumeth.2013.05.007. https://doi.org/10.1016/j.jneumeth.2013.05.007

Person, A. L., & Raman, I. M. (2011). Purkinje neuron synchrony elicits time-locked spiking in the cerebellar nuclei. *Nature*, *481*(7382), 502–505. https://doi.org/10.1038/nature10732

Person, A. L., & Raman, I. M. (2012). Synchrony and neural coding in cerebellar circuits. *Frontiers in Neural Circuits*, *6*. https://doi.org/10.3389/fncir.2012.00097

Rahmati, N., Owens, C. B., Bosman, L. W. J., Spanke, J. K., Lindeman, S., Gong, W., … De Zeeuw, C. I. (2014). Cerebellar Potentiation and Learning a Whisker-Based Object Localization Task with a Time Response Window. *The Journal of Neuroscience*, *34*(5), 1949. https://doi.org/10.1523/JNEUROSCI.2966-13.2014

Ramakrishnan, K. B., Voges, K., De Propris, L., Zeeuw, D., I, C., & D'Angelo, E. (2016). Tactile Stimulation Evokes Long-Lasting Potentiation of Purkinje Cell Discharge In Vivo. *Frontiers in Cellular Neuroscience*, *10*. https://doi.org/10.3389/fncel.2016.00036

Ramirez, J. E., & Stell, B. M. (2016). Calcium Imaging Reveals Coordinated Simple Spike Pauses in Populations of Cerebellar Purkinje Cells. *Cell Reports*, *17*(12), 3125–3132. https://doi.org/10.1016/j.celrep.2016.11.075

Rothman, J. S., & Silver, R. A. (2018). NeuroMatic: An Integrated Open-Source Software Toolkit for Acquisition, Analysis and Simulation of Electrophysiological Data. *Frontiers in Neuroinformatics*, *12*, 14. https://doi.org/10.3389/fninf.2018.00014

Sawtell, N. B. (2017). Neural Mechanisms for Predicting the Sensory Consequences of Behavior: Insights from Electrosensory Systems. *Annual Review of Physiology*, *79*(1), 381–399. https://doi.org/10.1146/annurev-physiol-021115-105003

Schonewille, M., Khosrovani, S., Winkelman, B. H. J., Hoebeek, F. E., De Jeu, M. T. G., Larsen, I. M., … De Zeeuw, C. I. (2006). Purkinje cells in awake behaving animals operate at the upstate membrane potential. *Nature Neuroscience*, *9*, 459. Retrieved from http://dx.doi.org/10.1038/nn0406-459

Shin, S.-L., Hoebeek, F. E., Schonewille, M., De Zeeuw, C. I., Aertsen, A., & De Schutter, E. (2007). Regular Patterns in Cerebellar Purkinje Cell Simple Spike Trains. *PLoS ONE*, *2*(5), e485. https://doi.org/10.1371/journal.pone.0000485

Sługocka, A., Wiaderkiewicz, J., & Barski, J. J. (2017). Genetic Targeting in Cerebellar Purkinje Cells: an Update. *The Cerebellum*, *16*(1), 191–202. https://doi.org/10.1007/s12311-016-0770-4

Solé-Casals, J., & Caiafa, C. F. (2011). A Simple Approximation for Fast Nonlinear Deconvolution. In C. M. Travieso-González & J. B. Alonso-Hernández (Eds.), *Advances in Nonlinear Speech Processing* (Vol. 7015, pp. 55–62). Berlin, Heidelberg: Springer Berlin Heidelberg. https://doi.org/10.1007/978-3-642-25020-0_8

Stell, B. M. (2018). *Igor2p: 2-Photon scanning functions for Igor Pro*. IGOR Pro, Cerebellum. Retrieved from https://github.com/StPeres-Cerebellum/Igor2p (Original work published 2015)

Sugihara Izumi, Fujita Hirofumi, Na Jie, Quy Pham Nguyen, Li Bing-Yang, & Ikeda Daisuke. (2008). Projection of reconstructed single purkinje cell axons in relation to the cortical and nuclear aldolase C compartments of the rat cerebellum. *Journal of Comparative Neurology*, *512*(2), 282–304. https://doi.org/10.1002/cne.21889

Sullivan, M. R., Nimmerjahn, A., Sarkisov, D. V., Helmchen, F., & Wang, S. S.-H. (2005). In Vivo Calcium Imaging of Circuit Activity in Cerebellar Cortex. *Journal of Neurophysiology*, *94*(2), 1636–1644. https://doi.org/10.1152/jn.01013.2004

Takahashi, A., Camacho, P., Lechleiter, J. D., & Herman, B. (1999). Measurement of Intracellular Calcium. *Physiological Reviews*, *79*(4), 1089–1125. https://doi.org/10.1152/physrev.1999.79.4.1089

Tank, D., Sugimori, M., Connor, J., & Llinas, R. (1988). Spatially resolved calcium dynamics of mammalian Purkinje cells in cerebellar slice. *Science*, *242*(4879), 773. https://doi.org/10.1126/science.2847315

Theis, L., Berens, P., Froudarakis, E., Reimer, J., Román Rosón, M., Baden, T., … Bethge, M. (2016). Benchmarking Spike Rate Inference in Population Calcium Imaging. *Neuron*, *90*(3), 471–482. https://doi.org/10.1016/j.neuron.2016.04.014

Usowicz, M. M., Sugimori, M., Cherksey, B., & Llinás, R. (1992). P-type calcium channels in the somata and dendrites of adult cerebellar purkinje cells. *Neuron*, *9*(6), 1185–1199. https://doi.org/10.1016/0896-6273(92)90076-P

Vogelstein, J. T., Watson, B. O., Packer, A. M., Yuste, R., Jedynak, B., & Paninski, L. (2009). Spike Inference from Calcium Imaging Using Sequential Monte Carlo Methods. *Biophysical Journal*, *97*(2), 636–655. https://doi.org/10.1016/j.bpj.2008.08.005

Wilt, B. A., Fitzgerald, J. E., & Schnitzer, M. J. (2013). Photon shot noise limits on optical detection of neuronal spikes and estimation of spike timing. *Biophysical Journal*, *104*(1), 51–62. https://doi.org/10.1016/j.bpj.2012.07.058

Womack, M. D., Chevez, C., & Khodakhah, K. (2004). Calcium-Activated Potassium Channels Are Selectively Coupled to P/Q-Type Calcium Channels in Cerebellar Purkinje Neurons. *The Journal of Neuroscience*, *24*(40), 8818. https://doi.org/10.1523/JNEUROSCI.2915-04.2004

Xiao, J., Cerminara, N. L., Kotsurovskyy, Y., Aoki, H., Burroughs, A., Wise, A. K., … Lang, E. J. (2014). Systematic Regional Variations in Purkinje Cell Spiking Patterns. *PLOS ONE*, *9*(8), e105633. https://doi.org/10.1371/journal.pone.0105633

Xu, Y., Zou, P., & Cohen, A. E. (2017). Voltage imaging with genetically encoded indicators. *Molecular Imaging Chemical Genetics and Epigenetics*, *39*, 1–10. https://doi.org/10.1016/j.cbpa.2017.04.005

Y. Jung, & M. Enqvist. (2013). Estimating models of inverse systems. In *52nd IEEE Conference on Decision and Control* (pp. 7143–7148). https://doi.org/10.1109/CDC.2013.6761022

Yaksi, E., & Friedrich, R. W. (2006). Reconstruction of firing rate changes across neuronal populations by temporally deconvolved Ca2+ imaging. *Nature Methods*, *3*, 377. Retrieved from http://dx.doi.org/10.1038/nmeth874

Yamada, Y., & Mikoshiba, K. (Eds.). (2016). Putting a Finishing Touch on GECI. In *Application of Genetically Encoded Indicators to Mammalian Central Nervous System* (Vol. 7, pp. 23–37). Frontiers Media SA. https://doi.org/10.3389/978-2-88919-804-7

Zariwala, H. A., Borghuis, B. G., Hoogland, T. M., Madisen, L., Tian, L., De Zeeuw, C. I., … Chen, T.-W. (2012). A Cre-Dependent GCaMP3 Reporter Mouse for Neuronal Imaging In Vivo. *The Journal of Neuroscience*, *32*(9), 3131. https://doi.org/10.1523/JNEUROSCI.4469-11.2012

Zhou, H., Lin, Z., Voges, K., Ju, C., Gao, Z., Bosman, L. W., … Schonewille, M. (2014). Cerebellar modules operate at different frequencies. *ELife*, *3*, e02536. https://doi.org/10.7554/eLife.02536

Zhou, H., Voges, K., Lin, Z., Ju, C., & Schonewille, M. (2015). Differential Purkinje cell simple spike activity and pausing behavior related to cerebellar modules. *Journal of Neurophysiology*, *113*(7), 2524–2536. https://doi.org/10.1152/jn.00925.2014

Zorrilla de San Martin, J., Jalil, A., & Trigo, F. F. (2015). Impact of single-site axonal GABAergic synaptic events on cerebellar interneuron activity. *The Journal of General Physiology*, *146*(6), 477. https://doi.org/10.1085/jgp.201511506

8. APPENDIX

Summarized compilation of the 2-Photon imaging recordings obtained from spontaneous acute experiments.

The following images and traces comprise a selection of recordings from each imaged field (called here a region) in anesthetized mice with GCaMP6f expression.

The regions are identified by a given number, an animal, and the date of recording. Each of the regions has an associated average image that has delineated the corresponding Regions of Interest (ROI) of each of the cells in the field. The traces below or right to the images correspond to the average number of counts of the pixels inside the somatic ROIs in the region. Simultaneous traces from the same region are stacked vertically in a top-to-down ascending order that follows the ROIs numeration (for reference, see the green numbers at the top and bottom of each vertical stack). The selection of data to show was carried out by choosing the continuous series of images that contained the biggest fluorescence change from all the recordings done in the same region.

The colored points inside the traces correspond to the detected slope change-points using slope thresholding (details on the detection procedure in Data Analysis). A red point corresponds to a significant transition from a negative-to-positive slope, and a blue point to a positive-to-negative transition. In a few regions a glimpse of spontaneous synchronization is visible when points get aligned in the vertical dimension.

The chosen parameters for the detection of change-points was:

1. Binomial smoothing with a window of 20 seconds (in each trace) and one pass, used to denoise the trace and find the estimated noise residuals.
2. A high noise threshold with Z-score ~ 3.3 ($\alpha = 0.001$) from the estimated noise residuals (assuming they were all distributed as gaussian noise). This results in the identification of the most significant change points with some true changes passing undetected in order to avoid the detection of possible signal artifacts.
3. A time duration limit for the changes (T_{thres}) comprising the whole length of the recordings, thus detecting the longest fluctuations.

Animal 1 – 20/Mar/2015

Regions 1 to 3

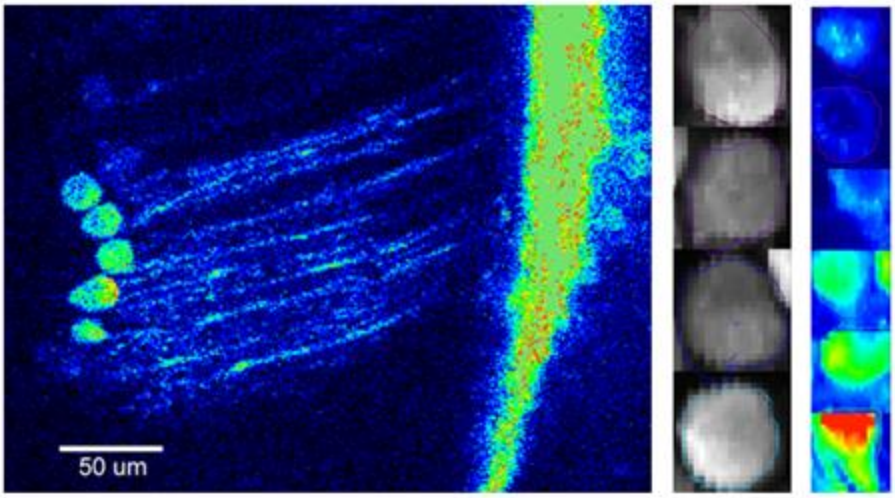

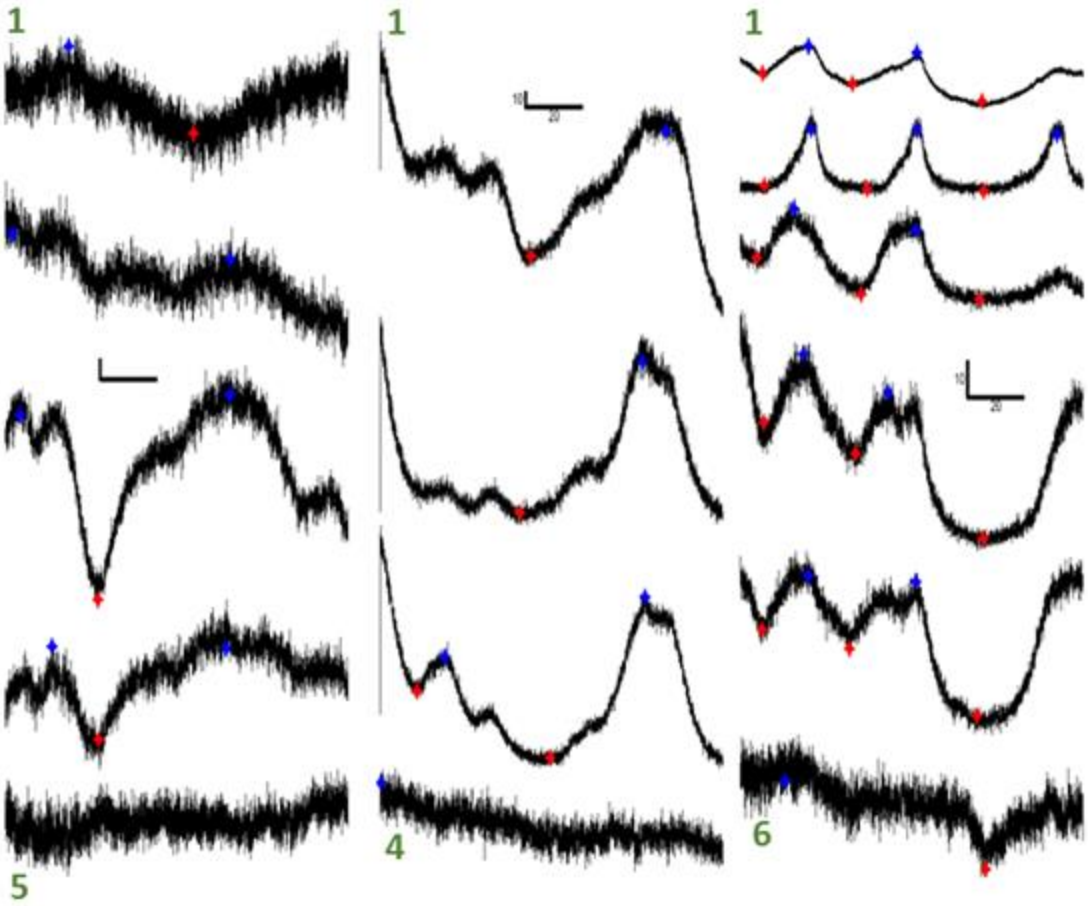

Scale Bar: 10 a.u. (Y), 20 s (X)

Animal 2 – 16/Feb/2016

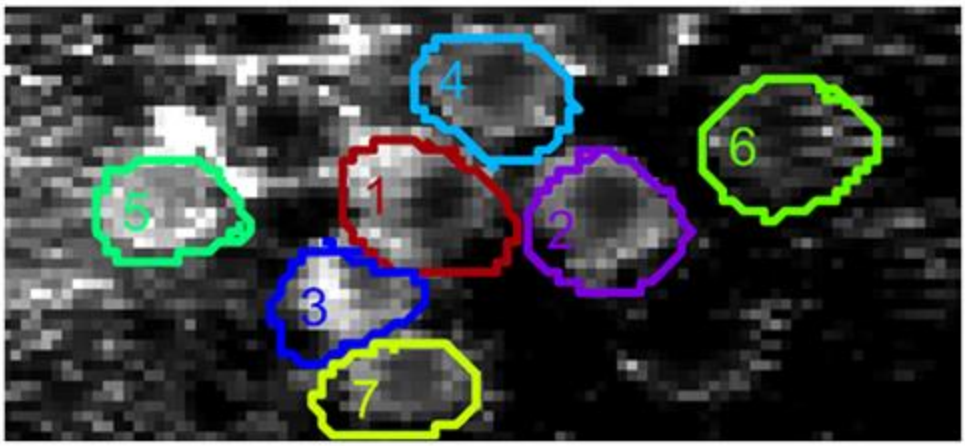

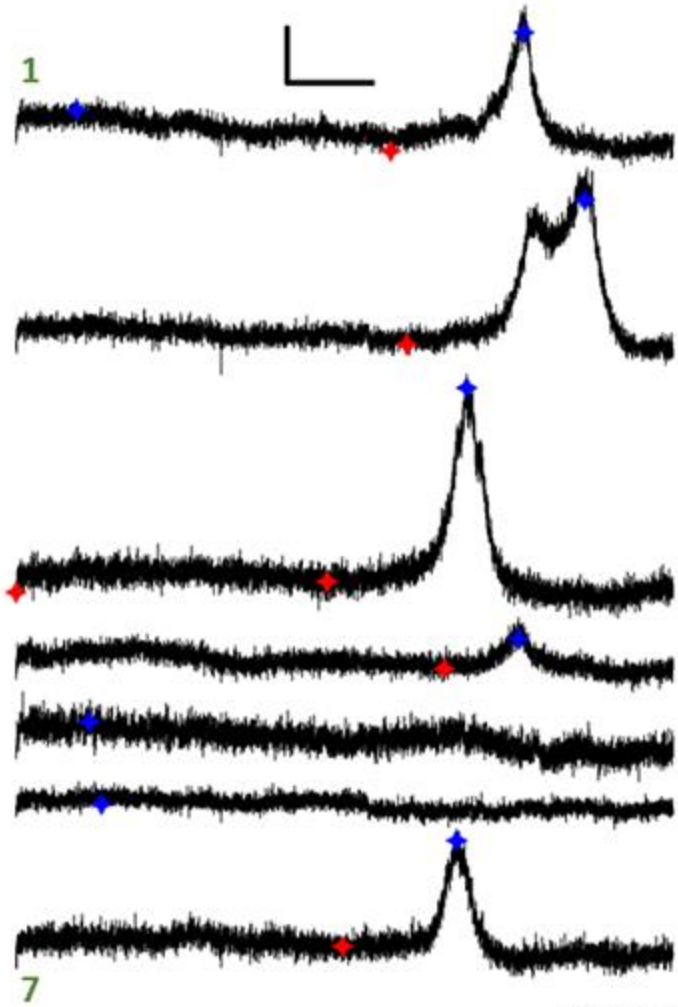

Scale Bar: 1 count (Y), 20 s (X)

Animal 3 – 25/Mar/2016
Regions 1, 2

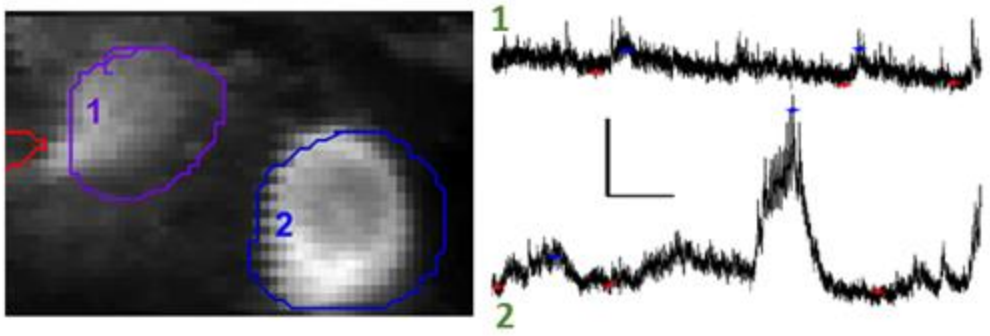

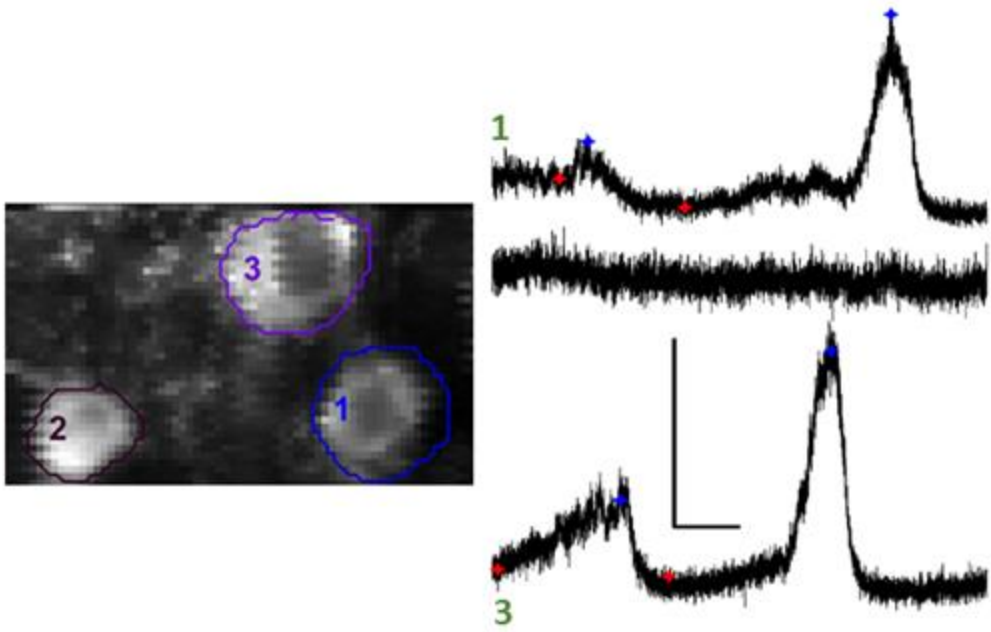

Scale Bar: 1 count (Y), 20 s (X)

Animal 4 – 20/Jun/2016

Regions 1, 2

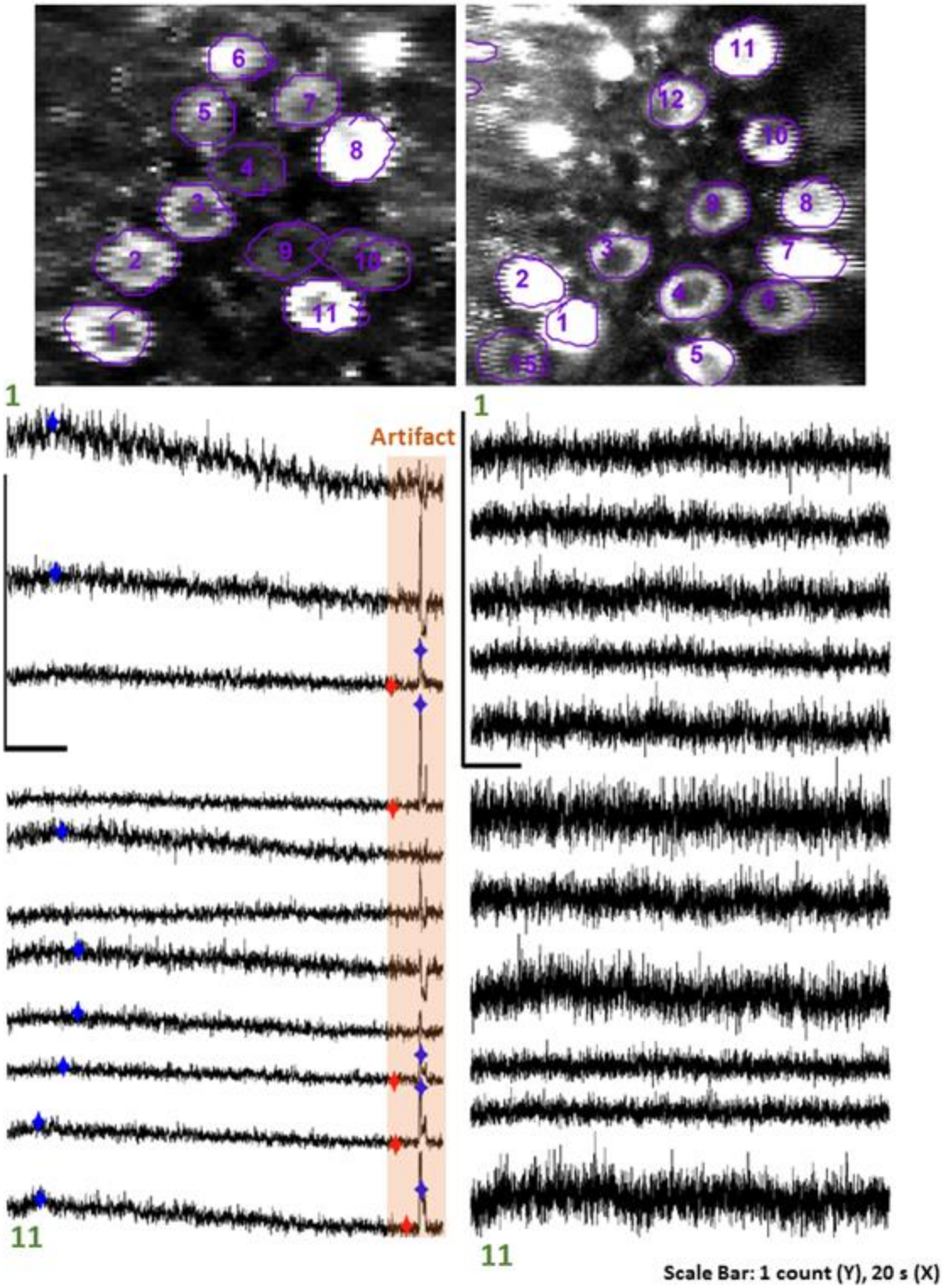

Animal 4 – 20/Jun/2016
Regions 3, 4

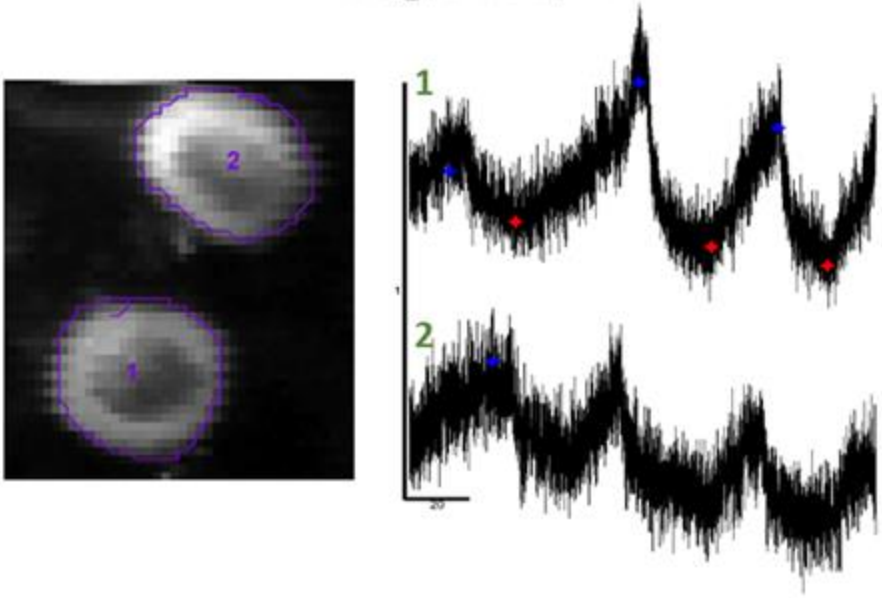

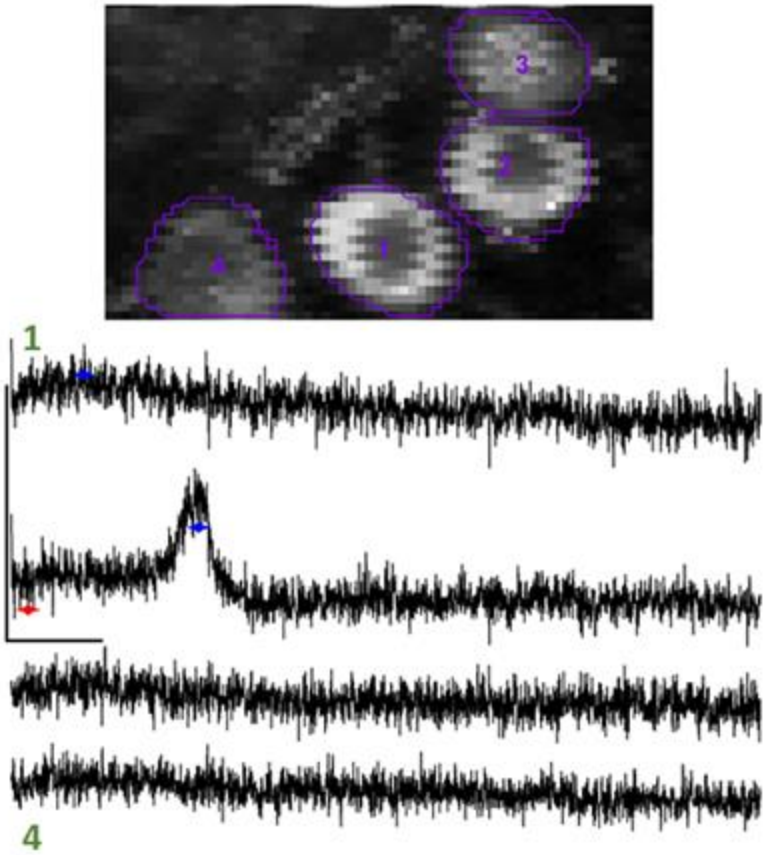

Scale Bar: 1 count (Y), 20 s (X)

Animal 5
18/Aug/2016

Animal 6
19/Aug/2016

Region 1

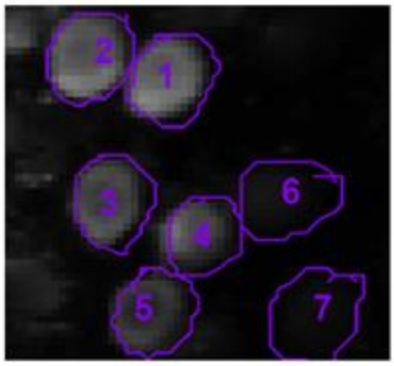

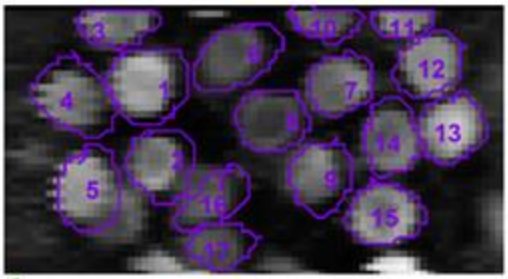

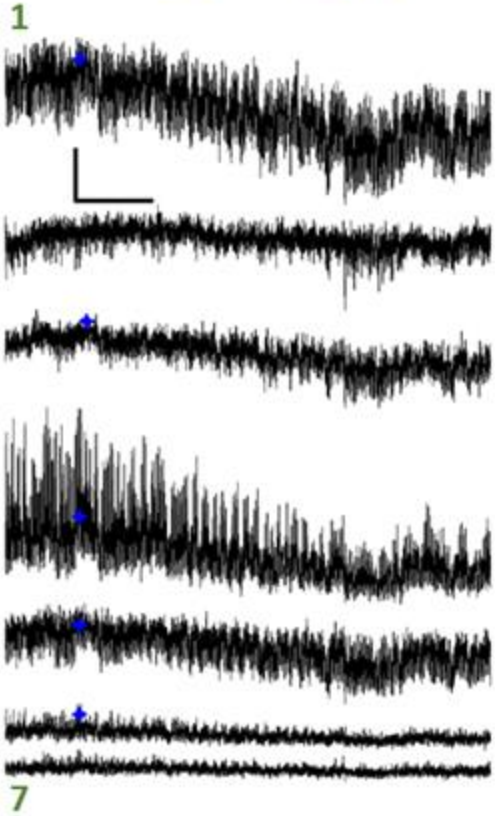

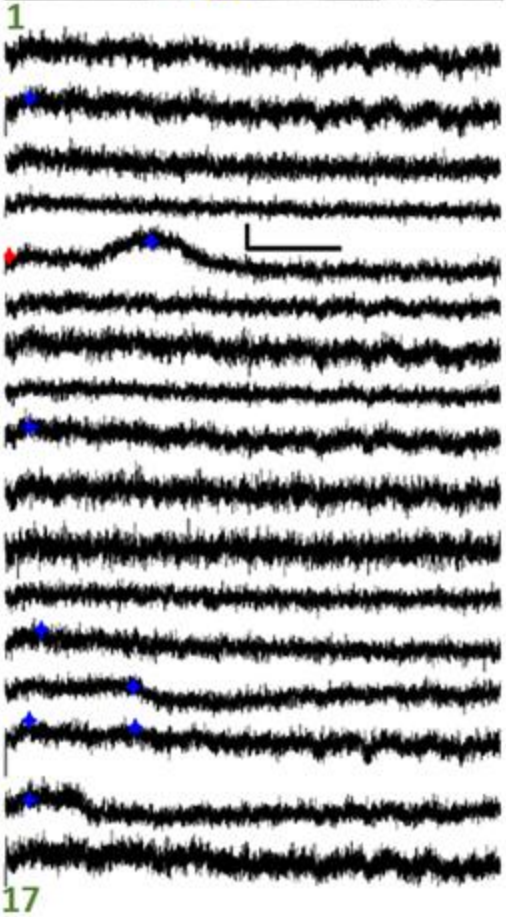

Scale Bar: 1 count (Y), 20 s (X)

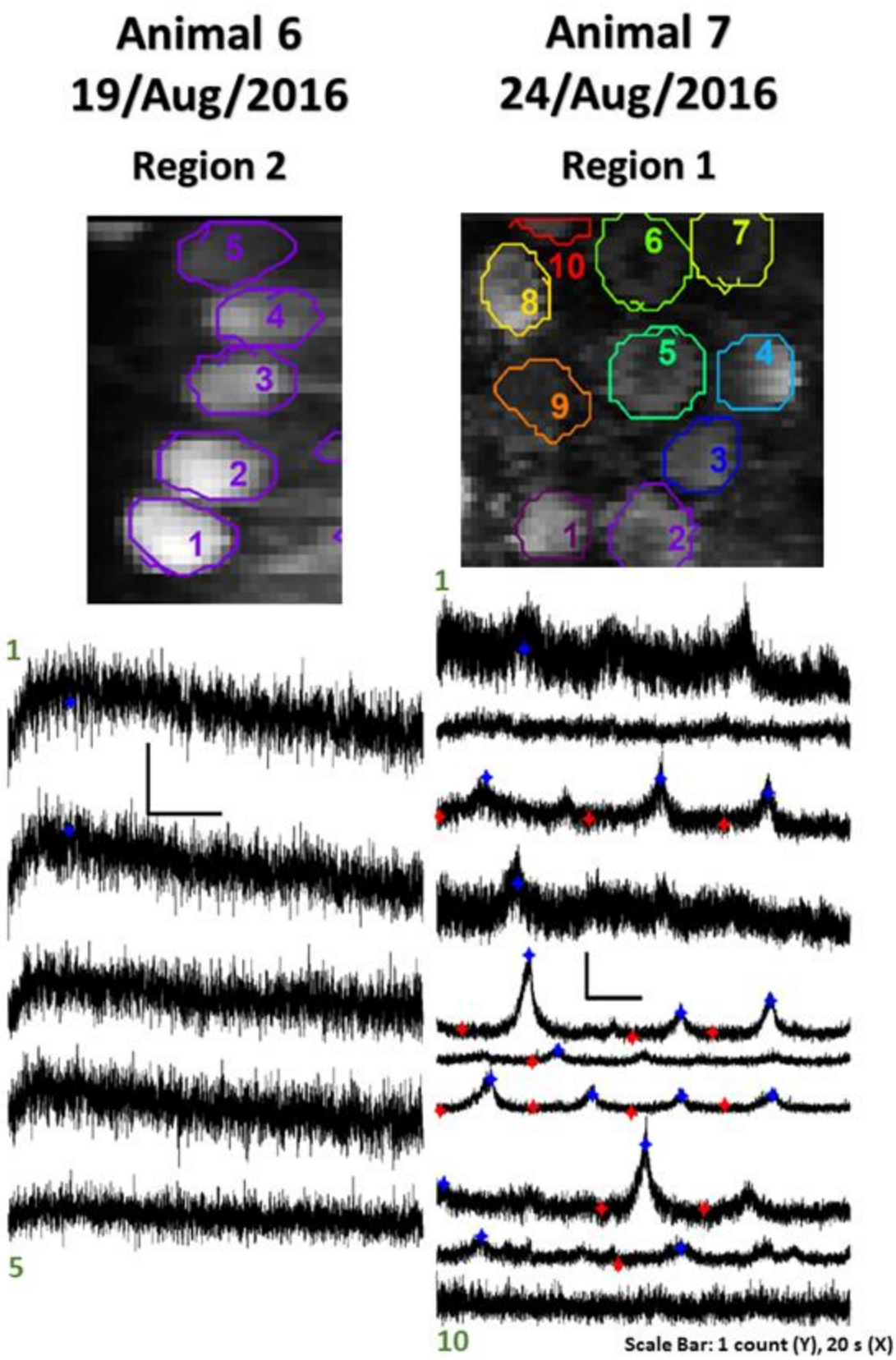
Animal 6
19/Aug/2016
Region 2
Animal 7
24/Aug/2016
Region 1
1
5
1
10
Scale Bar: 1 count (Y), 20 s (X)

Animal 7 – 24/Aug/2016
Regions 2, 3

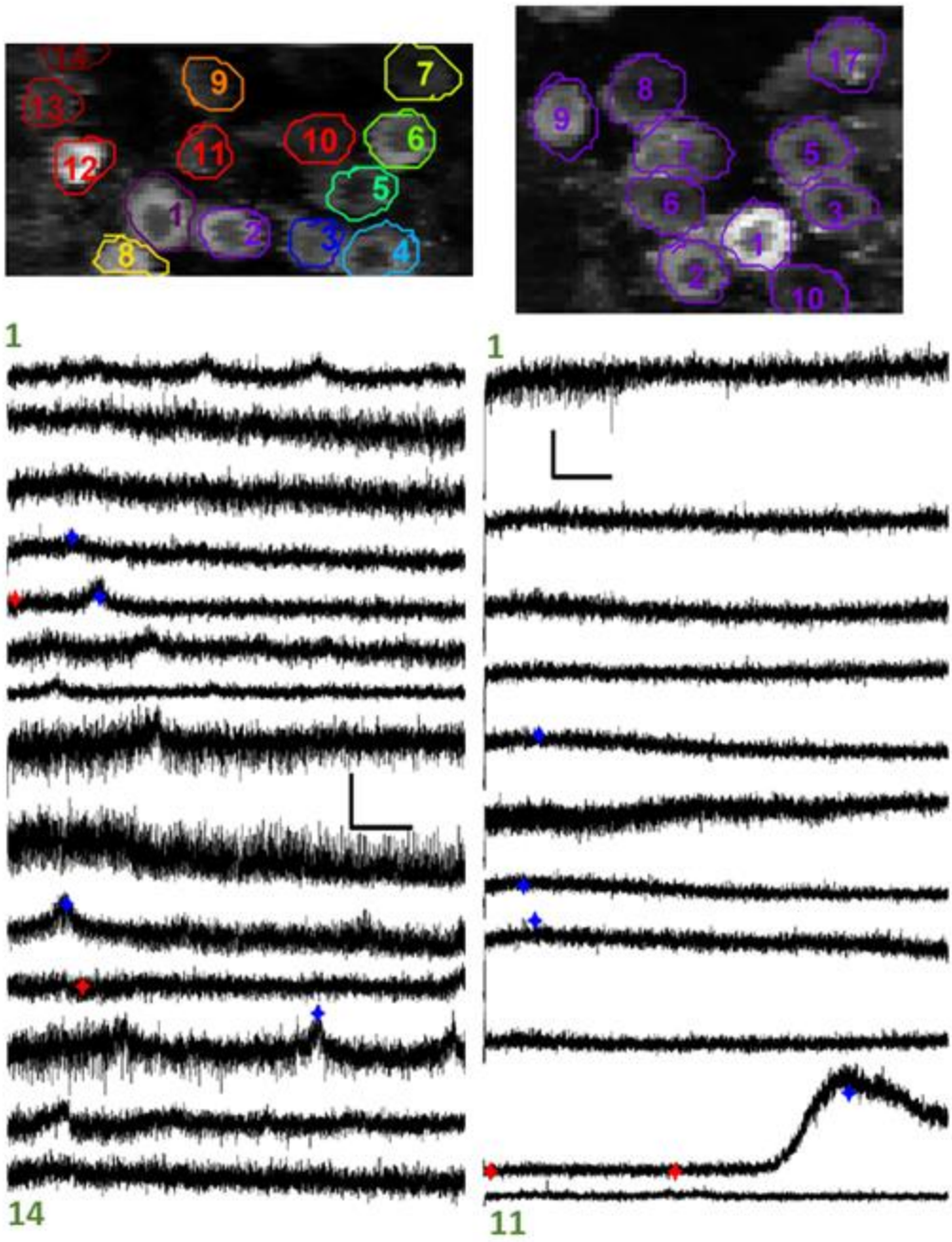

Scale Bar: 1 count (Y), 20 s (X)

Animal 8 – 25/Aug/2016

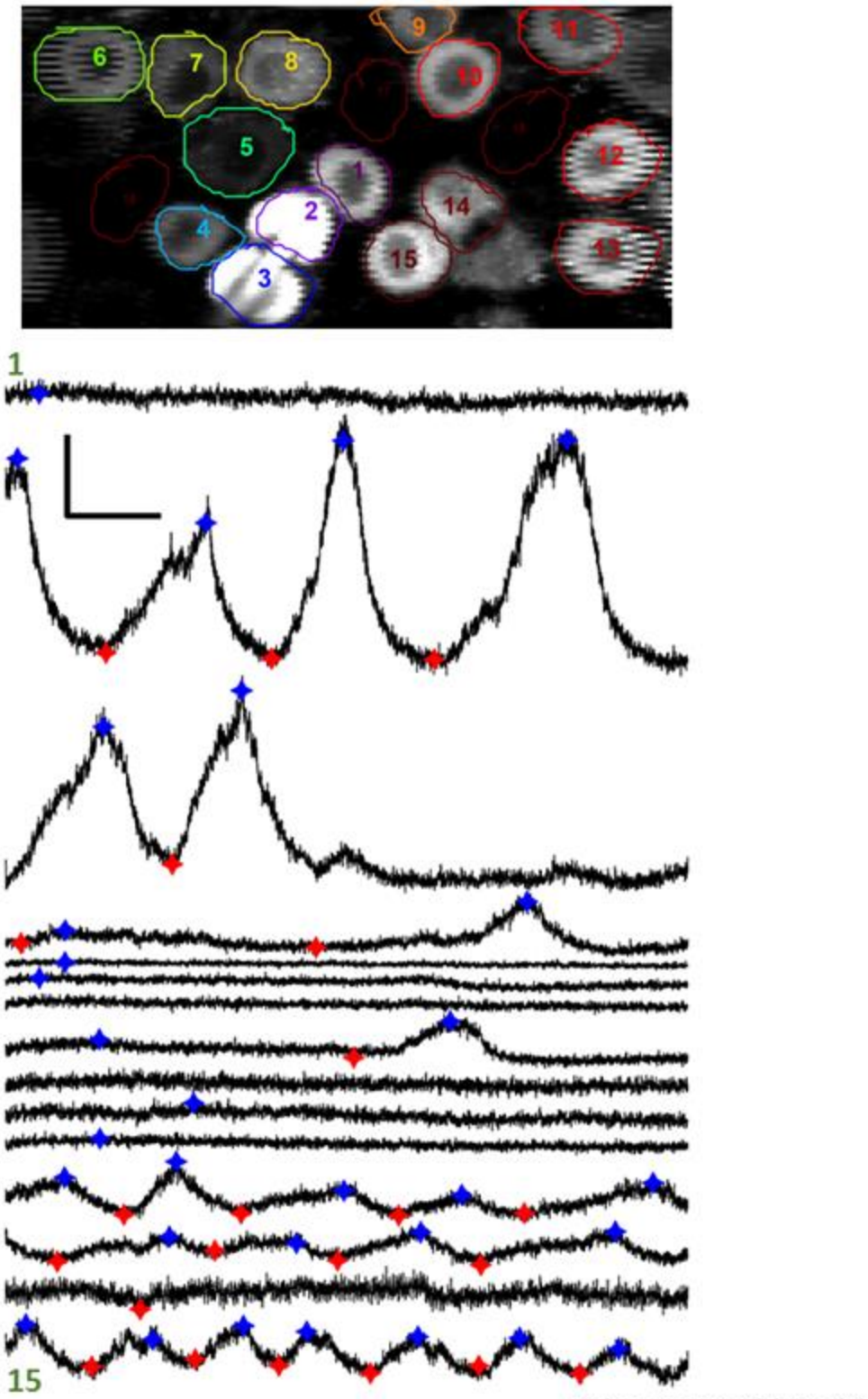

Animal 9 – 22/Sep/2016
Regions 1, 2

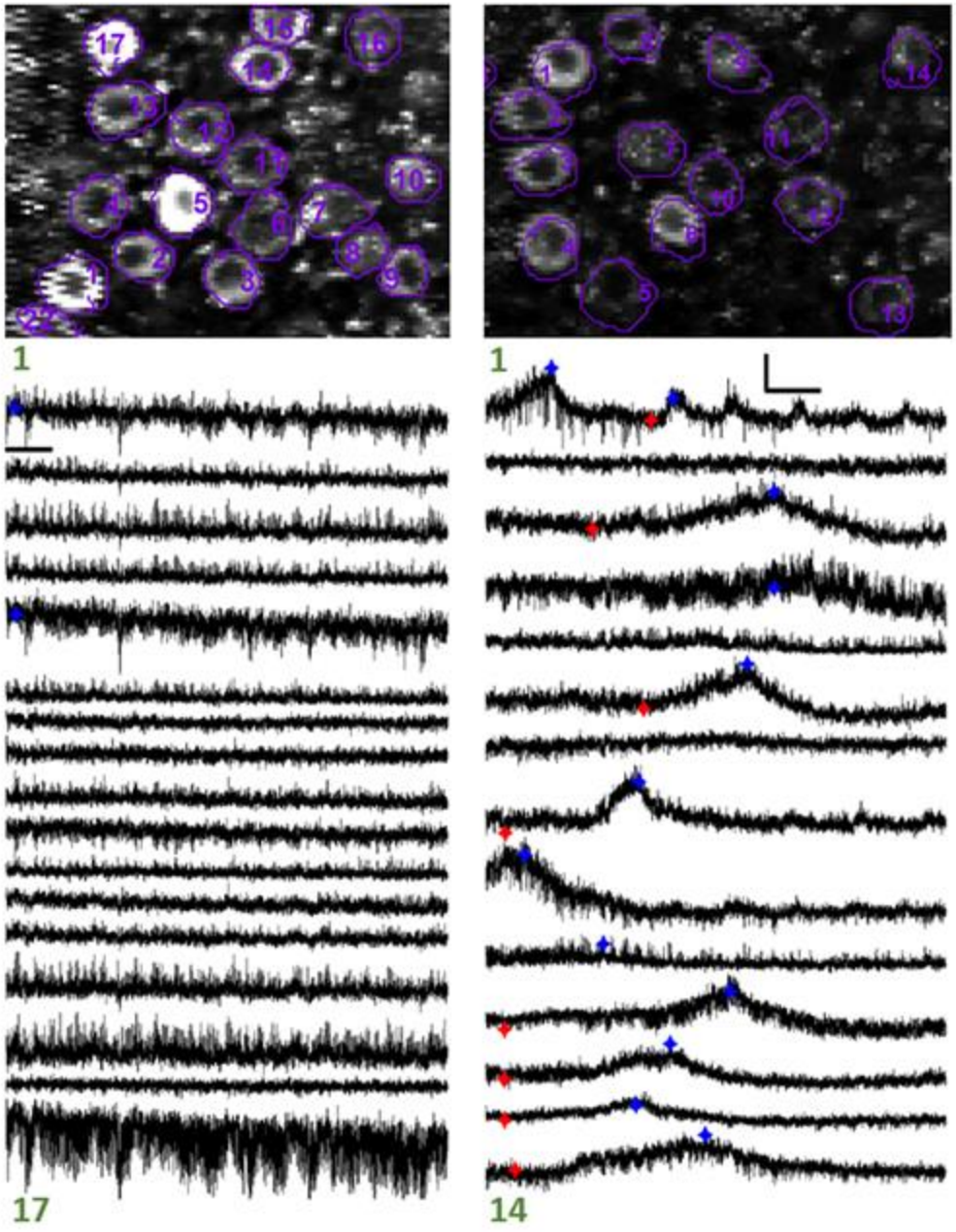

Scale Bar: 1 count (Y), 20 s (X)

Animal 10 – 23/Sep/2016
Regions 1, 2

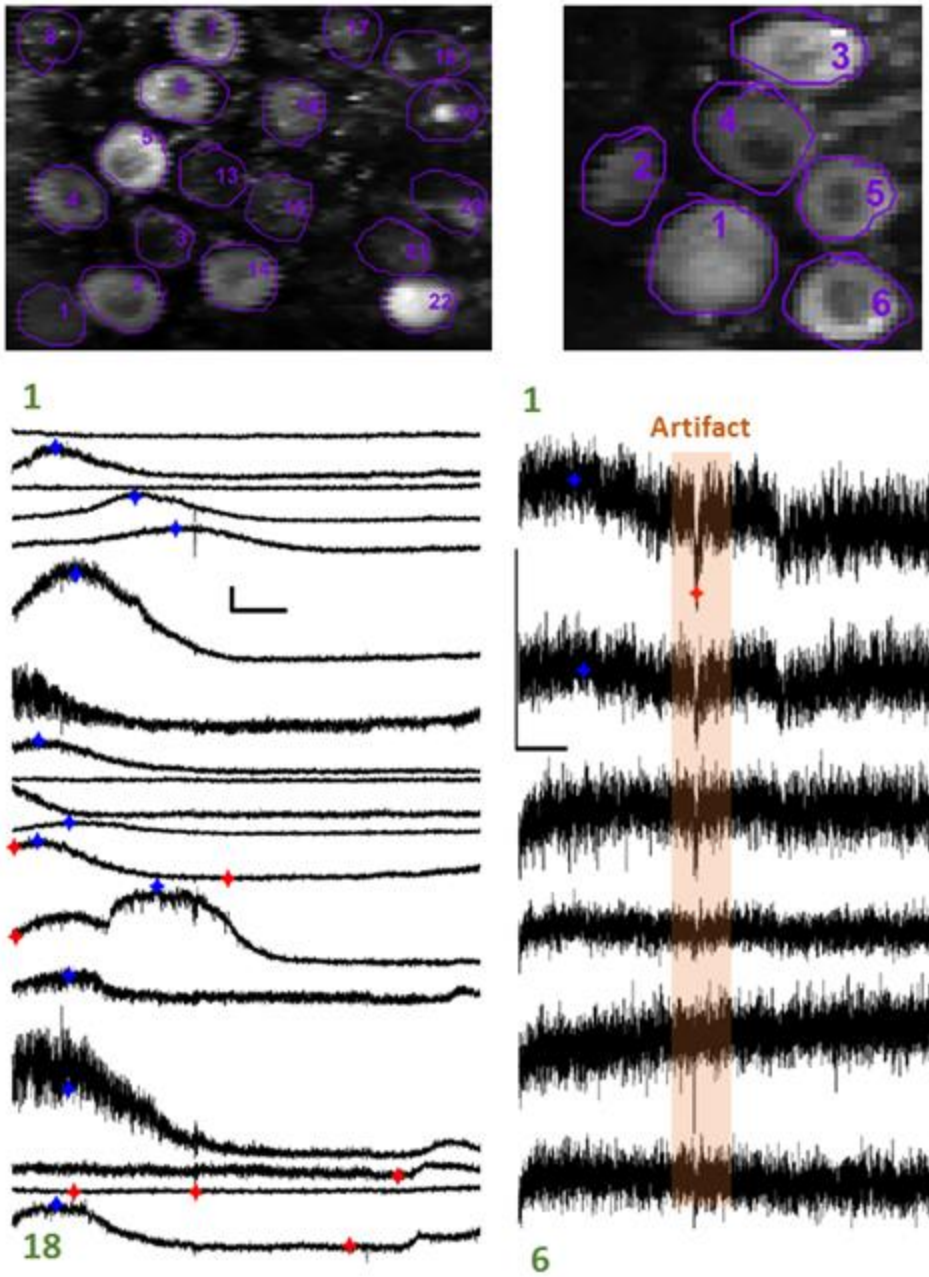

Scale Bar: 1 count (Y), 20 s (X)

Animal 10
23/Sep/2016

Region 3

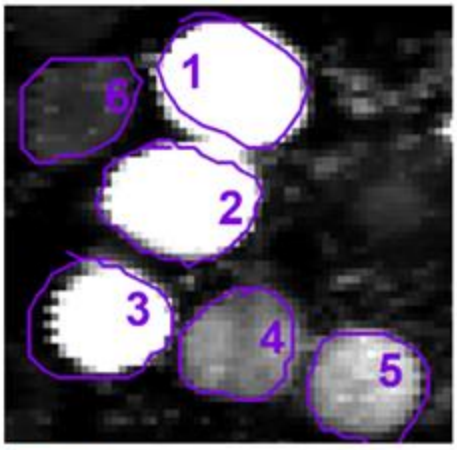

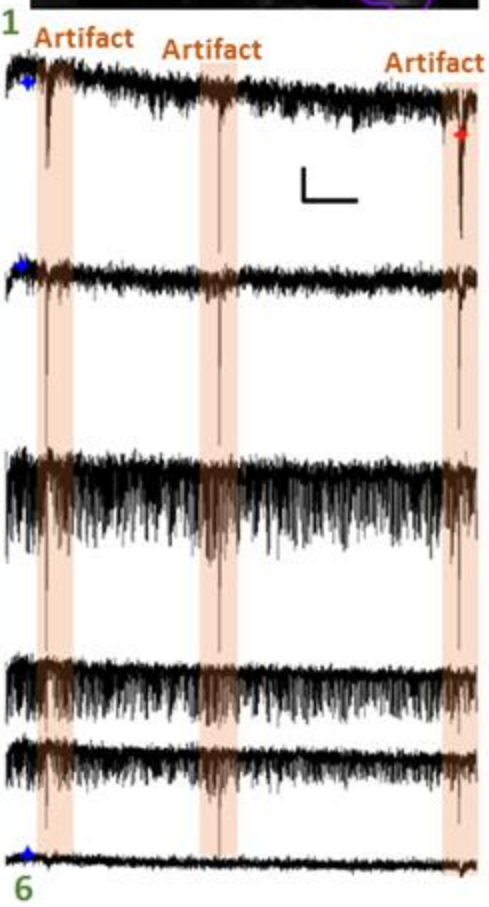

Animal 11
18/Oct/2016

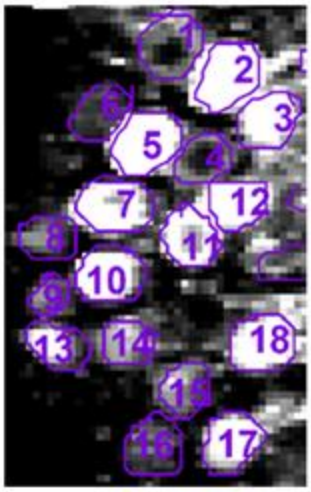

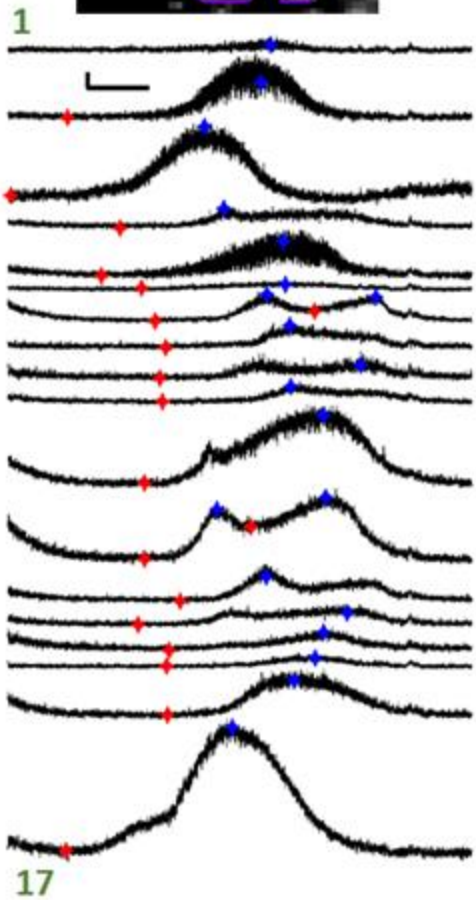

Scale Bar: 1 count (Y), 20 s (X)

Animal 12
19/Oct/2016

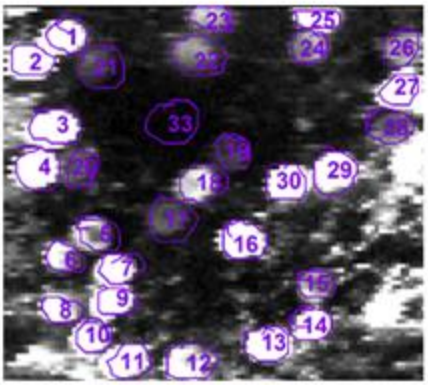

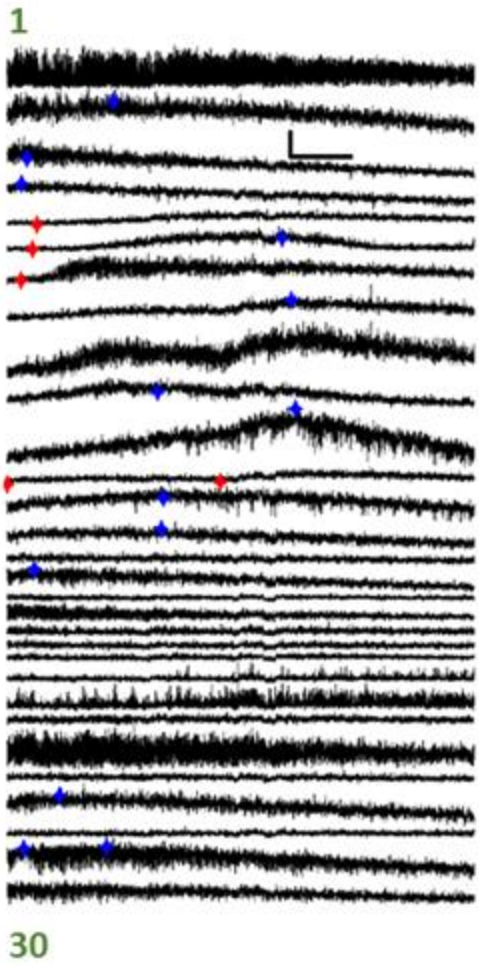

Animal 13
3/Nov/2016

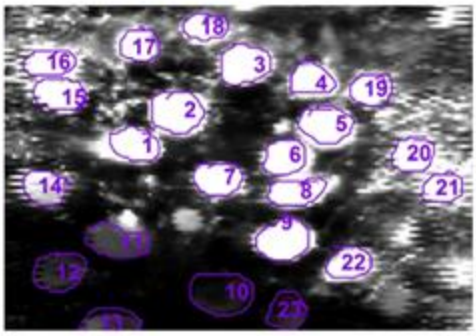

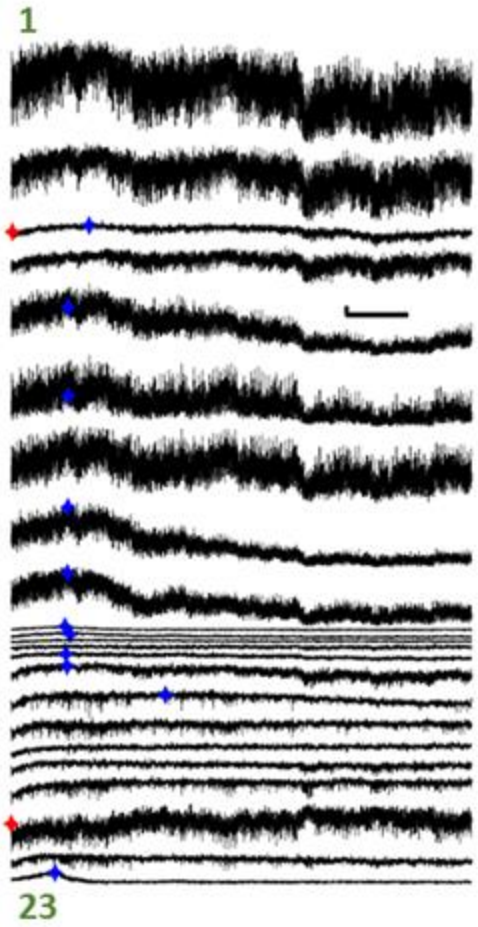

Scale Bar: 1 count (Y), 20 s (X)

Animal 14
23/Nov/2016
Region 3

Animal 15
26/Nov/2016
Region 1

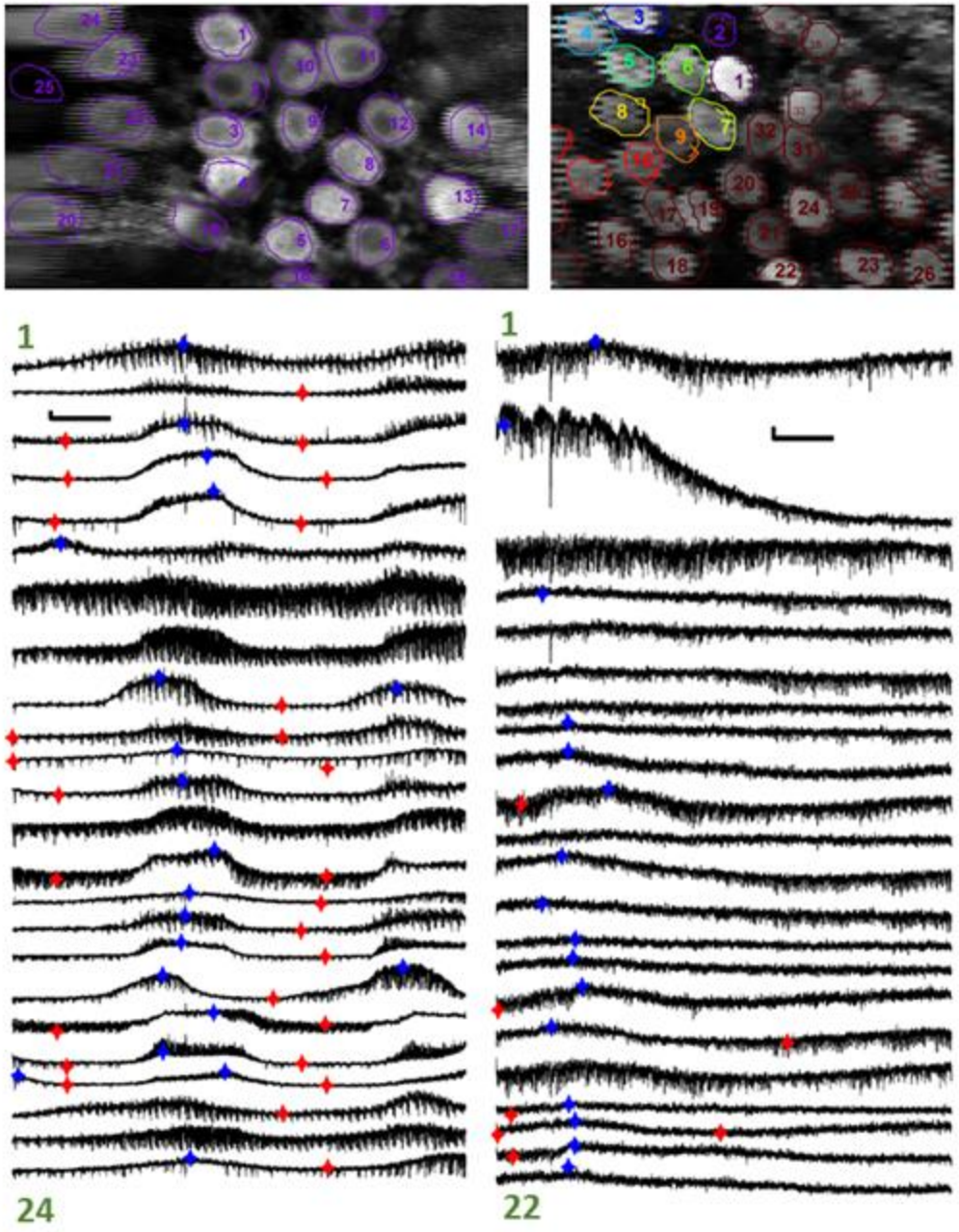

Scale Bar: 1 count (Y), 20 s (X)

Animal 15
26/Nov/2016
Region 2

Animal 16
16/Dec/2016

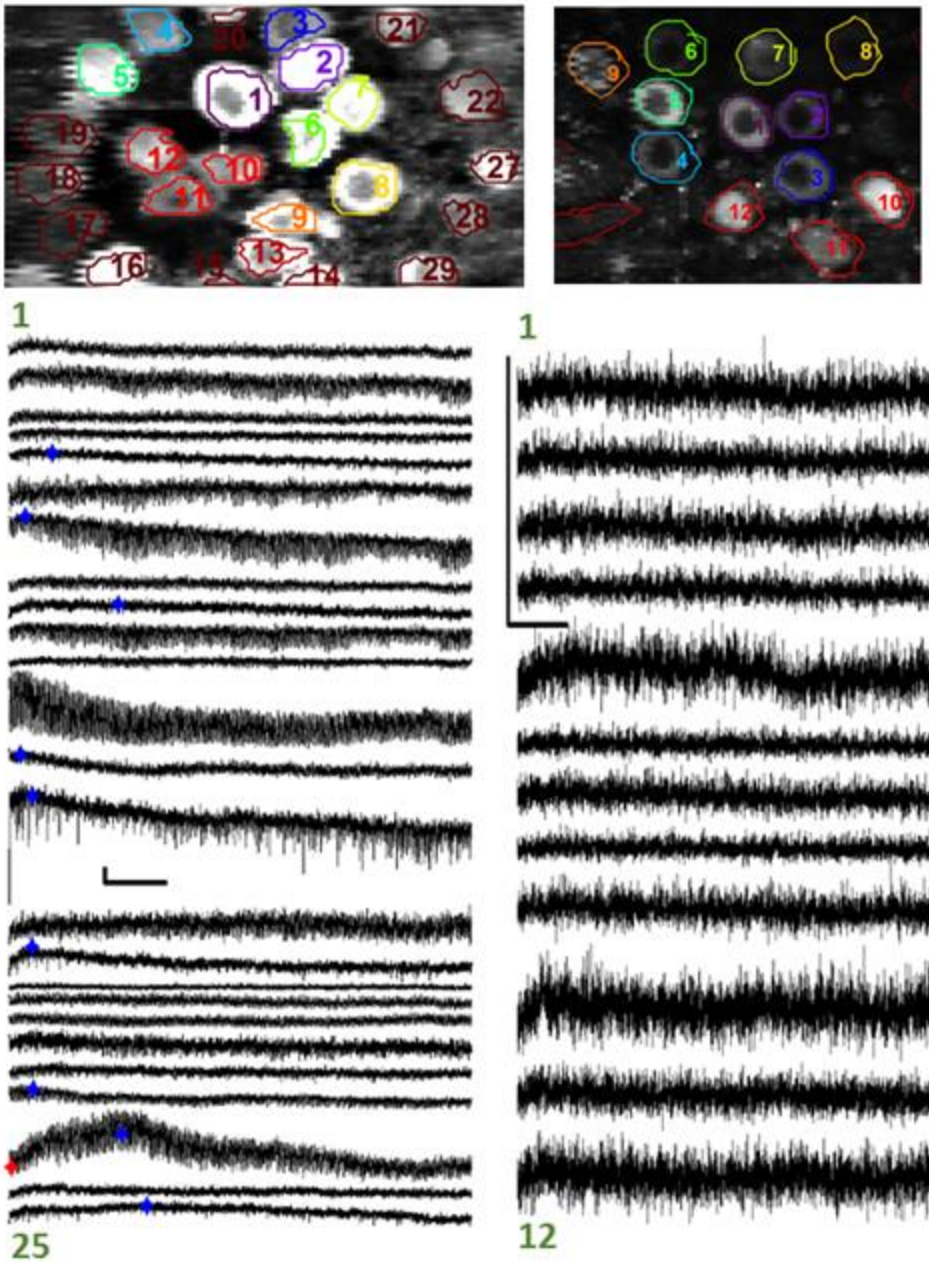

Scale Bar: 1 count (Y), 20 s (X)

Animal 17 – 22/Dec/2016
Regions 1 to 5

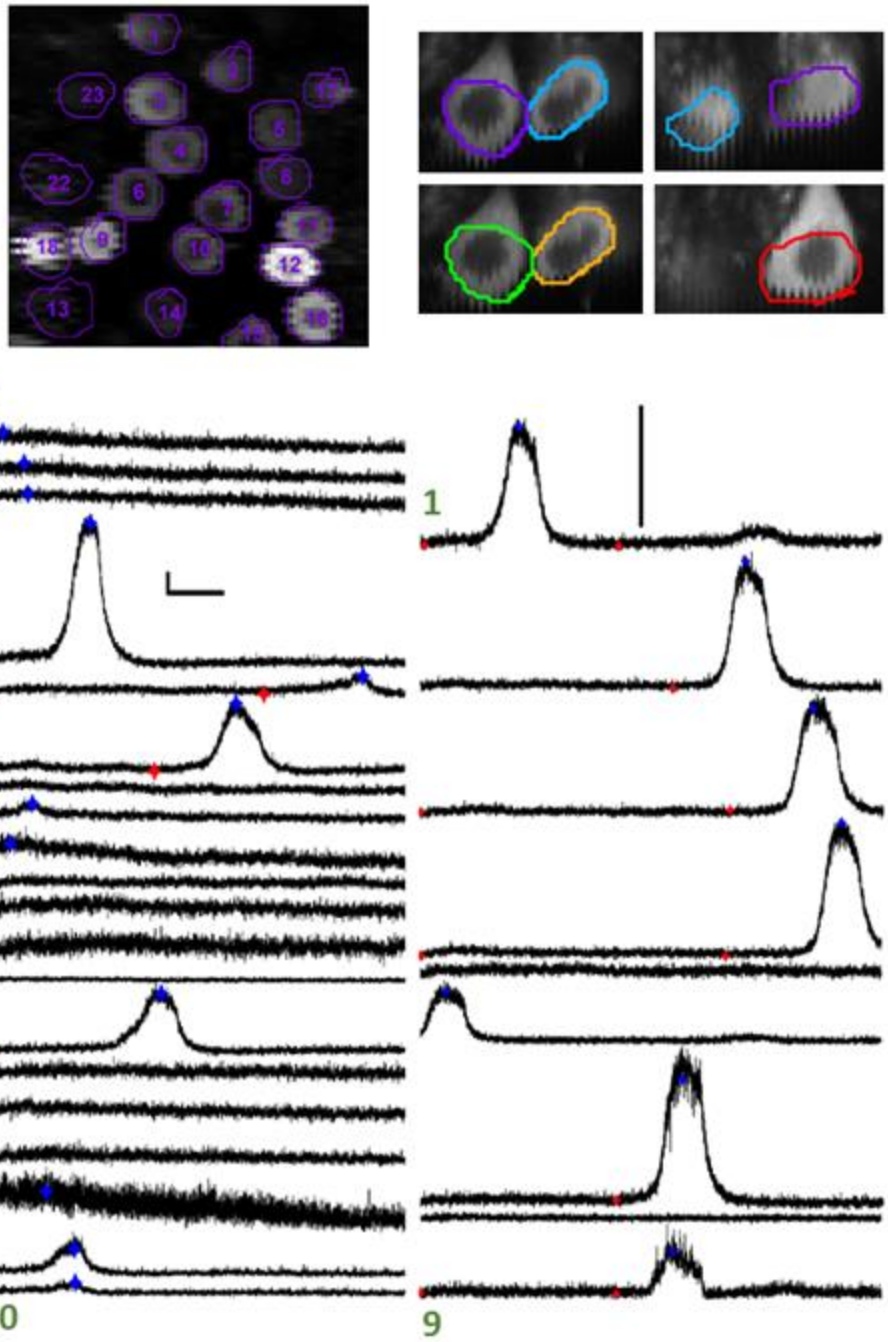

Scale Bar: 1 count (Y), 20 s (X)

Animal 18 – 20/Jan/2017
Regions 1, 2

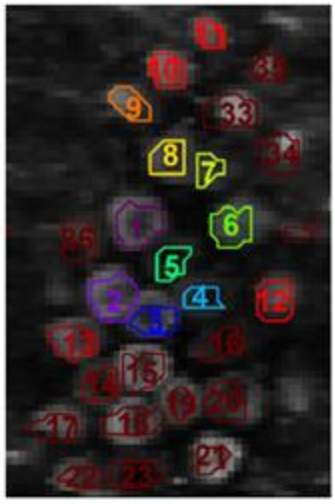

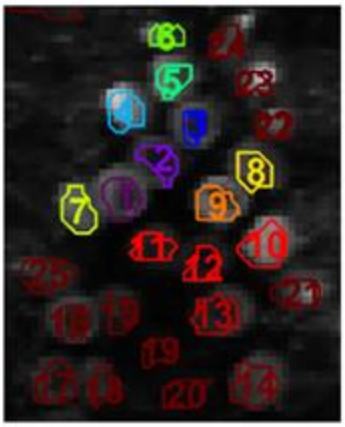

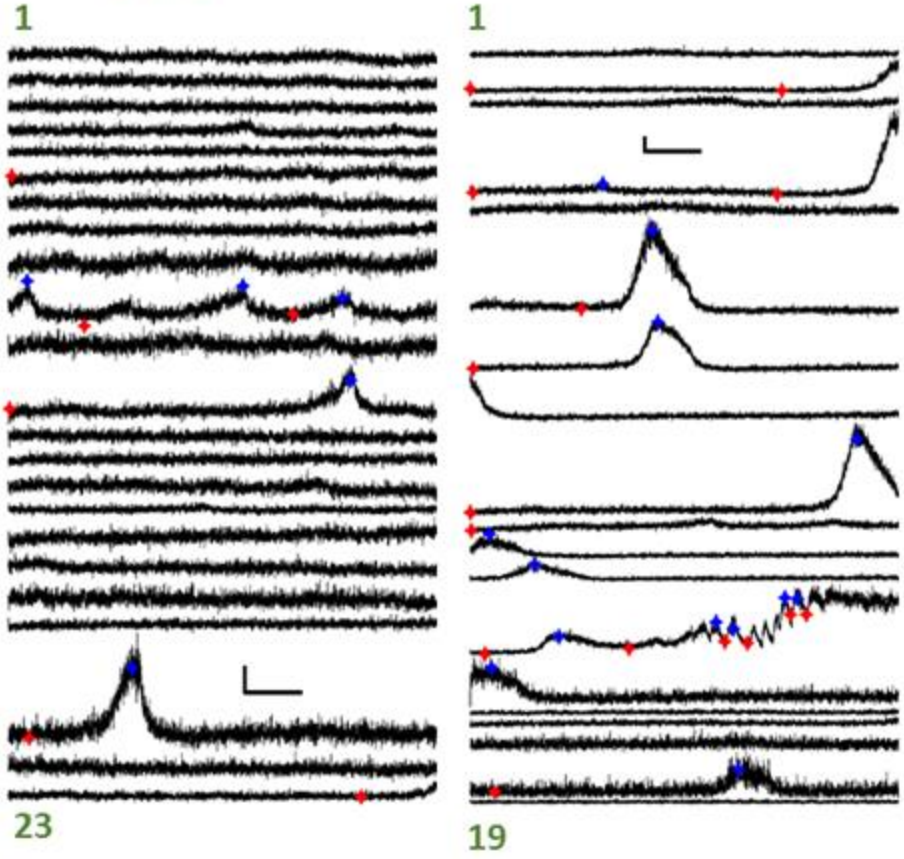

Scale Bar: 1 count (Y), 20 s (X)

Animal 19 – 24/Jan/2017
Regions 1, 2

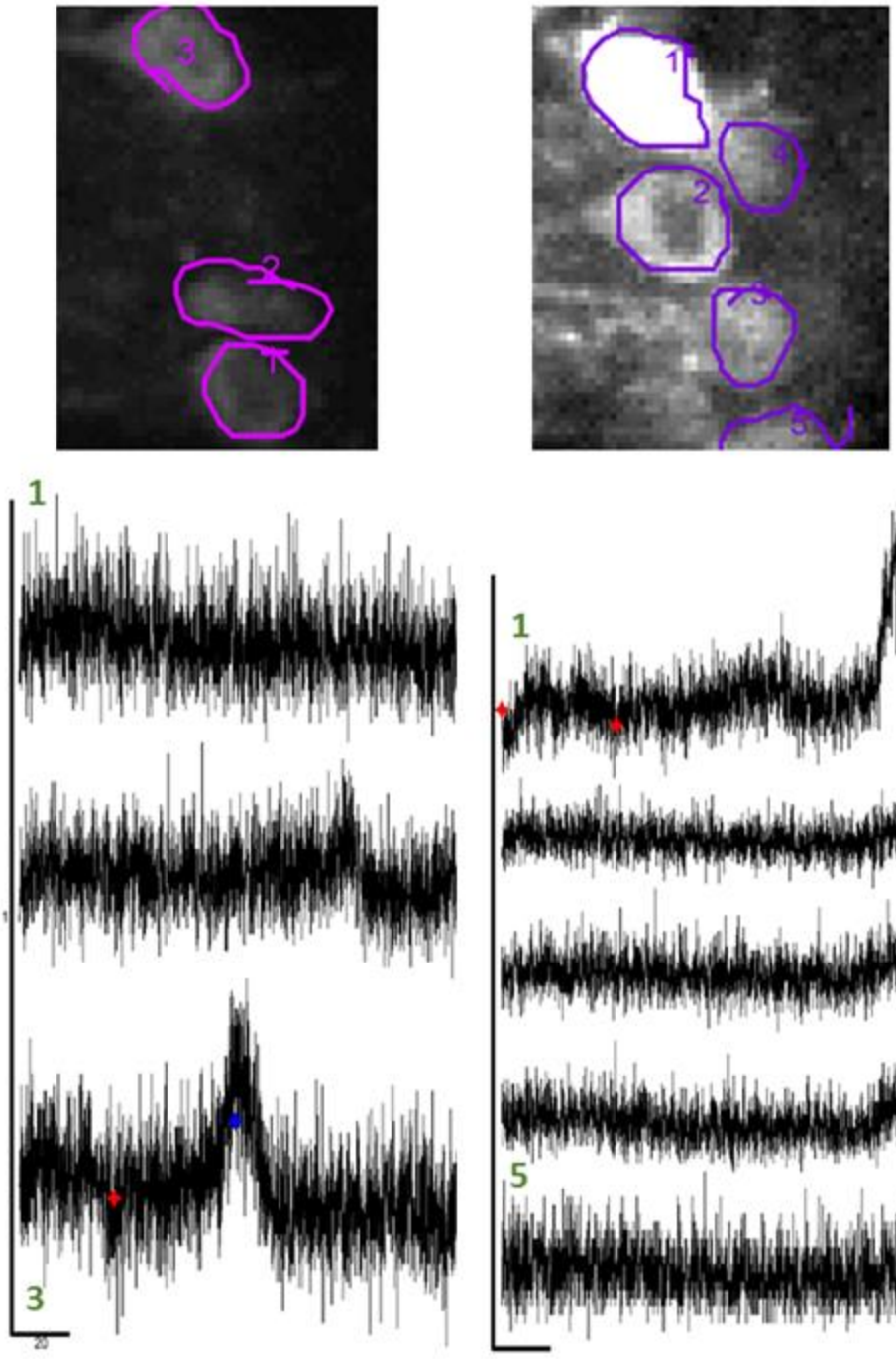

Scale Bar: 1 count (Y), 20 s (X)

Animal 19
24/Jan/2017
Region 3

Animal 20
2/Feb/2017

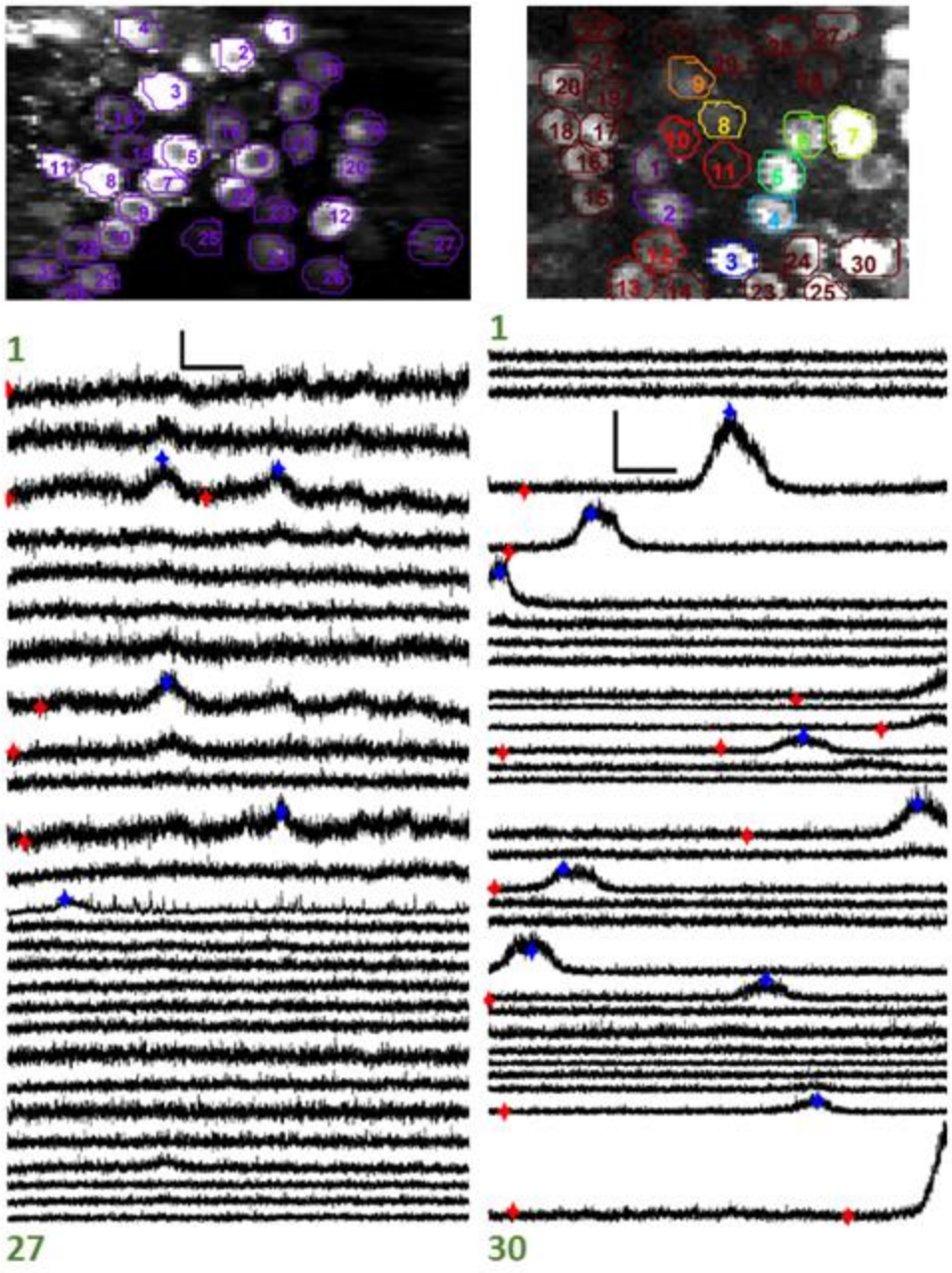

Scale Bar: 1 count (Y), 20 s (X)

Animal 21 – 7/Feb/2017
Regions 1, 2

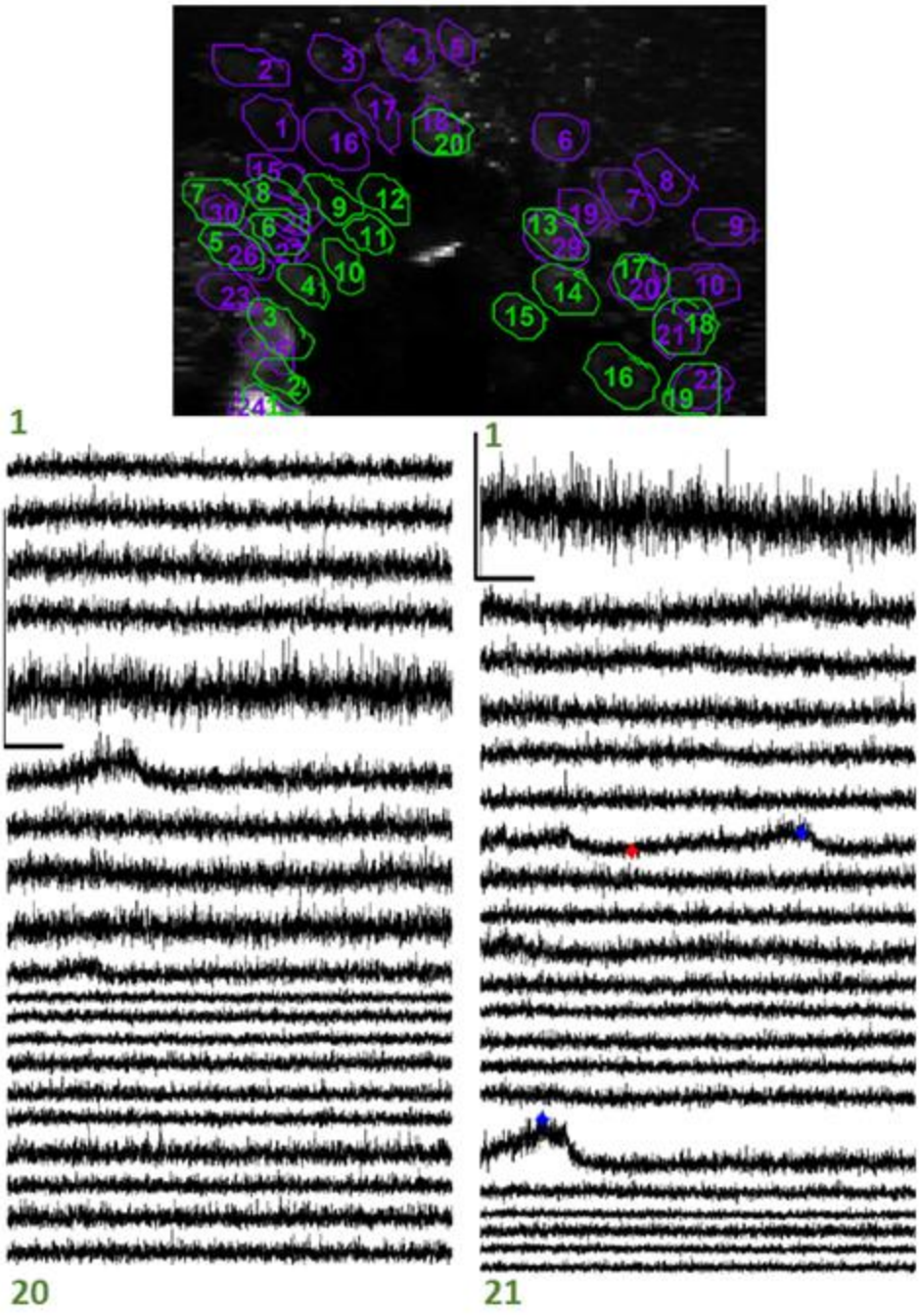

Scale Bar: 1 count (Y), 20 s (X)

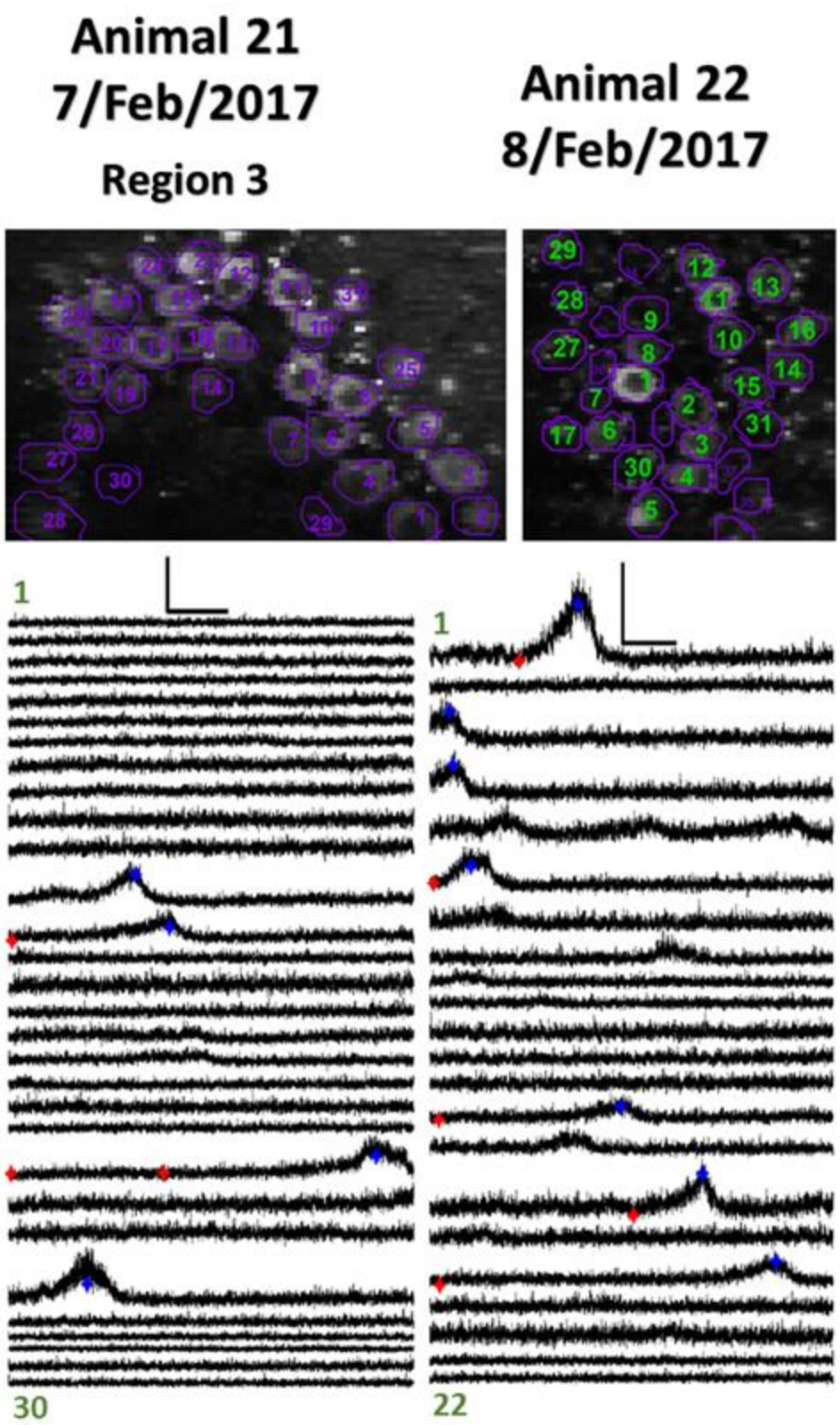
Animal 21
7/Feb/2017
Region 3
Animal 22
8/Feb/2017
1
30
1
22
Scale Bar: 1 count (Y), 20 s (X)

Animal 23
9/Feb/2017

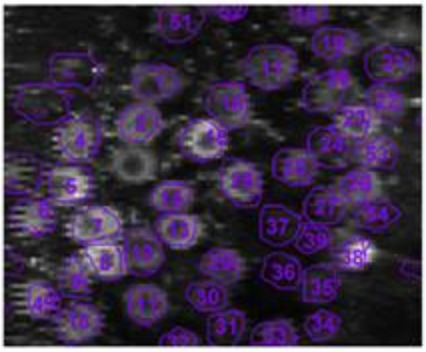

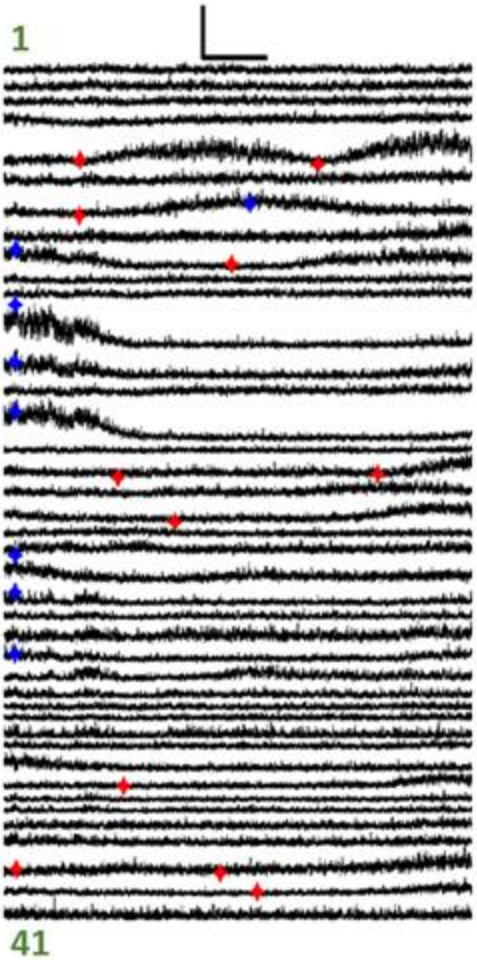

Animal 24
16/Feb/2017

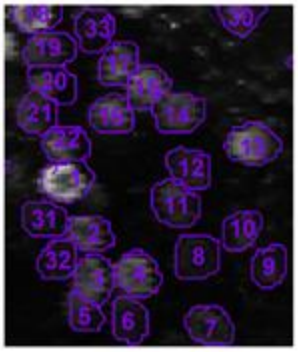

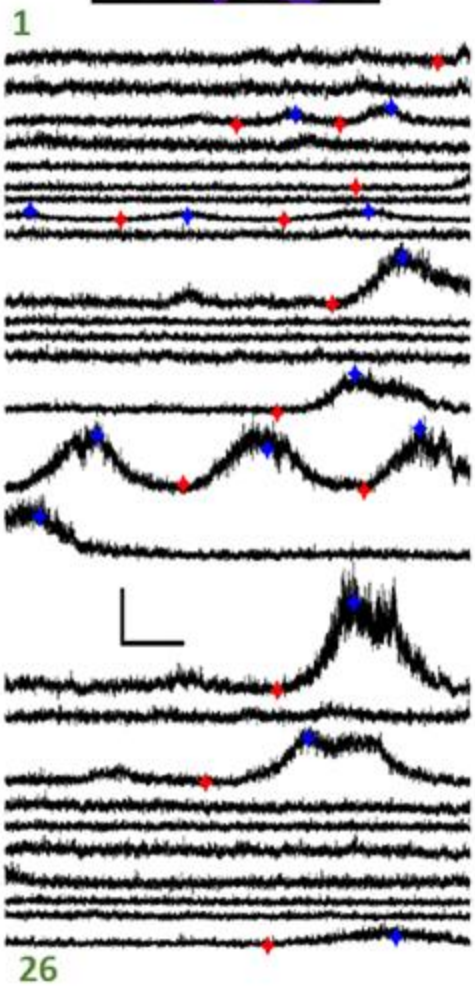

Scale Bar: 1 count (Y), 20 s (X)